WESTERN PACIFIC
REGIONAL BRANCH

Well Targeting Using Joint Geophysical Methods:

New Techniques for Exploration and Modelling

Prof. Peter Malin,

Institute of Earth Science and Engineering,

University of Auckland

WESTERN PACIFIC
REGIONAL BRANCH

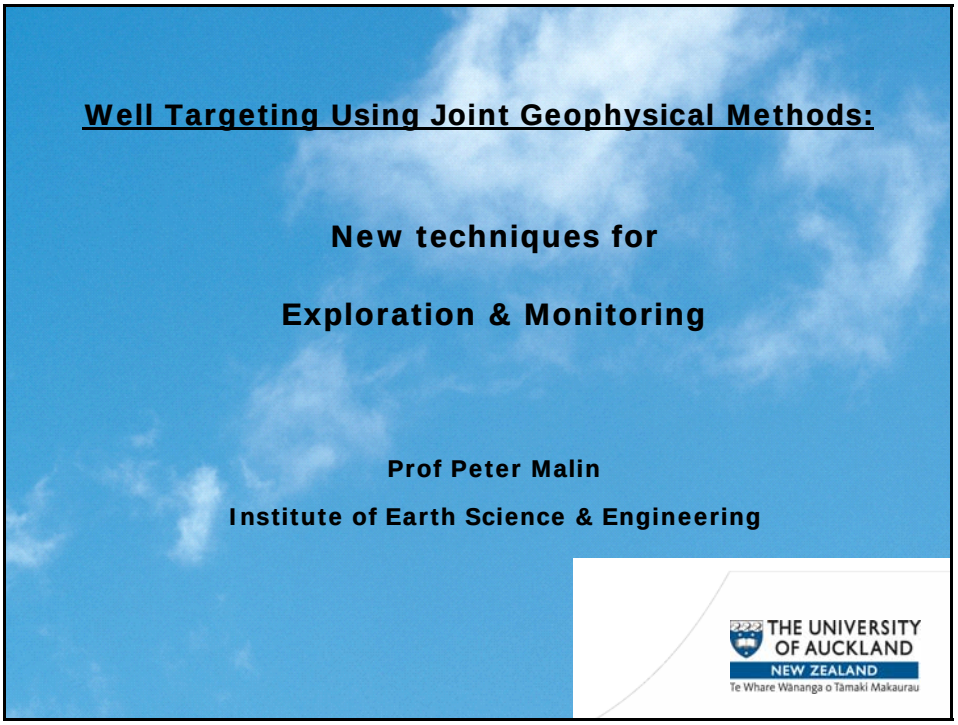

The objective of this talk is to introduce joint geophysical imaging and its application to earth energy exploration and environmental monitoring. Joint geophysical imaging is the combination of different geophysical methods to produce an accurate model of the earth's crust. The primary techniques discussed in this talk are seismic wave interpretation and electromagnetic resistivity measurements.

This presentation describes (1) the use of microearthquake (MEQ) and resistivity data to locate fluid-filled fracture zones within a geothermal system and (2) the well targeting test cases were these methods were applied. The methods use P- and S-wave velocity, S-wave polarization and splitting magnitude, resistivity and magnetotelluric (MT) -strike directions to determine fracture orientation and porosity. The conceptual approach used to characterize the buried, fluid-circulating fracture zones in hydrothermal systems is based on geological and fracture models. The method has been tested with geothermal field earthquake and resistivity data, core samples, temperature measurements, and more than 3 drilled well.

The seismic and electrical measurements used in the drill targeting examples come from portable, multi-station microearthquake (MEQ) monitoring networks, and multi-profile, MT and transient electromagnetic (TEM) observation campaigns. Examples of the methods are first discussed separately. The combined, or "joint", use of these measurements is based on the fact they share the effects of porosity and fracture induced anisotropy. The successful use of the joint method for targeting is presented for 2 wells, one predicted to be good and one bad.

WESTERN PACIFIC
REGIONAL BRANCH

How?

By Using:

S-Wave Splitting Seismograms

MT - Telluric Current Polarizations

To create

Subsurface Hydrocarbon & Geothermal Maps

"Joint Geophysical Images"

Joint geophysical imaging is the combination of different geophysical methods to produce an accurate model of the earth's crust. The primary techniques discussed in this talk are seismic wave interpretation and electromagnetic resistivity measurements.

The first component of joint geophysical imaging is seismic interpretation. Though large earthquakes occur infrequently, there are thousands of tiny earthquakes occurring every day. These "microearthquakes" can provide us with a huge amount of information about the structures present beneath the surface. As the seismic waves produced by these quakes travel through fractures, fluids, or faults, their properties become altered. By interpreting these variations in seismic waves, we can produce an accurate image of the geological structures beneath the surface.

Magnetotelluric data, taken using portable coils, measures natural currents induced by variations in earth's magnetic field. By monitoring these telluric currents, we can determine the resistivity of the material they travel through. From these measurements, we can see where fracture zones and fluids are present in the crust. When this data is combined with seismic data, an accurate, robust geological model can be constructed.

The goal of joint geophysical imaging is to better understand what is happening beneath our feet without having to risk huge sums of money to drill kilometres under ground. By investing in applied research, industry can both reduce the risk of drilling and further our scientific understanding of the accessible earth—that portion from which our resources come and whose processes and hazards directly impact people.

The Main Points to Understand

What is “S-wave splitting” ?

What is “telluric current polarization” ?

What is “joint geophysical imaging” ?

And

A successful example of a Geothermal Well

The main points to remember are:

1. Joint MEQ and resistivity data suggest that at some high temperature systems, microearthquakes occur mainly above the heat source and on the boundaries between deep low and high resistivity.

2. Strong evidence exists for a correlation between MEQ S-wave splitting, MT-strike direction, fracture induced anisotropy, and at sites close to fluid-filled fracture zones.

Based on these conclusions, the following drilling “hypotheses” are continuing to being tested:

3. The target for drilling high production wells should be at the intersection of structures with high seismic activity and above the interpreted heat source. The priority area is within the damaged zones of the interpreted fracture zone.

4. The drilling targets should be areas that show both S-wave splitting and MT polarization. The drilling should target the fractures that show highest seismicity.

5. Deeper low resistivity zones close to the interpreted heat sources and fracture zones maybe be a target for drilling for super critical steam.

6. The high resistivity zone outside S-splitting and MT polarization interpreted fracture zones are taken as areas of lower temperature and low fracture porosity. These are areas of low geothermal potential.

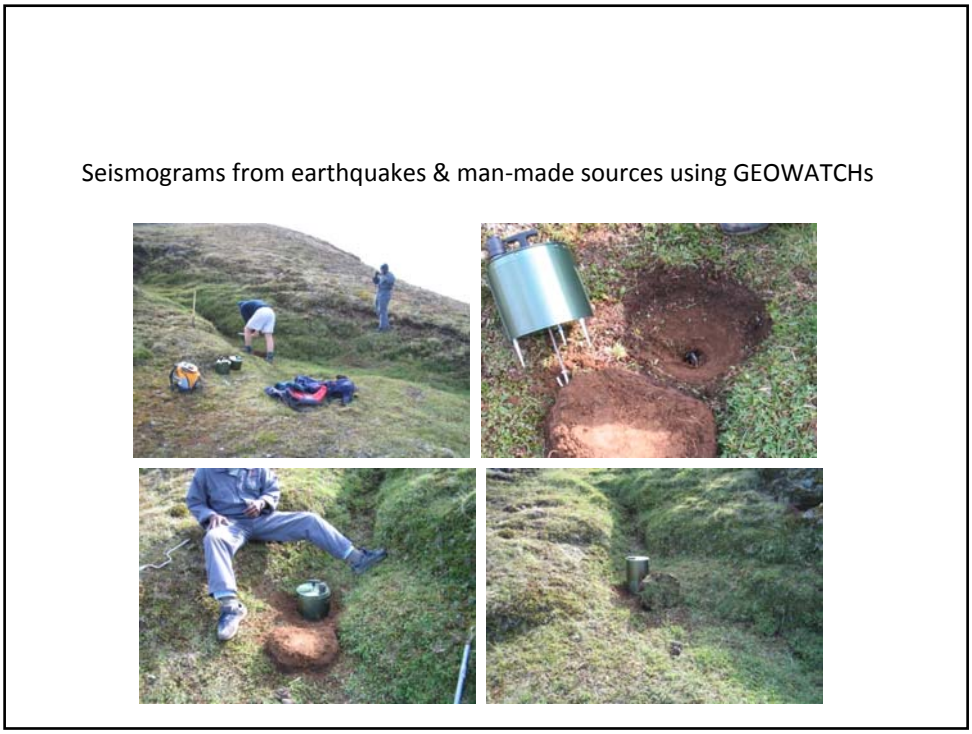

This Geospace GS-1 surface instrument measures microearthquake activity in the earth's crust. It is designed to be theft resistant, runs on a special long-run battery and stores data on compact flash cards.

The unit is a 3-component, 24-bit, 4-channel, digital grade seismometer used in the Iceland example discussed in this presentation was designed for seismic exploration in a variety of terrains. It is designed with a natural frequency of 1 Hertz (Hz), well suited for optimal response to microearthquakes where the driving frequency is expected to be low. The twenty Geospace GS-1 seismometers used for the Iceland study proved to be portable over rough terrain, durable, easy to maintain, and accurate.

The Geospace seismometers functioned well over a variety of conditions. The temperature ranged from –10C to 25C with no discernable effect on the seismometers.

Telluric currents from magnetotelluric sources using PHEONIX MT Recorders

This is a photograph of an IESE-SONDI field crew ready to deploy a set of magnetotelluric sensors in the Krafla Geothermal Field, Iceland.

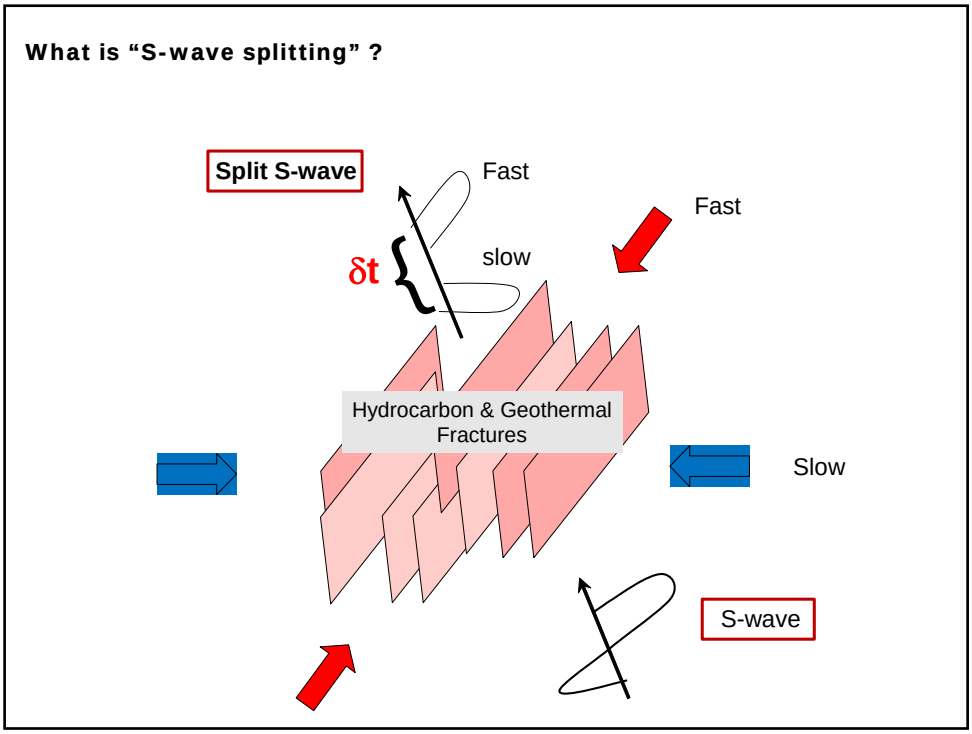

Shear wave splitting occurs when a seismic signal travels through an area of fractured rock. Because seismic waves move easily through contiguous rock, the wave is slowed in one direction. This “splitting” effect can be detected by the directional components of the seismometer.

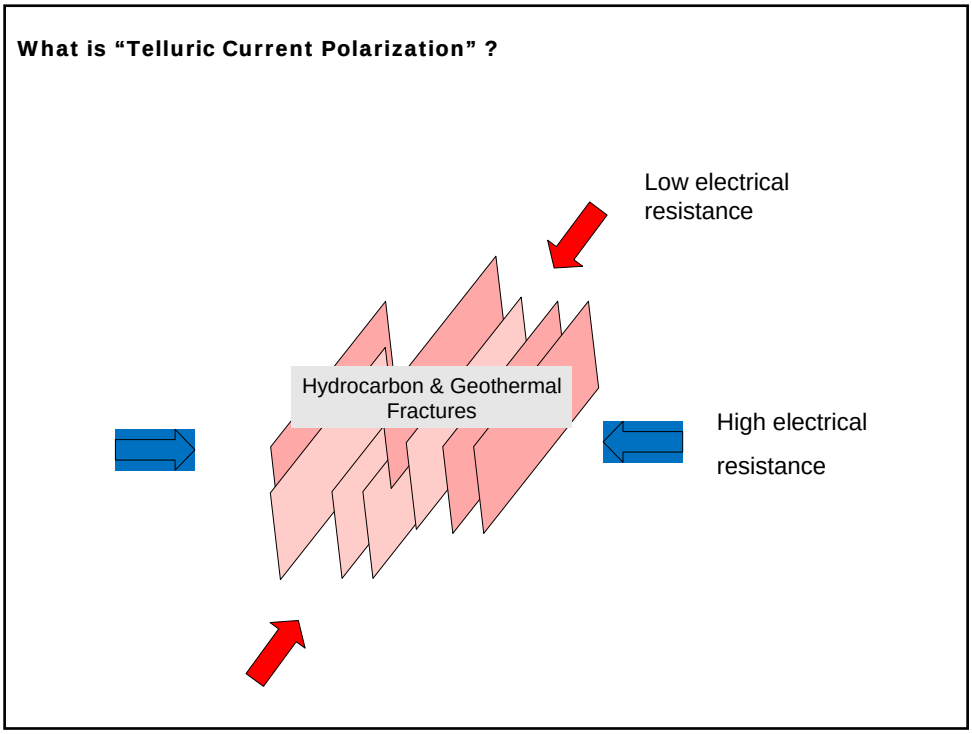

Telluric polarization is similar to shear-wave splitting. By looking at relationship between orientation and resistivity across an area, fracture and fluid-filled zones can be detected. When combined with shear-wave splitting analysis, this is a powerful tool for fracture mapping.

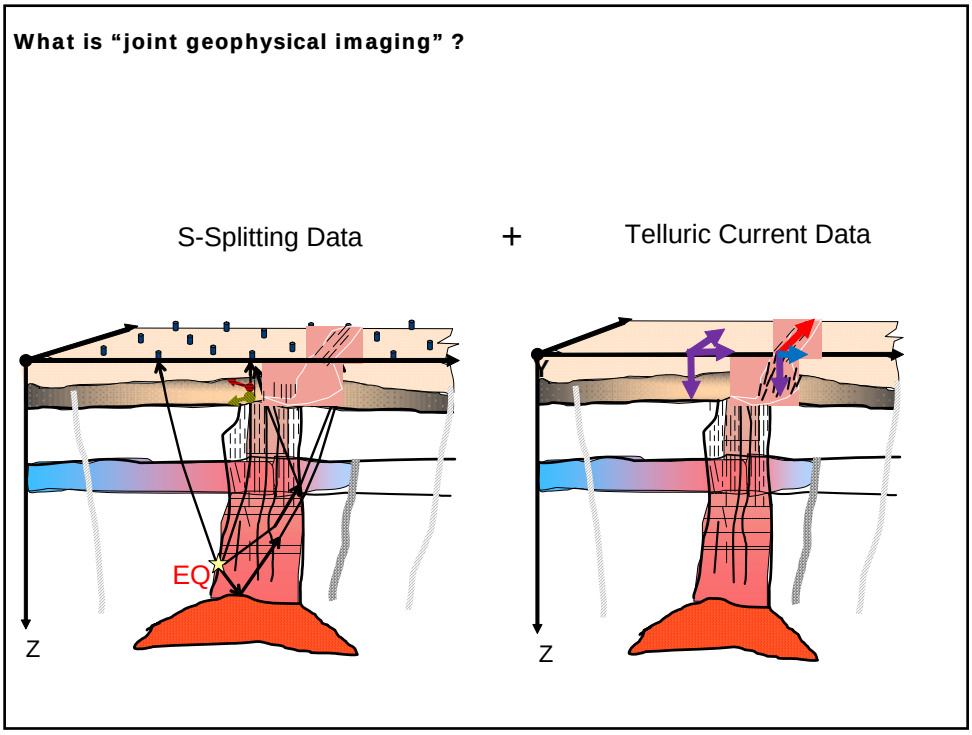

By combining shear-wave splitting data and telluric current data we can create a robust, 3-Dimensional model of the subsurface. This is called “Joint Geophysical Imaging,” which is the combination of different geophysical methods to produce 3D models of the subsurface.

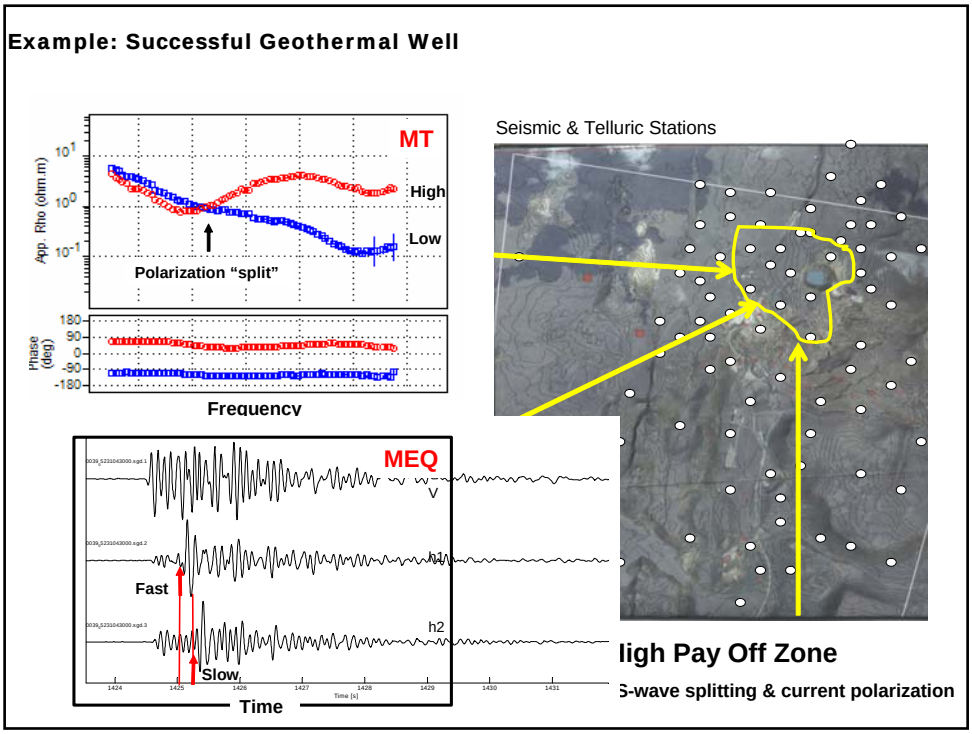

Joint Geophysical Imaging is a powerful, low cost tool for both scientists and industry. In this example, Joint Geophysical Imaging was employed in targeting a location for a geothermal well site. The ability to accurate describe and locate fracture zones greatly decreases the risk of drilling an unproductive well.

HYDROTHERMAL FAULT ZONE MAPPING AT KRAFLA GEOTHERMAL FIELD USING SEISMIC AND ELECTRICAL MEASUREMENTS

Imaging Fractures as Targets for Drilling

Stephen A. Onacha, Eylon Shalev, Peter Malin,
Knutur Arnasson and Bjarni Palsson
April 2007

ABSTRACT

This is a report of the geophysical studies at the Krafla geothermal field based on the use of microearthquakes and resistivity data to characterize fracture zones within the geothermal system. The method uses P- and S-wave velocity, S-wave polarization and splitting magnitude, resistivity and magnetotelluric (MT) strike directions to determine fracture-porosity and orientation. The conceptual model used to characterize the buried, fluid-circulating fault zones in hydrothermal systems is based on geological and fracture models. The method has been tested with field earthquake and resistivity data; core samples; temperature measurements; and, for the case of Krafla, with a drilled well.

The use of resistivity and microearthquake measurements is based on theoretical formulation of shared porosity, anisotropy and polarization. The relation of resistivity and a double porosity-operator is solved using a basis function. The porosity-operator is used to generate a correlation function between P-wave velocity and resistivity. This correlation is then used to generate P-wave velocity from 2-D resistivity models. The resistivity models are generated from magnetotelluric (MT) by using the Non-Linear Conjugate Gradient (NLCG) inversion method.

The seismic and electrical measurements used come from portable, multi station microearthquake (MEQ) monitoring networks and multi-profile, MT and transient electromagnetic (TEM) observation campaigns. The main conclusions in this Study are listed below:

1. Strong evidence exists for correlation between MT strike direction and anisotropy and MEQ S-wave splitting at sites close to fluid-filled fracture zones.
2. A porosity operator generated from a double porosity model has been used to generate valid P-wave velocity models from resistivity data. This approach is being developed further into a joint inversion scheme.
3. Joint interpretation of MEQ and resistivity data shows that at the Krafla high temperature hydrothermal system earthquakes occur mainly above the partially molten magma chamber and on the boundary between the deep low and high resistivity.

4. A high density of fluid-filled fractures bound by less fractured host rocks exists at Krafla. The target for drilling high production wells should be at the intersection of the NW and SE structures especially in areas with high seismic activity that occurs above the interpreted heat source. The priority area is within the damaged zones of the interpreted fracture zone.
5. The location of the drilling targets has taken into account the joint interpretation of resistivity and microearthquake data. The drilling targets should be areas that show both S-wave and MT splitting in the northern part of Krafla. The drilling should target the fractures that show high seismicity. The NW-SE trending interpreted fracture zones define important zones that channel upflow of hydrothermal fluids. Directional drilling can be done from the same well pads to minimize on the environmental impact and also reduce the costs.
6. The study has demonstrated both the value of using both MT and MEQ methods. The study has clearly indentified the heat source for the geothermal system and defined the best targets for production drilling. The best sites are associated with a fracture zone above an interpreted heat source. The fracture zone is defined by a low resistivity anomaly bound by high resistivity. The fracture zone is also associated with earthquakes above a deeper low resistivity interpreted as the heat source for the geothermal system. The deeper low resistivity close to the fracture zone can be a target for drilling for super critical steam.
7. The high resistivity zone outside the fracture zone is interpreted as an area of lower temperature and low fracture porosity. These are areas of low potential for geothermal development.

1.0 INTRODUCTION

1.1 Objectives, motivation of research and background

The objective is to contribute to research, development and industrial applications in the exploration and utilization of geothermal energy. This report addresses the integrated scientific challenges of developing methods to explore new hydrothermal systems and also improve the production from existing geothermal fields.

Costs of geothermal power plants are heavily weighted toward early expenses such as well drilling and pipeline construction. During this stage, analysis of the drilling information is carried out to find the most productive wells. The main risk of developing and the time for construction of the power plants can be reduced by

drilling fewer production wells. For instance in Krafla, within an area covering 3-4 km^2, 34 wells have been drilled. The initial output from the wells ranges from 2.3 to 19.7 MWe (Gudmundsson, 2001), reflecting the variability in permeability in the hydrothermal reservoir. Two wells in the Krafla geothermal field account for over 50% of the steam required to power the installed capacity of 60MWe. Similar well output variability exists in the Olkaria Geothermal field in Kenya where two wells produce 19 MWe for a power station of an installed capacity of 45 MWe. If these high production wells had been drilled at the beginning of the project, there would have been tremendous savings on the infrastructure and the total costs of developing the geothermal power plants. On average it takes about 45-60 days to drill wells to a depth of 2000 m. If we consider the case for Krafla, the drilling of 34 wells took between 4 to 5.5 years of continuous drilling. This makes the rapid implementation of geothermal projects difficult. The goal of this work is to locate the most productive areas of a hydrothermal system, thereby increasing the productivity of the wells that are drilled, and thus reducing the total number of wells and overall costs.

The goal is to map and locate buried fluid-filled faults zones that can be targets for drilling high production wells. The scientific and application challenge is to map the fault zones and determine their size, orientation and depth. The objective of this dissertation is to combine microearthquake and electrical resistivity data to image fault zones and determine fracture porosity. Microearthquake and resistivity measurements are used to map buried faults zones and heat sources for hydrothermal systems in regions of extension tectonics. Resistivity measurements are indirect geothermometers through their association with temperature sensitive clays that have high interface conduction (Flovenz et al., 2005, Arnasson, 2000). Resistivity is also an indicator of the fluid content especially for fluid-filled fractures.

Typically, high-fracture porosity is found at fault tips, fault bends and jogs, and fault intersections. When these structures occur near geothermal heat sources, they provide important upwelling paths for hydrothermal fluids. Such zones are excellent targets for exploratory drilling, with the potential to significantly lower the number of wells needed to both delineate a reservoir and place it into economic production.

Hydrothermal systems are geologically complex areas and usually the foci of intense tectonic and volcanic activity. Heat sources for hydrothermal systems include magma chambers, young dikes, and frictional heating due to faulting (Lanchenbrunch, 1978). These processes are expected to produce changes in the rock properties that may be detected by both resistivity and seismic velocity

measurements. In most cases, fault zones are buried by repeated volcanic eruptions and lava flows. The challenge in understanding fluid circulation in hydrothermal systems depends on the ability to map the buried fluid-filled fractures. Although most of the deep up-flows are found near vertical fault zones, some lava rocks like breccias have dominant primary permeability. The limitation of mapping fluid-filled buried fractures can be mitigated by using both seismic and electrical measurements.

Resistivity methods have been used in hydrothermal exploration for many years. Calibration of this method against drilling results has been done in several geothermal fields, and it is apparent that resistivity measurements can be used as a subsurface thermometer (Arnasson, 2000). This indirect spatial correlation between resistivity and temperature is associated with the local degree of hydrothermal alteration. Most high-temperature hydrothermal systems are associated with a low resistivity layer over the geothermal reservoir due to clay mineral alteration (Arnasson et al., 2000., Flovenz et al., 2005). Because resistivity methods can be used to interpret temperature, hydrothermal alteration and permeability, they offer a means for resolving the geometry of the hydrothermal reservoir, depth to hydrothermal reservoir, fracture zones and permeability distribution. Resistivity variations are usually related to salinity, water saturation, porosity, and cation exchange capacity in hydrated clays (Cumming, 2000, Ussher et al., 2002, Flóvenz' et al., 2005). Understanding the low resistivity distribution can contribute to the location of the high temperature upflow zones as targets for drilling. The resistivity distribution is also used in evaluating depth to the geothermal reservoir and dimensions of the heat source. In this dissertation, both Transient Electromagnetic (TEM) and magnetotelluric (MT) resistivity data were used.

In the MT method, the resistivity properties of the rocks are determined from the measurements of orthogonal components of the natural time varying electrical and magnetic (EM) fields. The electrical fields are measured by two sets of orthogonal non-polarizing electrodes and the magnetic field is measured by induction coils. In this study, MT measurements acquired at frequencies of 400-0.0025Hz were used.

EM fields propagate into the earth as coupled E- and H- fields which are commonly represented in the frequency domain as a four element impedance tensor. The apparent resistivity is obtained from the scaled ratio of the electric field to the magnetic field. If the subsurface is two-dimensional, EM fields are usually polarized into two modes usually referred to as TE-mode when the E fields are parallel to the direction of strike and the TM-mode when the H-field is parallel to the strike direction.

One of the problems in the interpretation of MT data is the static shift. The shift is caused by shallow polarization of the EM fields by local resistivity contrasts at the scale of the measurement dipole (in this study 50-70 m) that lead to a constant vertical displacement of the MT apparent resistivity curve on a log scale at all frequencies.

The evaluation of the relationship between porosity and resistivity and porosity and P-wave velocity is used as an initial step in developing a mathematical formulation for a Joint Geophysical Imaging (JGI) method that combines both MT resistivity and MEQ data. The relationship between resistivity and shear wave anisotropy is used as a useful tool of imaging the depth, size and orientation of fluid-filled fractures. In this structural approach, the study assumes that changes in acoustic impedances and resistivity occur at the same structural boundary due to variations in porosity.

The objective of joint imaging is to map the subsurface location, orientation, and size of fracture zones and fractures. This research presents evidence of local correlations between MT polarization and S-wave splitting directions, directions that also match some of the known geological and tectonic settings.

This is an effort to contribute to the ongoing research in the scientific community to carry out joint interpretation of geophysical data to constrain models obtained by different inversion schemes. The tasks undertaken are listed below:

1. Jointly interpret TEM and MT data. The TEM and MT data was used in joint interpretation to correct for static shifts inherent in MT methods. 1-D models generated from TEM data in the vicinity of the MT measurements were used to correct for static shifts. The MT curves have been analyzed to extract information on lateral variation in resistivity and physical parameters that give evidence of the presence of fluid circulation in the hydrothermal systems. In particular, the MT data was analyzed to determine the dimensions of conductive zones that coincide with the rank of hydrothermal alteration; this can be a proxy for either relict hydrothermal systems or the temperature of the hydrothermal fluids. In MT methods when the magnetic field is polarized along the strike direction, then the current density at a lateral resistivity interface is discontinuous; this is known as the TM mode. As pointed out by Wannamaker (1999), lateral changes in resistivity are often derived from TM mode impedance. Recent 2-D numerical modeling studies indicate that closely spaced TM mode MT data can be used to locate a fault zone (Ingham, 2005).

2. Reduce, analyze, and interpret Krafla data sets for the types of electrical and microearthquake signatures associated with local tectonics. This includes locating earthquakes.
3. Analyze microearthquakes to establish whether they have characteristic signals associated with tectonic movements, fluid movement in the upflow zone, and fluid movement in the down-flow zone. The pores, cracks, fractures, fissures, joints, faults, and the internal rock structures are important in controlling the storage and transmission of fluids in rocks. This study takes into consideration that several theoretical formulations to study seismic propagation in porous or fractured medium have been developed over the years (Hudson, 1981., O'Connell, 1974), but their field applications have been limited. The physical properties of porous media are usually determined by evaluating the interaction between the solid grains and pore fluid, parameters that characterize the structures, and the coupling mechanisms between the solid matrix, fluid, fractures and pressure. Pressure changes caused by mechanical coupling between solid grains, pore fluid and the interconnection of the pores in the hydrothermal reservoir can create changes in the bulk density of the rocks (Maultzsch et al., 2003). This change in bulk density can then cause velocity gradients within the hydrothermal system.
4. Determine the local seismic wave velocity and electrical resistivity structure of the hydrothermal systems, as much as is possible with publicly available modeling codes. In this research, the resistivity structure is used to constrain the velocity model. Initial velocity models will be based on the depths to the resistivity interfaces of 1-D resistivity sections. Then make use of the expanded Krafla seismic data set from 2004 and 2005 to study S-wave splitting for evidence of fractures. This is achieved through analysis of shear wave polarization and travel times delay caused by anisotropic properties of the propagating medium.
5. Evaluate and model the evidence that MT strike orientations correlate with S-wave splitting directions. S-wave splitting is usually caused by aligned systems of open, fluid-filled micro-fractures. Since the primary target for productive geothermal wells is faults and fractures, it is expected that this anisotropy would be diagnostic of the variability of the factors that affect fluid flow. In this dissertation, it is anticipated that such a relationship can be used to map out the depth and location of fracture systems.

1.2 Geology and tectonic setting of the Krafla hydrothermal system

The Krafla hydrothermal system is located within an interpreted caldera that lies at the boundary of the North American and European plates along the Neovolcanic Zone (NZ). The NZ zone, which has an estimated spreading rate of 0.9cm/year, occurs along the Mid-Atlantic Ridge (MAR) in northeast Iceland. The NZ lies along the Mid-Atlantic Ridge (MAR) that extends from the Reykjanes Ridge in the south to the Kolbeinsey Ridge in the north. The NZ is composed of three main branches, the Northern Volcanic Zone (NVZ), the Eastern Volcanic Zone (EVZ) and the Western Volcanic Zone (WVZ). The NZ is composed of central volcanoes and fissure swarms (Figure 1).

The geology of the Krafla area is dominated by basaltic lava, hyaloclastites, and intrusives. The caldera was formed about 100, 0000 years ago (Saemundsson, 1974, 1978, 1981; Armannsson et al., 1987) . Rhyolitic volcanism identified at Krafla has been attributed to silicic melts due to basaltic intrusion into the crust. It is postulated that the source of the Rhyolite rocks is an active rhyolitic magmatic source at temperatures of about 850-950°C on the periphery of a larger basaltic magma chamber (Jonasson, 1994).

The volcanic activity in this area is episodic, occurring every 250-1000 years, with each episode lasting 10-20 years (Armannsson et al., 1987) . This episodic volcanic activity affects the hydrothermal system by opening new factures and injecting magmatic gases, mainly carbon dioxide and hydrogen sulfide. The rifting process changes the fluid flow regimes, and the magmatic gases change the composition of the hydrothermal fluids. The last volcanic period started at the end of 1975 and ended in September 1984 with 21 tectonic events and 9 eruptions (Gudmundsson et al., 2001). This volcanic activity occurred along a fissure and released volcanic gases into the hydrothermal reservoir. From studies of S-wave shadows, it has been postulated that a cooling magma chamber exists at a shallow depth of 3-8 km below the hydrothermal field (Einarsson, 1978). The Krafla volcanic system is transected by a fissure swarm (Figure 2), which is 4-10 km wide and trends in a near north-south direction (Björnsson, 1985) . The hydrothermal manifestations are controlled by tectonic fractures, faults and dykes.

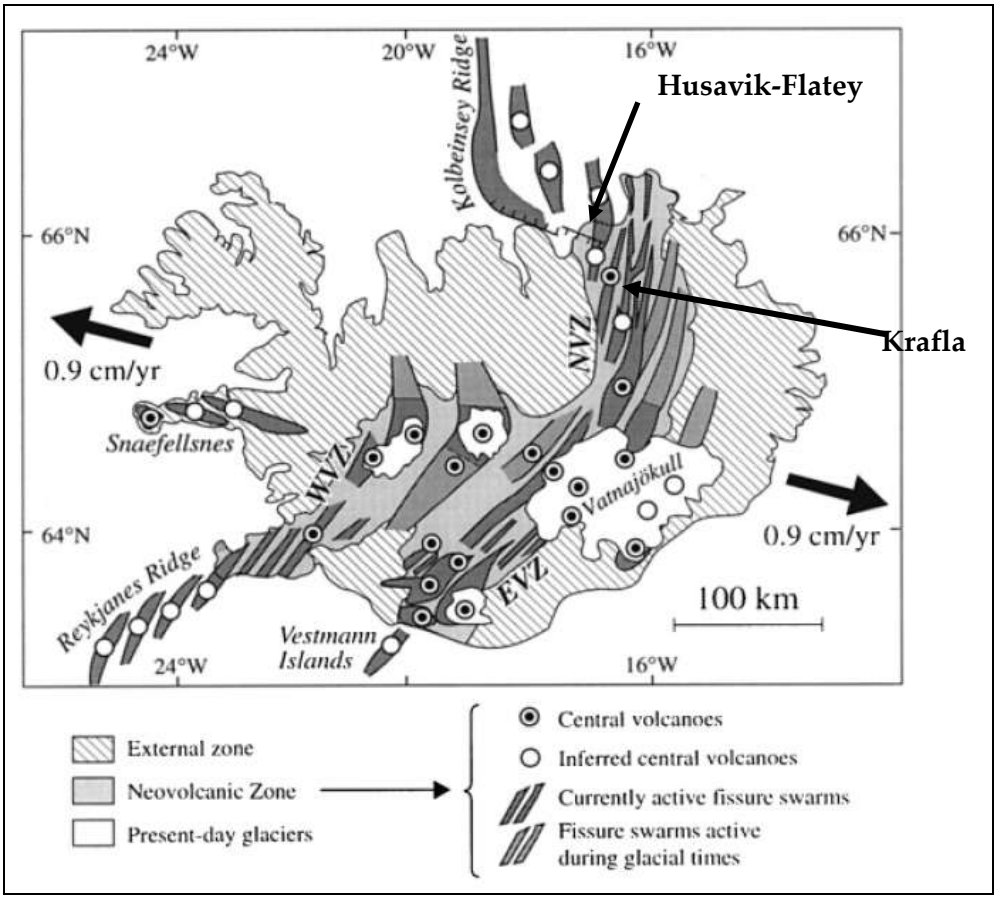

Figure 1: Geological and tectonic setting of Iceland. The Krafla hydrothermal area occurs along the Mid-Atlantic Ridge (MAR) and within the Neovolcanic Zone (NZ). The NZ extends from the Reykjanes Ridge to the Kolbeinsey Ridge in the north. The Neovolcanic Zone is composed of three main branches, the Northern Volcanic Zone (NVZ), the Eastern Volcanic Zone (EVZ) and the Western Volcanic Zone (WVZ).

A geological cross section (Figure 3) in an NW-SE direction across the hydrothermal system shows three stratigraphic units. The upper layer is made of young lava (less than 10,000 years) and a hyaloclasite formation up to a depth of about 200-300m.

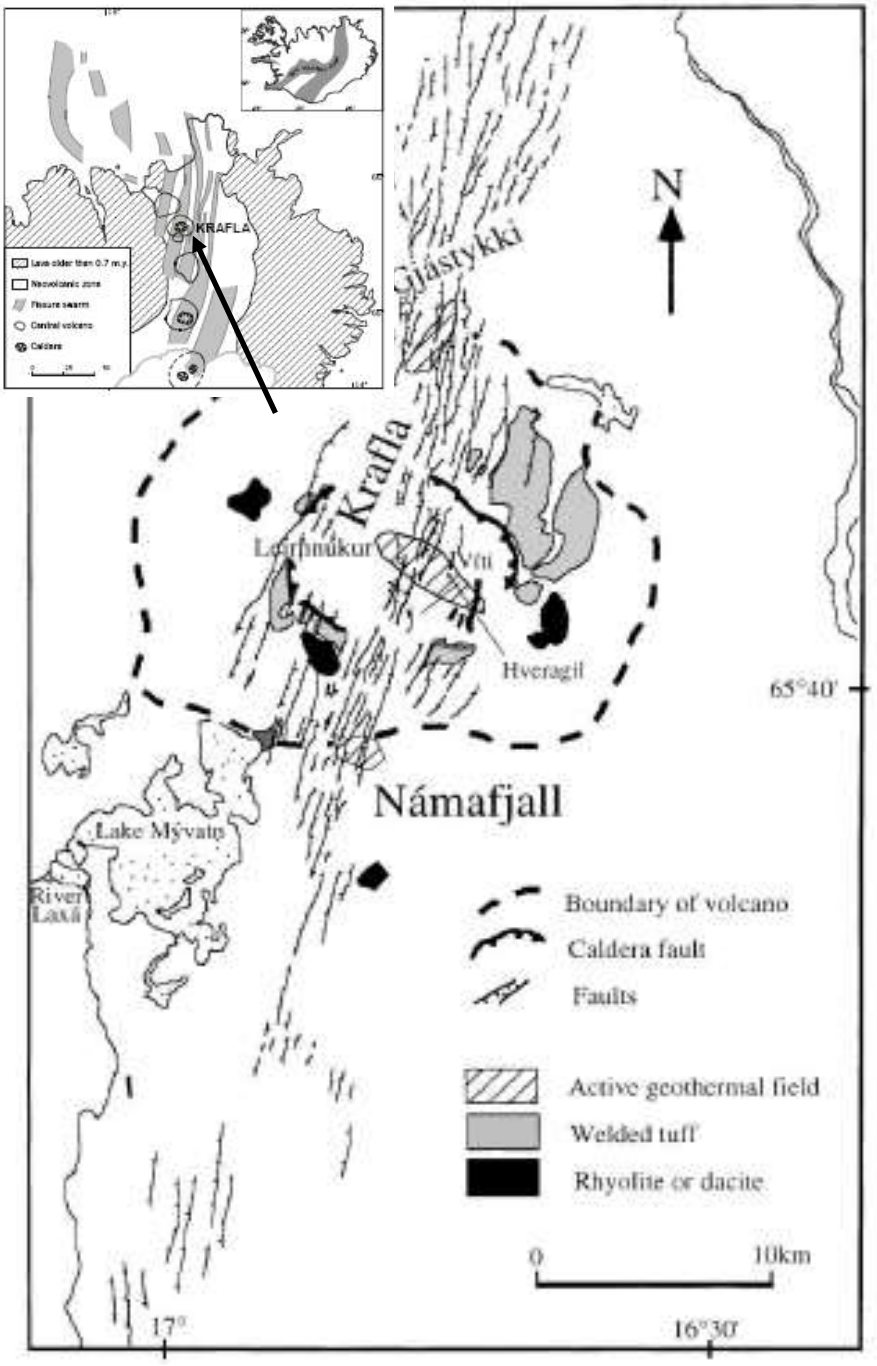

Figure 2: Geological and structural model of the Krafla hydrothermal system. The caldera faults have a NW-SE trend while the faults within the volcanic zone have an N to NNE trend. Welded tuff and Rhyolite deposits occur at the margins of the caldera.

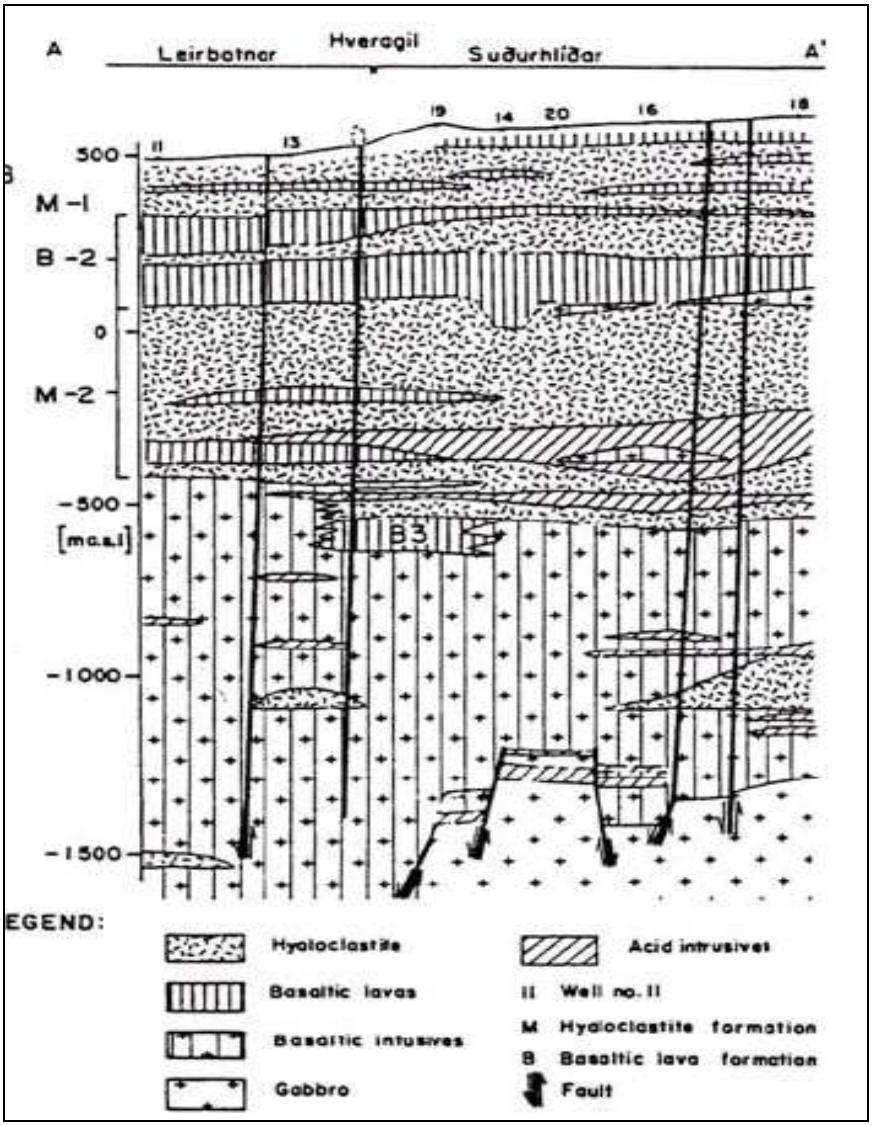

Figure 3: Geological section in a NW-SE direction across the Krafla hydrothermal system. Surface layers to a depth an elevation of 500 mbsl are dominated by hyaloclastites and basaltic lava flows. Below 500 mbsl, basaltic intrusions, minor acid intrusions, and gabbros dominate (Armannsson et al., 1987).

The second group is made of lava and hyaloclasite rocks up to a depth of 1000-1300m (Armannsson et al., 1987). The third stratigraphic unit consists of basaltic lavas with doleritic and minor gabbroic intrusives to a depth of 2000-2200m. This geological section has been used to constrain the geophysical model. In this study, it is assumed that the first two stratigraphic units form the capping unit for the hydrothermal system and are expected to be nearly isotropic and homogenous. The near surface lateral changes are attributed to channeling of hydrothermal fluids along faults and dykes. The third stratigraphic unit is assumed to be anisotropic and

therefore forms the basis of this study to evaluate the anisotropic effects on both MT and MEQ data.

1.3 The Krafla hydrothermal system

Drilling of geothermal production wells focused on intersecting known fractures and intrusion boundaries at a depth of 800-2100m. This strategy was aimed at obtaining geothermal wells with high mass flow rates. Additional hydrothermal exploration was carried out between 1984 and 1996 to locate hydrothermal fluid with low magmatic gases and also to find replacement wells for some of the wells damaged due to tectonic movements. Although some of the wells were targeted in the known fracture zones, the production was still low. This highlights the problem of targeting fracture zones for drilling production hydrothermal wells. Analysis of drill cuttings from the wells has facilitated the evaluation of the distribution of individual lithological units, correlation of aquifers with lithology, and the degree of hydrothermal alteration. Intrusive rocks are dominant below 1200-1300m depth and are therefore expected to contribute to the spatial channeling of hydrothermal fluids.

A total of 34 wells have been drilled at Krafla within an area covering 3-4 km^2. The initial output from the wells ranges from 2.3 to 19.7 MWe , reflecting the spatial variation in permeability across the hydrothermal system. Two wells in the Krafla hydrothermal system account for over 50% of the steam required to power the installed capacity of 60MWe. Similar well output variations exist in other hydrothermal systems like Olkaria in Kenya where two wells produce 19 MWe for a power station of an installed capacity of 45 MWe.

The Krafla hydrothermal area is divided into three fields: Leirbotnar, Sudurhlídar and Hvíthólar fields. Although the sectors are within a caldera, the drilled wells show big differences in fluid chemistry, temperature and pressure. The Leirbotnar hydrothermal system is divided into an upper and a lower zone (Stefansson and Steingrimsson, 1980) . The upper reservoir is water saturated and has a depth of 1000m with a mean temperature of 205°C. The main aquifers in the lower zone are associated with fissures and intrusives. This lower zone is boiling with temperatures ranging from 300 to 350°C. The Sudurhlídar field is a boiling system while the Hvíthólar field exhibits boiling characteristics down to a 700m depth with a temperature reversal (Armannsson et al., 1987).

1.4 Previous resistivity studies at Krafla

DC resistivity data has been used to establish a general relationship between bulk resistivity of rocks, porosity and temperature for the upper crust in Iceland (Flovenz et al., 1985). The resistivity structure depends on the age of the volcanic rocks. The resistivity in the high-temperature hydrothermal systems is low (1-10 Ωm) at a depth of 500-800m. In the areas of older Quaternary volcanism, typical resistivity at a depth of 200-500m is 100-1000 Ωm.

Electromagnetic measurements have been used extensively to study the hydrothermal systems in Iceland (Árnason et al., 2000) . A major finding of this work is that all high temperature hydrothermal systems have the same resistivity structure characterized by a low resistivity cap at the outer margins of the hydrothermal system and an underlying more resistive core within the reservoir. The low resistivity has been interpreted as a zone dominated by low temperature (100-200˚C) alteration of rocks to clays. In this clay zone (depth up to 1000m), the resistivity is controlled by both ionic and interface conduction. Below the clay cap, the resistivity is dominated by interface conduction and generally the resistivity increases with depth (Flovenz et al., 2005). Analysis of core samples from the chlorite show significant interface conduction. This result gives further evidence that interface conduction is the dominant conduction mechanisms in most high temperature hydrothermal systems (Flovenz et al., 2000; Flovenz et al., 2005).

1.5 Previous local seismic activity and velocity studies at Krafla

A microearthquake study around the Krafla hydrothermal system in 1967 and 1968 (Ward and Björnsson, 1971) showed a high level of seismicity with an average of 191 events per day in 1967 and a low level of seismicity with an average of 1.2 events per day in 1968. The unusually high level of seismicity was attributed to the inflation of a magma chamber beneath the hydrothermal system at Krafla (Ward and Björnsson, 1971).

The seismic structure of the Krafla central volcano is characterized by extreme variations in P-wave velocity (Brandsdottir et al., 1995). The resistivity structure is therefore also expected to show these extreme variations. The near surface structure as determined from the seismic undershooting experiment showed that the upper-most 2.5 km is almost isotropic. Based on the results of a 0.2-0.3s P-wave delay and shear wave shadowing, the preferred interpretation by Brandsdottir et al. (1995) was that the Krafla magma chamber has a width of 2-6 km wide and elongates in a NW-SE direction across the rift zone with a thickness of 0.75-1.8 km (Figure 4).

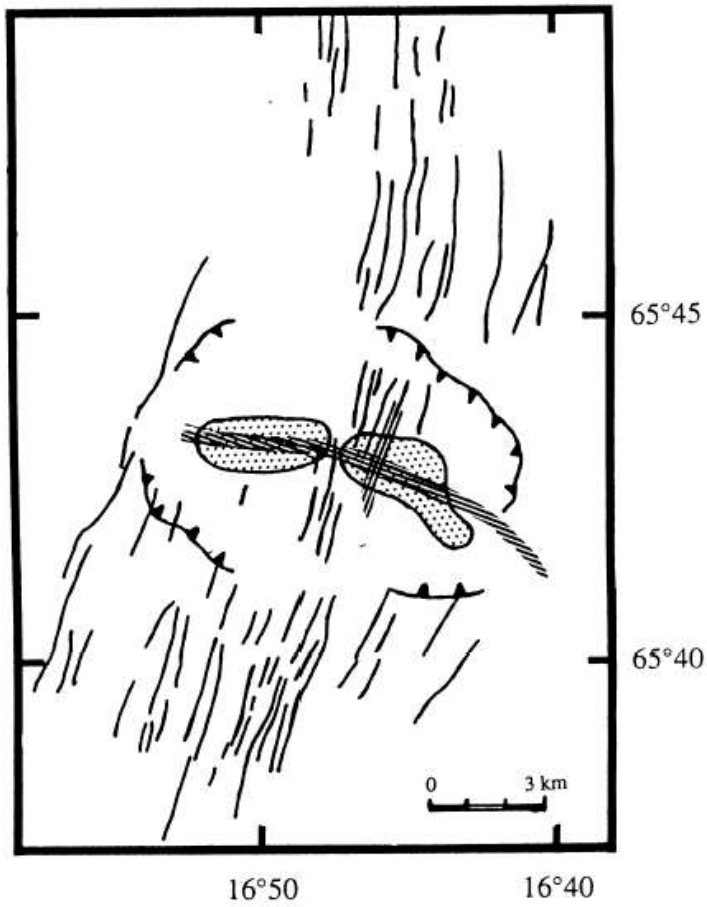

Figure 4: Map of the Krafla caldera showing the fissure swarms, shear wave attenuation zones (shaded regions) delineated by Einarsson (1978), and the P-wave attenuation (stripped zones). The P-wave attenuation zones cut across the NNE fissure swarm and extend 3km NS and 10 km EW (Brandsdottir et al., 1995).

2.0 Conceptual model and theoretical formulation for imaging fault zones using microearthquake and electrical measurements

2.1 Conceptual model

2.1.1 Geophysical and geological model of the hydrothermal systems

The geophysical and geological model assumes that the porosity within the deep hydrothermal reservoir is dominated by fracture porosity. This is consistent with studies based on the properties of more than 500 samples of igneous rocks in Icelandic hydrothermal systems. These studies show that total porosity is equivalent to effective porosity (Sigurdsson et al., 2000). The data analysis of igneous rock properties in Iceland by Sigurdsson et al. (2000) indicates that matrix permeability is related to the capillary tube model, and therefore, the model used is that the flow of fluids in the hydrothermal systems is controlled by fracture porosity, temperature, pressure gradients, and the size and orientation of faults and dykes.

Recent studies on core samples from the chlorite zone in geothermal wells in Iceland (Flovenz et al., 2005), found that temperature dependence of conductivity is at least twice as high for interface conduction as for pore fluid conduction. The conclusion is generally that interface conduction is the dominant conduction mechanism for high temperature geothermal fields regardless of fluid salinity (Flovenz et al., 2005).

The model (Figure 6) used in this study consists of a fault zone, defined as a zone of high fracture porosity which is made up of a core bounded by a damaged zone embedded in a host rock. The fault zone is overlain by a clay cap and recent volcanic rocks. The core and the damaged zones are modeled regions of low and high resistivity, respectively. The host rock is expected to have the highest resistivity.

The conceptual model of the hydrothermal system close to the fault zone is therefore postulated as follows:

1. A surface layer of recent volcanic rocks or pyroclastics with variable resistivity depending on the age of the rocks and proximity to the fault zone. Areas close to the hydrothermal system are modeled as low resistivity zones formed by the alteration of the rocks to low temperature clays. Areas with young basaltic, Rhyolitic and Trachytic rocks are expected to have higher resistivity.

2. The second layer with variable thickness is formed by a clay clap due to alteration of rocks by lateral movement of hot (180-240 ˚C) hydrothermal fluids. The clay cap is probably formed by the interaction of meteoric water and gases from the deep hot hydrothermal reservoir. The interaction of the gases and meteoric water may form acidic condensates that alter rocks into clays. The outflow direction of the hydrothermal system may be controlled by the hydrogeological gradient.

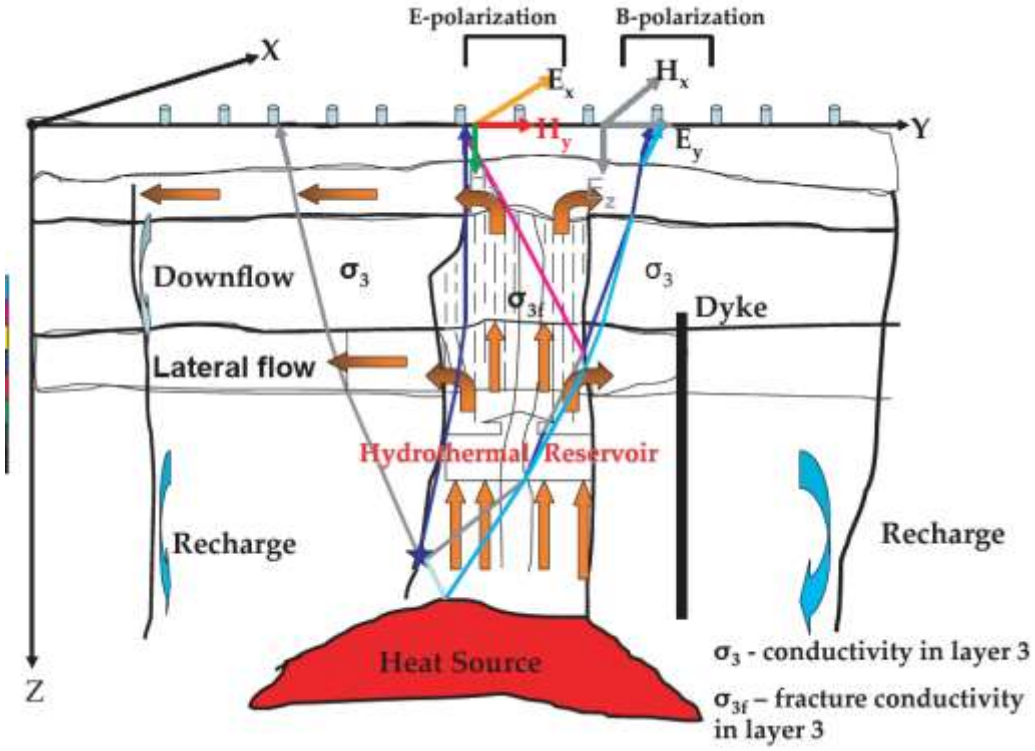

Figure 5: The conceptual model used for the development of a joint geophysical imaging method using collocated resistivity and earthquake measurements. In this model, the fracture zone is defined by low resistivity and P-wave velocity within a host rock with high resistivity and P-wave velocity. The clay cap occurs above the hydrothermal system and the heat source. Earthquakes occur above the heat source at the contact between low and high resistivity. Conversions of S-waves to P-waves occur on top of the heat source. The resistivity contrasts below the clay cap cause polarization and splitting in the MT data.

3. In high temperature hydrothermal systems, the third layer is expected to have a higher resistivity due to either a higher rank (chlorite or mixed chlorite and illite) of hydrothermal alteration or low temperature and fracture porosity. The buried fault zone is postulated

to have a lower resistivity due to circulation of hydrothermal fluids and high fracture porosity. The fault zone is also associated with shear wave splitting. Lateral flow within this zone may be controlled by a series of dykes and intrusives.

4. The heat source for the hydrothermal system is a partially molten magma chamber at a depth of more than 3km below the fault zone. The partially molten magma chamber is postulated to have low resistivity.
5. The resistivity contrasts at the fault zone produce anisotropy /heterogeneity and polarization both in MT data and shear wave splitting. The anisotropy in MT data is assumed to be due to resistivity contrasts at the base of the clay cap rather than near surface lateral changes (this is based on the geological model of the fault zone). The MT polarization is assumed to have the same orientation as shear wave polarization.
6. Stresses on the boundary faults and at the boundary of the heat source and host rock produce microearthquakes. It is postulated that microearthquakes produced above the heat source reflect off on the boundary of the heat source causing conversions of the S-waves to P-waves.

2.1.2 Geological and structural justification for the model

The geophysical model is based on the geometry of a buried fault zone within a host rock (Gudmundsson et al., 2002). This model is based on the observations of systems of mineral veins in the damaged zone of the Husavik-Flatey Transform Fault Zone with a NW-SE trend (See Figure 1). The fault zone is about 2-3 km wide and is covered by either volcanic pyroclastic rocks or fresh volcanic rocks. The fault zone is divided into a fault core bounded by damaged zones on either side (Figure 6). The core may be formed by tectonic gouge and breccia; the damaged zone is formed next to the core, and it consists of breccia and fractures of different sizes (Evans et al., 1997). Based on this model, the fracture zone may be a target for drilling high production geothermal wells.

Intense fracturing can form a zone of high permeability that can allow the flow of hydrothermal fluids. The contact between the fault zone and the host rock may form a barrier to deep lateral fluid flow. This barrier may form a significant confining structure for the upflow of high pressure hydrothermal fluids. The assumption is that the fault zone (the size may vary within hydrothermal systems) is expected to have lower resistivity with the lowest resistivity within the core. The host rock is postulated to have high resistivity and high P-wave velocity.

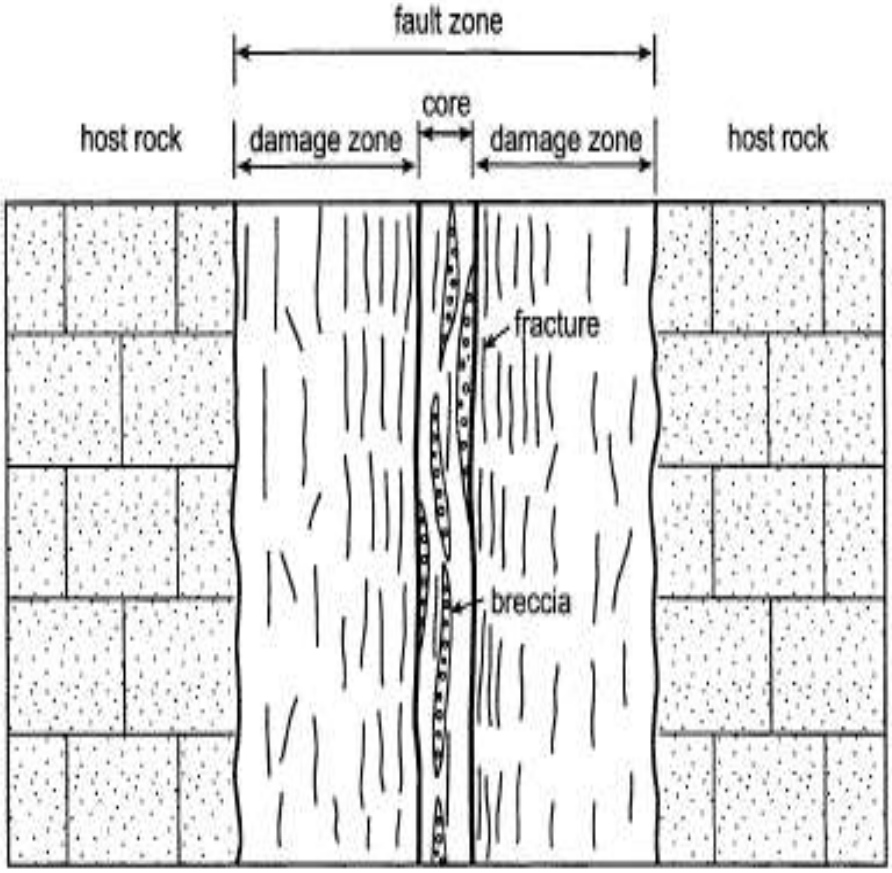

Figure 6: The structural model of a fault zone showing the core, damaged zone and the host rock. Fault displacement generally occurs either at the core or at the contact with the damaged zone. Fluid flow within the damaged zone can be modeled as flow through a fractured medium (after Gudmundsson et al., 2002).

2.2 Theoretical formulation for joint microearthquake and resistivity imaging

The theoretical formulation for 1-D and 2-D joint geophysical imaging of fracture zones within hydrothermal systems is based on the relationship between resistivity, seismic velocity (both P and S velocities), temperature, fluid saturation, and porosity. It is further assumed that, there exists a spatial relationship between shear wave splitting and the polarization in MT data. A new formulation for determining fracture porosity based on MEQ and MT measurements have been developed. The joint imaging approach using fracture porosity is based on the assumption that both shear wave splitting and MT polarizations are caused by aligned, fluid-filled fractures. The amount of fluid, fracture intensity and orientation therefore

determines the response of MT and MEQ measurements observed by surface arrays of instruments.

The key to mapping rock formations is to understand the factors that affect seismic velocities. The major factors are density of the rocks, porosity, number of fractures in unit volume of rock and temperature. All these factors also affect the bulk resistivity of rocks. The bulk modulus of the rocks relates strain due to an applied stress.

When the medium is elastic and isotropic, the velocity can be expressed as a function of bulk modulus (κ) and shear modulus (μ). In an isotropic medium, elasticity can be expressed by Lame's coefficients λ and μ. The bulk modulus (incompressibility) relates the change in pressure to the change in volume. Other important coefficients are the Young's modulus (E), which relates the longitudinal stress and strain in the same direction and Poisson's ratio (σ). The Poisson's ratio relates strain in mutually orthogonal directions due to stress in one of the directions. The shear modulus (rigidity) relates changes in form without change in volume.

2.2.1 Relationship between resistivity, P-wave velocity and porosity

2.2.1.1 Relationship between resistivity, temperature of pore fluid and fracture porosity

The main objective is to determine a way of quantifying fracture porosity which can be used to estimate the amount of hydrothermal fluids and also the orientation of the fractures. The amount of hydrothermal fluid stored per unit volume (storage capacity) within the rocks depends on the thickness of the formation and fracture porosity.

It is assumed that porosity below the clay cap is mainly controlled by fracture porosity. This is based on observations that formation of zeolites and clays are dependent on the influx of pore fluid. This process is generally very slow in rock matrix. It is therefore, generally assumed that only fracture porosity contributes significantly towards interface conduction from clays (Flovenz et al., 1985). The total hydrothermal reservoir storage capacity is therefore a function of the fracture intensity within the fault zone.

The analysis of fracture porosity is based on the comparison of the solution of a volume averaged resistivity equation and a modified double porosity model. In the volume average equation, the measured resistivity of the rocks is related to porosity, percentage of clay, resistivity of clay, saturation of the geothermal fluids,

resistivity of the fluids and the resistivity of air in the fractures or the voids as shown below:

$$1/\rho = ((1-\Phi)(1-P_c))/\rho_b + P_c(1-\Phi)/\rho_c + \Phi S_w/\rho_w + \Phi(1-S_w)/\rho_a \qquad 2.1$$

Where ρ, ρ_b, ρ_w and ρ_a are the measured resistivity (including fractures), resistivity of rock matrix, resistivity of clay, resistivity of the hydrothermal fluids (water) and resistivity of air or steam, respectively. S_w is water saturation, Φ is porosity and p_c is percentage of clay. This approach is better than models based on Archie's law which is a good approximation for rocks where the conductivity is dominated by pore porosity only.

If we consider the rocks in the hydrothermal reservoir below the clay cap, and assume maximum fluid saturation and interface conduction by chlorite clays, then the measured resistivity is controlled by fracture porosity, the bulk resistivity and the resistivity of the hydrothermal fluids.

In the double porosity model which is based on the relationship established by Flóvenz' et al. in 1985, the measured resistivity is related to the matrix porosity, fracture porosity, resistivity of the geothermal fluids and an empirically defined factor (**b**) which relates degree of fracturing as shown below:

$$\frac{1}{\rho} = \frac{0.22}{\rho_w}\left[1-(1-\Phi_f)^{2/3} + \frac{(1-\Phi_f)^{2/3}}{1+(1-\Phi_f)^{1/3}+(1-\Phi_f)^{1/3}4.9x10^{-3}}\right] + \frac{\Phi_f^{1.06}}{b} \qquad 2.2$$

$$\rho_w = \rho_{wo}/[1+0.023(T-23)] \qquad 2.3$$

$$b = 8.7/[1+0.023(T-23)][1+0.018(T-23)] \qquad 2.4$$

The equation by Flóvenz' et al. (1985) was based on the double porosity model that takes into account the matrix and fracture porosity. This model also takes into account effect of temperature and pore fluid. The model takes into account conduction through the fracture interfaces. The observed measurements of resistivity on laboratory samples of basaltic rocks showed that resistivity was dependent strongly on temperature and interface conduction associated with chlorites in the hydrothermal system.

The first step is to analyze the dependence of pore water resistivity on temperature using equation 2.5 which indicates that for a reservoir saturated with meteoric

water with a low percentage of dissolved salts, the pore water resistivity is expected to be close to that of water at room temperature which is about 2.5 x10^5 Ωm at 23˚C. Empirical analysis of the relationship between resistivity and pore fluid temperature of fresh water shows high resistivity of more than 10,000 Ωm for a temperature range of 100-400˚C.

In hydrothermal systems with geochemical data, the pore fluid resistivity can be determined from the total dissolved solids (TDS) in g/l using the empirical relationship by Block, (2001) as shown below:

$$\rho_w = 4.5TDS^{-0.85} \qquad 2.5$$

In the Krafla hydrothermal system, the average TDS is about 800 ppm, which is equivalent to 0.8 g/l. Substituting the average TDS in equation 2.5, gives a pore water resistivity of about 5.4 Ωm. In comparison, sea water has a TDS of about 30 g/l, which gives an equivalent pore water resistivity of 0.25 Ωm.

Analysis of empirical results for the resistivity of water for 10 Ωm and 2 Ωm are plotted against the temperature range of 0-400°C, it is clear that for very low pore resistivity, and there is very little variation in resistivity with increase in temperature. The variation is significant for high resistivity of water and at low temperatures.

Analysis of the empirical results shows that the pore fluid resistivity for hydrothermal fluids of resistivity at 2 Ωm is given as shown below:

$$\rho_w = 50.381T^{-9145} \qquad 2.6$$

For a reservoir temperature of 240°C below the clay cap, the resistivity of the hydrothermal fluids would be 3.4x10^{-1}.

An important step in determining the relationship between resistivity and porosity involved empirically determining the value of **b** in equation 2.4 for a temperature range of 50-400˚C. The empirically calculated values were plotted against temperature. The value of **b** is higher and changes more rapidly at low temperatures below 150˚C. For high reservoir temperatures (>200˚C), the value of **b** is low and changes very gradually.

For the purpose of evaluating fracture porosity below the clay cap, the reservoir temperature for high temperature hydrothermal systems from down-hole temperature measurements is about 240˚C. The value for the **b** factor for

hydrothermal fluids at 240°C is $2.9x10^{-1}$. This relationship shows that the **b** value in the double porosity model in equation 2.2 and 2.4 is stable at high temperatures.

The limiting values of the dependence of resistivity on porosity can be qualitatively analyzed by considering two cases of fracture porosity. The first case is when the fracture porosity is very small, and the second case is when fracture porosity is dominant.

In the first case when fracture porosity is very small we substitute zero for the value of porosity in equation 2.4. This indicates that the measured resistivity depends only on the resistivity of the hydrothermal pore fluid. This means that when fracture porosity is very small, the measured resistivity for rocks is then expected to be very high. When fracture porosity is very high (totally fractured and saturated rock), the measured resistivity is both a function of fluid resistivity and the b factor. The b factor is temperature dependent and relates average fracture density over large (km^3) volumes of rock to the interface conductivity and fracture porosity (Flovenz et al., 1985).

By considering the anticipated reservoir temperatures of more than 240°C, equations 2.1 and 2.4 can be rearranged as shown below to solve for porosity using a basis function. The basis function finds a point with a value near zero as the solution for the resistivity equation to solve for the fracture porosity of the rocks given the range of the resistivity of the formation, the resistivity of the hydrothermal fluid at 240°C, very low percentage of clay, and fully saturated rocks. For equation 2.4, the **b** factor and the resistivity of the hydrothermal fluid is determined from the equation $b = 2685.3T^{-1.6676}$. The basis porosity function for equation 2.1 and 2.2 are expressed as shown below:

$$f(\Phi) = \frac{(1-\Phi)(1-P_c)}{\rho_b} + \frac{Pc(1-\Phi)}{\rho_c} + \frac{\Phi S_w}{\rho_w} + \frac{\Phi(1-S_w)}{\rho_a} - \frac{1}{\rho} \qquad 2.7$$

$$f(\Phi) = -\frac{1}{\rho} + \frac{0.22}{\rho_w}\left[1-(1-\Phi_f)^{2/3} + \frac{(1-\Phi_f)^{2/3}}{1+(1-\Phi_f)^{1/3}+(1-\Phi_f)^{1/3}4.9x10^{-3}}\right] + \frac{\Phi_f{}^{1.06}}{b} \qquad 2.8$$

The basis function tries to find a zero of the equation with one variable, in this case porosity, with a specified starting interval between 0.0001-0.9. The algorithm uses a combination of bisection, secant, and inverse quadratic interpolation methods to determine porosity. The basis function was evaluated for both equation 2.7 and 2.8. In equation 2.7, a solution was found for about 10 percent clay, matrix resistivity of 5,000 Ωm (which is the estimated value for resistivity of a basaltic rock), resistivity of clay at about 5 Ωm, and water resistivity of 7 Ωm. When the percentage of clay is very high or resistivity of clay is less than 5 Ωm, then the solution gives very high

values of porosity (Figure 7) which imply that a different conduction mechanism is required. The high values obtained for porosity show that the model cannot be explained by fracture porosity in areas dominated either by clays or very low resistivity where ionic conduction is dominant for instance in molten rock. The value of pore fluid resistivity is the average of the values of 5 Ωm determined from the approximation from TDS measurements and that of 10-15 Ωm determined for measured resistivity of fresh-water hydrothermal systems (Arnasson et al., 2000).

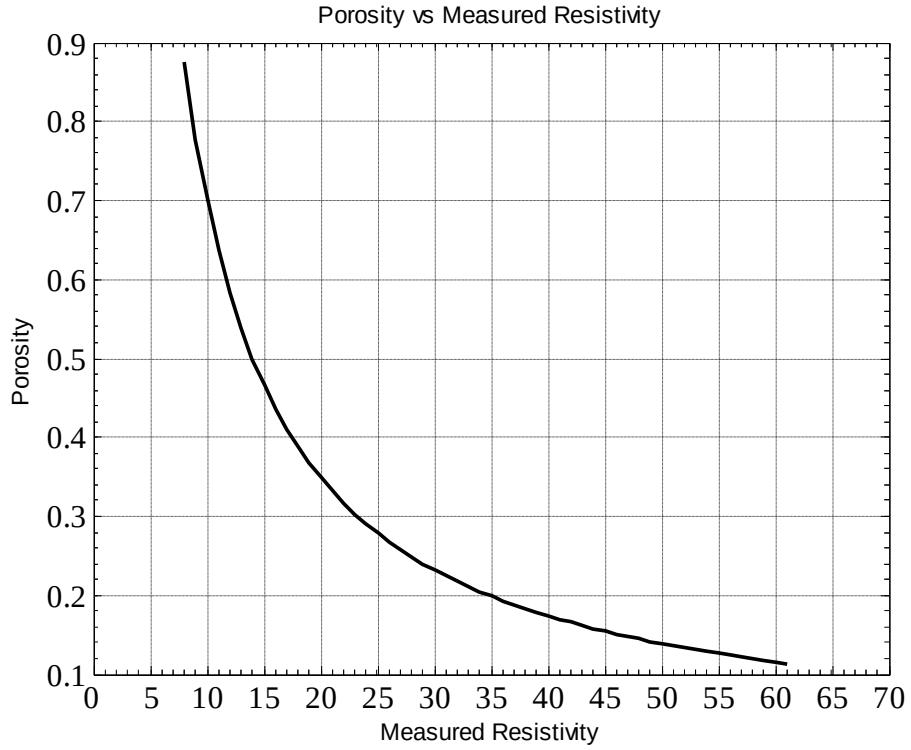

Figure 7: Plot of the variation in porosity against measured resistivity using equation 2.7 for pore water resistivity of 7 Ωm, matrix resistivity of 5,000 Ωm and clay resistivity of 5 Ωm. The plot shows that fracture porosity is very low for measured resistivity higher than 70 Ωm. Based on this model, highest fracture porosity (≥0.3) is found within the resistivity range 5-25 Ωm.

Analysis of the results from equations 2.7 and 2.8 indicates that equation 2.9, which takes into account the effect of temperature, underestimates the porosity determined from some cores in the hydrothermal field. From the analysis of the resistivity and porosity from equation 2.10, the value of fracture porosity obtained is less than 10% (Figure 8) and is not consistent with porosity data from the hydrothermal systems.

From this analysis, there is a very narrow range (5-130 Ωm) of resistivity that correlates with high fracture porosity of more than 5%. The fracture porosity is very

low for resistivity more than 130 Ωm. Based on this analysis; it has been assumed that the areas with high resistivity at a depth of more than 1000m have low fracture porosity and possibly low reservoir temperatures. These limits for resistivity are used in the objective function to formulate the relationship between resistivity and P-wave velocity based on the porosity distribution derived from resistivity.

When the exponent of fracture porosity is modified from 1.06 to a value greater than 2 in equation 2.10, the solution gives consistent results with the measured effective porosity of between 0% and 50% with porosity as high as 49% measured in the igneous samples with the majority falling below 20% (Sigurdsson et al., 2000). The modified basis function used in this dissertation is shown in equation 2.23 which is used to formulate the relationship between P-wave velocity and resistivity, taking into account the effects of pore fluid resistivity, reservoir temperature, and the percentage of low-temperature clays which is very small for high temperature hydrothermal systems.

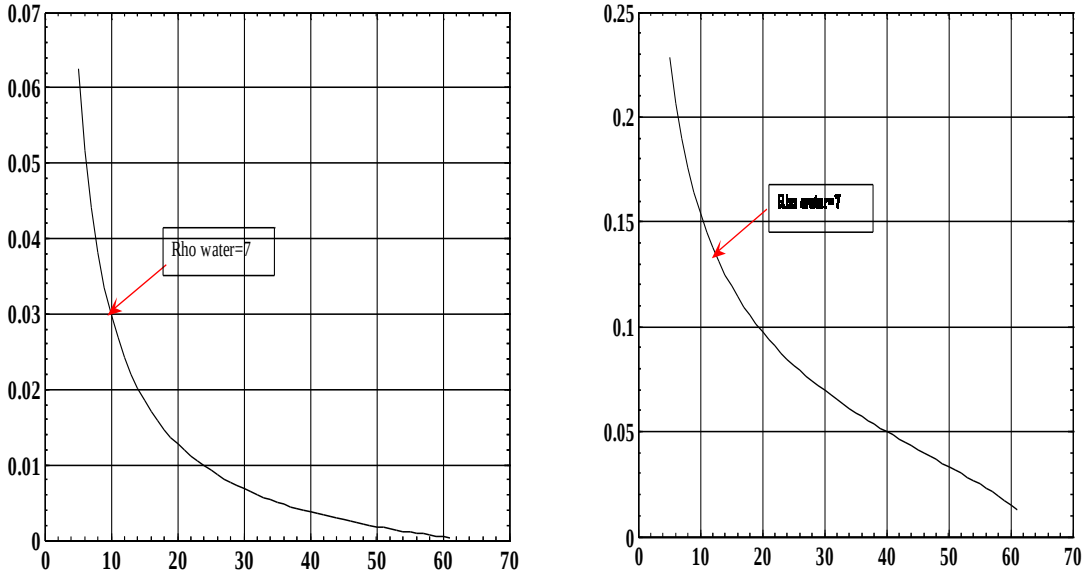

Figure 8: Plots of fracture porosity determined from equation 2.8 shown on the left and fracture porosity determined from a modified equation 2.13 with a higher exponent for the fracture porosity shown on the right. Fracture porosity determined from equation 2.12 is very low (<10%).

When the empirically determined values of porosity are compared with those measured in the hydrothermal systems in Iceland and Kenya, the modified double porosity model gives a good estimate. This therefore justifies the use of a higher exponent for equation 2.7 to simulate the measured porosity for various hydrothermal systems located within volcanic areas.

2.2.1.2 Relationship between P-wave velocity, porosity and resistivity

When an earthquake is generated, body waves travel through the rocks. The main interest is in the body waves which generate P-waves and S-waves which are related to the elastic coefficients of the medium they propagate through. The bulk density ρ_b depends on fracture-porosity Φ_f, density of the matrix ρ_m and density of the fluid ρ_f as shown below:

$$\rho_b = \Phi_f \rho_f + (1 - \Phi_f)\rho_m \qquad 2.9$$

From the analysis of field measurements and core samples, Flóvenz' et al. (1985) established a semi-empirical relation based on the double porosity model (Stefansson et al., 1982). An important finding in this study was that for rocks saturated with fluids with resistivity higher than 2 Ωm (at room temperature), the bulk resistivity is independent of fluid but dependent on fracture-porosity and temperature. This finding was used in this study to evaluate the dependence of resistivity and P-wave velocity on fracture porosity with an emphasis on understanding the structural and physical controls for hydrothermal fluid circulation. In hydrothermal systems, the density of the fluid is a function of temperature, salinity and pressure. The P-wave velocity and porosity relationship has been established based on the equation by Wyllie et al., 1958 shown below:

$$\frac{1}{V_p} = \frac{\Phi_t}{V_w} + \frac{1-\Phi_t}{V_r} \qquad 2.10$$

where V_p is the bulk P-wave velocity, V_w is the P-wave velocity in water, V_r is the P-wave velocity of the rock matrix, and Φ_t is the total porosity and it further assumed that in the fracture zone it is dominated by fracture porosity while in the un-fractured zone it is dominated by matrix porosity. Based on a 2-km core from Eastern Iceland, Christensen and Wilkens (1982) concluded that the Wyllie equation was a good approximation of the interpreted P-wave velocity with V_w=1500 ms^{-1} and V_r=6250 ms^{-1}.

From equation 2.10 above, porosity can be expressed as

$$\Phi_f = \frac{(V_r - V_p)V_f}{(V_r - V_f)V_p} \qquad 2.11$$

In the vicinity of the fractured zones, V_r can be considered as the velocity of the un-fractured rock and V_p as the measured velocity; V_f is the velocity of the fluid. This

relation shows that the P-wave velocity is related to porosity. The limiting factors are the velocity of the un-fractured rock, which is assumed to be related to high resistivity, the measured velocity model and the pore fluid velocity (in this case water).

This relationship together with the Wyllie equation was used to establish the empirical relationship between porosity and P-wave velocity as shown below:

$$\Phi_f = 1974 ms^{-1} V_p^{-1} - 0.32 \qquad 2.12$$

From this equation, it can be deduced that as porosity increases, the velocity of the matrix reduces. The P-wave velocity of the rock matrix is therefore expected to reduce in the fault zone within a hydrothermal system at the scale of the convecting system. The cooler surrounding areas with low fracture porosity and a lower rank of hydrothermal alteration are expected to have high P-wave velocity.

If the location of the earthquake is known, then we can consider the direction of fast $S_f(t)$ and slow shear $S_s(t)$ waves. The ratio of $S_f(t)$ and $S_s(t)$ can be related to the anisotropy. In cracked reservoirs, this anisotropy is usually caused by aligned systems of open, fluid-filled micro-fractures. The deployment of seismic arrays were designed to gather SWS data with uniform Azimuthal coverage, ideal for performing high-resolution tomographic inversion for 3-D fracture density.

Based on the assumption that both P-wave velocity and resistivity are affected by fracture porosity, and then if fracture porosity and the resistivity of the fluid are known, then P-wave velocity can be calculated. In this study, the range of porosity and resistivity values obtained from modeling the MT data have been used to estimate the velocity model which is then used to locate the microearthquakes. From the analysis of the relationship between resistivity and porosity, this study assumes that in areas with resistivity high than 130 Ωm the fracture porosity is very low, and therefore the P-wave velocity approaches that of the rock matrix. It is therefore expected that the variation in porosity is significant only in areas with low resistivity close to the fracture zone. The modified equation 2.8 that conforms to the observed porosity can be expressed as shown below:

$$f(\Phi) = -\frac{1}{\rho} + \frac{0.22}{\rho_w}\left[1 - (1-\Phi_f)^{2/3} + \frac{(1-\Phi_f)^{2/3}}{1 + (1-\Phi_f)^{1/3} + (1-\Phi_f)^{1/3} 4.9x10^{-3}}\right] + \frac{\Phi_f{}^2}{b} \qquad 2.13$$

This equation can be used together with 2.12 to obtain the relationship between measured resistivity and P-wave velocity. From the solution of fracture porosity and measured resistivity, it is assumed that for areas of resistivity higher than 130

Ωm, the P-wave velocity will be equal to that of the rock matrix (V_r =6250 ms^{-1}) in the unfractured zone. If measurements of the matrix P-wave velocity are known, the value can be substituted in this equation. The solutions for the resistivity and porosity was obtained and then used to determine P-wave velocity. As an example, when the measured resistivity is about 10 Ωm, the porosity is 15±5% and equation 2.21 can be expressed as

$$0.15 = 1974 ms^{-1} V_p^{-1} - 0.32 \qquad 2.14$$

$$V_p = \frac{1974 ms^{-1}}{0.47} = \mathbf{4200 \pm 200 ms^{-1}} \qquad 2.15$$

This value is consistent with expected acoustic P-wave velocity of 4000-4600 m/s for basaltic samples with grain densities higher than 3000 kg/m^3 (Sigurdsson et al., 2000).

2.2.2 Relationship between MT anisotropy and polarization and shear wave splitting and polarization

Resistivity anisotropy in rocks can be caused by either orientation of elongated rock grains or by fine layering with different resistivity values. Anisotropy in hydrothermal systems can either result from directional fracturing and orientation of pore spaces or the influence of pressure gradients, fluid content, and degree of hydrothermal alteration.

A major problem in analyzing and interpreting shear wave anisotropy recorded by surface measurements is determining the depth of the anisotropy (Crampin and Peacock, 2004). In this dissertation, it is assumed that the splitting in the MT data is caused by resistivity variations at depth rather than lateral variations. This is based on the regional resistivity model that shows that resistivity increases from the volcanic zone towards the older Tertiary rocks (Björnsson et al., 2005). It is postulated that the splitting in the MT data is caused by variations in resistivity below the clay cap. The depth at which the splitting in the MT data occurs is used to model the depth to the anisotropy layer for S-wave splitting data.

2.2.2.1 Polarization and anisotropy in MT data

The motivation to analyze the polarization and anisotropy in the MT data and compare it to S-wave splitting is based the goal of understanding the orientation and anisotropy/heterogeneity caused by the postulated fluid-filled fracture zones.

Based on this assumption, the current distribution depends on the orientation and fracture density within the fluid-filled fracture zone. The study of the MT polarization and anisotropy therefore has the potential of providing important structural information that can be used to map high permeability zones in the hydrothermal systems.

The MT measurements are made in the time domain by sampling the variations in the EM fields at specified frequency windows (determined by equipment type and manufacturer). A Fourier Transform is usually applied to the time domain electromagnetic variations E (t) and H (t) to determine their amplitudes as a function of angular frequency. The EM equations are of the form $\nabla^2 X + k^2 X = 0$ where X is either the magnetic (H) or electric field (E). These are the wave equations in the frequency domain (commonly known as Helmholtz equations in E and H) which have a similar form to the seismic wave propagation.

The Helmholtz equations in MT reduce to diffusion equations for E and H fields in the earth while microearthquake data is governed by the wave equation. This difference in propagation may seem to be a problem in comparing MT and seismic data. However, because of very high air-earth resistivity contrast, the vertical E-field can be ignored at the earth's surface for almost any resistivity distribution in the earth (but not for sub-surface MT). Horizontal H varies slowly and so need not be measured except near vertical discontinuities in resistivity that produces vertical current. The vertical H is not coupled to E so is not needed to derive resistivity but it is still useful as an inductive indication of dimension. The assumption based on the conceptual model is that seismic waves travel to the earth's surface at they are affected by the same rock properties as the diffusive MT propagation.

This study focused mainly on finding the 2-D conductivity distribution that might be an indicator of zones with a high density of fluid-filled fractures that are postulated to cause polarization and anisotropy in the MT data. This formulation is used together with shear wave splitting and polarization to model fracture porosity.

For a 2-D subsurface, the EM fields are polarized into two modes referred to as TE-mode when the E fields are parallel to the direction of strike and TM-mode when the H-field is parallel to the strike direction. When the MT polarization is in the direction of the regional strike, it is assumed that there will be no conductivity variation in this direction and the resistivity varies only with depth and the perpendicular (dip) axis. In this case the EM fields decouple into 2 distinct polarizations, the TE (transverse electric) and TM (transverse magnetic).

During data acquisition, the EM measurements are sometimes made in the NS and EW directions which do not always correspond to the direction of strike. To facilitate 2D MT analysis approaches like 2D inversions, are commonly used.

In the case of 2-D, the direction of the induction arrow is perpendicular to the orientation of the regional strike. In this dissertation, will compare and contrast the polarization in both MT and shear wave splitting in relation to the postulated fluid filled fractures. For a rock mass with higher conductivity that is embedded in a host rock with lower conductivity, the induction arrows point towards the conductor, and the normal to the conductor at any given measurement point defines the polarization direction. If the high conductive rock mass is oriented parallel to the fluid-fractures, and assuming further that the relationship between resistivity and fracture porosity holds, then the resistivity will be lower in the direction parallel to the fractures and higher in the direction perpendicular to the structures (Figure 9).

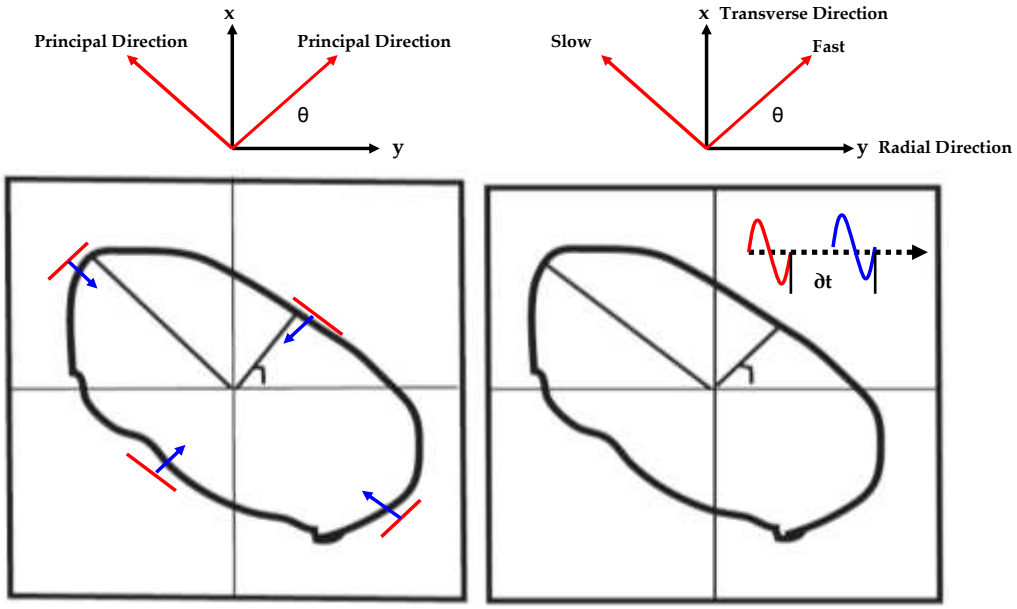

Figure 9: Postulated polarization of the MT and shear wave splitting data due to a conductive fluid-filled body embedded in a resistive host rock. The MT data is polarized into two principal directions while s-wave decouples into fast and slow directions. The direction of MT polarization is parallel to the conductive body while the induction arrows (shown with a blue arrow) point towards the conductor. The time delay between the slow and fast shear waves is proportional to the velocity contrasts.

This relationship has been expressed in different ways by many authors including Heise and Pous (2001); Eisel and Haak (1999). By considering the bulk resistivity

normal (ρ_n) and parallel (ρ_p) to the fractures, the analogous formulation for resistors in parallel and in series can be obtained as:

$$\rho_n = (1-V_1)\rho_2 + V_1\rho_1 \text{ and} \quad 2.16$$

$$\rho_p = \frac{\rho_2\rho_1}{(1-V_1)\rho_1 + V_1\rho_2} \quad 2.17$$

In this case ρ_1 and V_1 are resistivity and the volume fraction occupied by the conductive fluid-filled body, while ρ_2 is the resistivity of the host rock. For the 2-D case considered in this dissertation, the volume fraction is considered to be proportional to the width of the resistivity of the low and high resistivity zones defined by Figure 9 above. The low resistivity zone can also be made or alternating vertical columns of high and low resistivity that can result in the splitting MT data.

The parameter γ_R, which is the normalized difference between the resistivity normal to and parallel to the fluid-filled fractures, can be defined as shown below:

$$\gamma_R = \frac{\rho_n - \rho_p}{\rho_n} \quad 2.18$$

Based on this equation, when ρ_n is equal to ρ_p, then γ is zero. This would result in a situation where the MT graphs have the same resistivity. It is anticipated that the effect of conductive fluids within a fracture zone, would create a significant change in resistivity within the fracture zone and very little change in the host rock surrounding the hydrothermal system. It is therefore postulated that a relationship exists between S-wave splitting and MT splitting anisotropy.

2.2.2.2 Shear wave splitting and polarization

Shear wave splitting, which is sometimes referred to seismic birefringence, is probably the most diagnostic and measurable property of seismic anisotropy (Crampin 1985). The anisotropy is usually interpreted as a characteristic of fluid-saturated, stress-aligned cracks or grain-boundary films of liquid melt (Crampin, 1994, 1996, 2005). It has also been observed in several studies that shear-wave splitting shows temporal and spatial variation in response to small changes in stress (Crampin and Peacock, 2005). Crampin and Peacock (2005) have noted that there is a problem in analyzing and interpreting the observed anisotropy from measurements recorded by instruments on the surface because the depth of the anisotropy is not usually known. In this study, the similarity between the MT polarization (in the frequency range 10-0.01 Hz) and S-wave splitting is used to

determine the depth of the anisotropy. The most important parameters in evaluating S-wave splitting are the polarization angle (PA) of the fast S-wave arrival and the time difference (δt)between the fast and slow waves. Both the PA and δt are related to the orientations of the cracks and crack density.

The pores, cracks, fractures, fissures, joints, faults, and the internal rock structures are important in controlling the storage and transmission of fluids in rocks. Several theoretical formulations to study seismic propagation in porous or fractured medium have been formulated over the years (Hudson, 1980; O'Connell and Budiansky, 1974), but their field applications have been limited. The S-wave is polarized into a fast wave parallel to the direction of maximum stress and slow wave which propagates perpendicular to the fractures. For both MT and S-wave splitting, we postulate that they would have the strike direction. The shear waves after rotation to fast $S_f(t)$ and slow $S_s(t)$ polarizations with time delay ∂t between them.

For vertically aligned fluid filled fractures, the basic theory of seismic wave propagation is based on the equations of motion. The resulting wave propagates through the medium without movement of material. The wave motion is usually described using the theory of linear elasticity.

The crack density in a given volume of rock is proportional to the cube of the crack radius (Hudson, 1980. Crampin, 1994) as shown below:

$$\varepsilon = \nu a^3 \qquad 2.19$$

where $\nu = \frac{N}{V}$ and N is the number of cracks with radius a (length $2a$) for a given volume of rock V.

The anisotropy is defined by Hudson (1981) as

$$\gamma_s = \frac{V_{s1} - V_{s2}}{V_s} \qquad 2.20$$

where V_{s1} the phase velocity in the fast direction is, V_{s2} is the phase velocity in the slow direction, and V_s is the phase velocity of the matrix.

The objective is to use the equation of anisotropy by Hudson (1981); to compare with the anisotropy defined by resistivity measurements in equation 2.18.

In shear wave splitting models, the only data available is arrival times and location of stations. The unknowns are the velocity structure and the location of the earthquakes. It is further assumed that in the fracture zone, the phase velocity is equal to the group velocity. If the polarization parallel to the fractures is assigned as

P_1 and the polarization perpendicular to the fractures as P_2, then the difference in the velocity can be expressed as an approximation for anisotropy as

$$\gamma_s = \left(V_{P1} - V_{P2}\right) \Big/ V_{P1} \qquad 2.21$$

From the field data, only the arrival time for the fast and slow waves is known but the velocities are the unknowns. If the earthquake has been located, then the ray path can be defined by the distance **L** or the summation of the product of the time and velocities in the individual layers below the measurement point. For constant velocity, the ray path is the distance (**L**) between the earthquake and the measuring point and the travel times t_1 for the fast shear wave and t_2 for the slow shear wave such that

$$V_{p1} = \frac{L}{t_1},\ V_{p2} = \frac{L}{t_2} \quad \text{and} \qquad 2.22$$

$$\gamma_s = \frac{\left[\left(L/t_1\right) - \left(L/t_2\right)\right]}{L/t_1} = \frac{t_2 - t_1}{t_1} = \frac{V_s \delta t}{L} = \frac{V_p \delta t}{\alpha L} \qquad 2.23$$

where $V_s = V_p/\alpha$ is the S-wave velocity, L is the depth to the origin of the S-wave splitting, α is V_p/V_s ratio and δt is the time difference between the arrival times for the fast and slow shear waves.

The shear wave velocity is determined from the following:

1. V_p/V_s ratios and the existing p-wave velocity models; and
2. S-wave velocity based on the arrival times of some well located earthquakes.

From this analysis, the relationship between the S-wave anisotropy (γ_s) and the resistivity anisotropy (γ_R) was evaluated.

2.3 Microearthquake location

Locating earthquakes requires the identification of seismic phases and the knowledge of the velocity model. Solving the forward problem is easy if the velocity structure and the travel time of the P and S waves are known. However, the velocity structure and the origin time at the hypocenter are not usually known. For a simple homogenous case, the travel time for the P and S waves can be calculated from the distance from the source to the receiver (Figure 10).

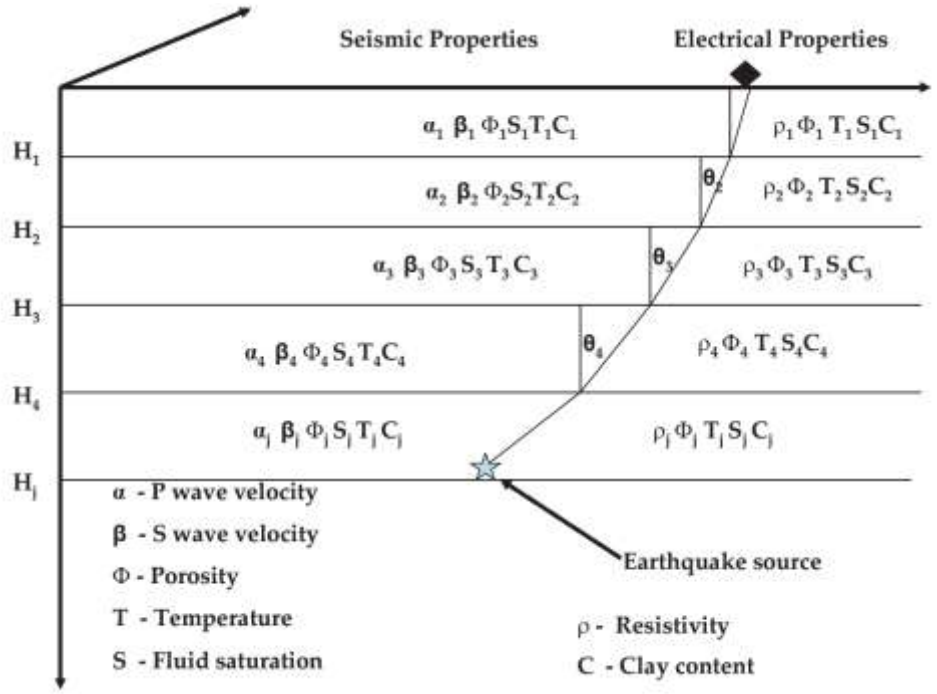

Figure 10: Propagation of up-going seismic waves in a 1-D media. The ray path is a summation of the distance traveled in each layer. The velocity of the seismic waves depends on the density which depends on porosity. The change in porosity causes the ray to bend.

Based on the conceptual model, it is postulated that if the earthquakes occur above the heat source, the ray paths are composed of both down-going and up-going P- and S-waves. If this condition exists, then it is expected that the recorded signal would show the first arrival P-wave, reflected P-wave and converted S-wave.

In modeling, it is common to assign a velocity model, and then locate the events. After locating many events, it is then the standard practice to use the locations to improve on the velocity model. A list of the locations of microearthquake stations is required by the program to locate earthquakes. The locations were determined from the internal GPS measurements and cross-checked with locations from the hand held GPS. The microearthquakes are located at a reference datum which is the average of the stations. Station corrections are incorporated to account for the elevation differences with respect to average elevation. The station corrections are computed by locating many earthquakes with zero corrections and then assigning the average time errors as station correction.

For any station, the arrival time is formulated in terms of the unknown parameters for the earthquake and the known parameters for the station location. The forward problem for the arrival time is related to model parameters, the unknown

earthquake location, the origin time, velocity, and the known station location parameters.

The location of events is carried out first by picking only one P- and S-wave arrivals using the Hypoinverse-2000 code (Klein, 2000) with a parameter input interface in Mat lab. The initial velocity model was obtained from the results of seismic studies at Krafla by Brandsdottir et al. (1995). The final velocity model was obtained from resistivity.

2.4 Joint inversion approach

The goal of the joint inversion of the geophysical data is to give better resolution of the structure of the fault zones in the hydrothermal systems. The initial steps involve the uses of some existing interpretation techniques to prepare a basis for a structural approach to determine fracture porosity distribution in the vicinity of fracture zones and the heat source. This inversion approach is based on the assumption that both electromagnetic and seismic data are affected by the geological structure and the rock properties in the area of collocated data sets.

The initial joint interpretation resistivity and microearthquake data to determine fracture porosity has already been discussed. The next step is to briefly discuss the theoretical outline of joint interpretation of Transient Electromagnetic (TEM) and magnetotelluric (MT) data to determine galvanic effects. After removal of galvanic effects, 2-D forward and inverse modeling of the MT data are carried out and then jointly interpreted with microearthquake locations. The final approach for 2-D interpretation uses joint inversion through a structural approach. The 2-D resistivity model is used to generate a porosity operator that converts the resistivity porosity. The porosity operator is also used to generate a P-wave and porosity relationship.

2.4.1 1-D TEM and MT formulation

2.4.1.1 1-D TEM formulation

In the TEM method, a time varying magnetic field is generated by a controlled artificial source. In this method, a loop of wire is placed on the ground and a constant current transmitted through it. The current is turned on and off at predetermined turnoff times. When the current is turned off, it creates a decaying magnetic field, which induces an electric current in the earth. This electric current distribution induces a secondary magnetic field that decays with time, and the rate of decay is measured at the centre of the loop by an induction coil.

The Occam one-dimensional inversion of electromagnetic data generally refers the data interpretation with many layers with fixed thicknesses and variable resistivities. The resistivity values vary with little contrast between layers. The initial model can either be automatically generated with constant initial resistivities or by specifying an initial model file and the resistivities of the layers. The Occam inversion therefore seeks the "smoothest" model that fits the data (Constable et al., 1987).

2.4.1.2 1-D MT formulation

The apparent resistivity is obtained from the scaled ratio of the impedance tensor (**Z**) which is defined by $\left(\sqrt{E/H}\right)$. The apparent resistivity (ρ_a) and phase of impedance (Φ_z) are given by

$$\rho_{aij} = \sqrt{\frac{1}{\omega\mu}}\left|Z_{ij}\right|^2, \text{ and} \qquad 2.24$$

$$\Phi_{zij} = \tan^{-1}\frac{\mathbf{Im}(Z_{ij})}{\mathbf{Re}(Z_{ij})}, \text{ where } ij = xy, yx \qquad 2.25$$

The 1-D formulation is carried by the Occam method which is similar to that already discussed for the TEM method.

2.4.2 2-D forward and inverse MT formulation

2-D forward and inverse modeling was carried out on the MT data sets to determine which features in the inversion models were important. Since the WinGlink program was used in the interpretation of 2-D MT data, the detailed discussion on the forward and inverse modeling can be found in Rodi and Mackie, 2001.

The forward model is computed using finite difference equations generated by network analogs to Maxwell's equations. The 2-D mesh is user defined and it incorporates topography. The forward response is saved as station data.

The inversion routine finds regularized (smooth) solutions assuming a 2-D resistivity distribution using the Nonlinear Conjugate Gradients (NLCG) method to match the MT data. The NLCG method is used to minimize an objective function that is the summation of the normalized data misfits and the smoothness of the model. The tradeoff between data misfits and model smoothness is controlled by a regularized user defined parameter (tau), which penalizes data residuals and spatial second order resistivity (Rodi and Mackie, 2001).

2.4.3 Structural approach of joint inversion of resistivity and microearthquake data

The background to joint interpretation of geophysical data acquired by different methods is based on the assumption that the observed resistivity and seismic anomalies are caused by the same physical parameters (Kozlovskaya E., 2001). The main assumption in this study is that both resistivity and velocity of rocks in hydrothermal systems are affected by the same physical properties which are affected by fractures and faults. The changes in the physical properties structural and geological boundaries cause variations in the measured velocity and resistivity.

The development of the joint inversion of microearthquake and resistivity data is based on assumed relationship of fracture porosity. In this formulation, the inversion is solved through a defined objective function, which takes into account the factors that relate both resistivity and P-wave velocity to porosity in the vicinity of a fracture zone in a hydrothermal system.

If is assumed that fracture porosity, determined from resistivity and seismic waves can be related through an operator similar to that defined by Haber and Oldenburg (1997) such that

$$\Im_R[m_R] = d_R \quad \text{and} \quad \Im_S[m_S] = d_S \qquad 2.26$$

where the subscripts R and S refer to resistivity and seismic waves, $\Im$ is the operator representing measurements, m represents the model parameters and d represents data. For 2-D, the model parameters are expressed as grids with different porosities. The assumption is that the porosity is constant in each grid. The data for joint inversion are MT resistivity and P-wave velocity for MEQ. The data sets are related through the porosity operator. The goal is to carry out a joint inversion of the data to recover the model. A fracture porosity operator which relates resistivity, porosity, and P-wave velocity (Figure 11 and 12) close to the fracture zone is defined such that

$$f(\Phi_f) = \begin{Bmatrix} 0 & \rho \geq 130\Omega m & V_P \geq 6000 ms^{-1} \\ 0.5-0 & 5 \geq \rho \leq 130\Omega m & 2500 \geq V_P \leq 6000 ms^{-1} \\ 1-0.5 & 0 \geq \rho \leq 5\Omega m & V_P \leq 2500 ms^{-1} \end{Bmatrix} \qquad 2.27$$

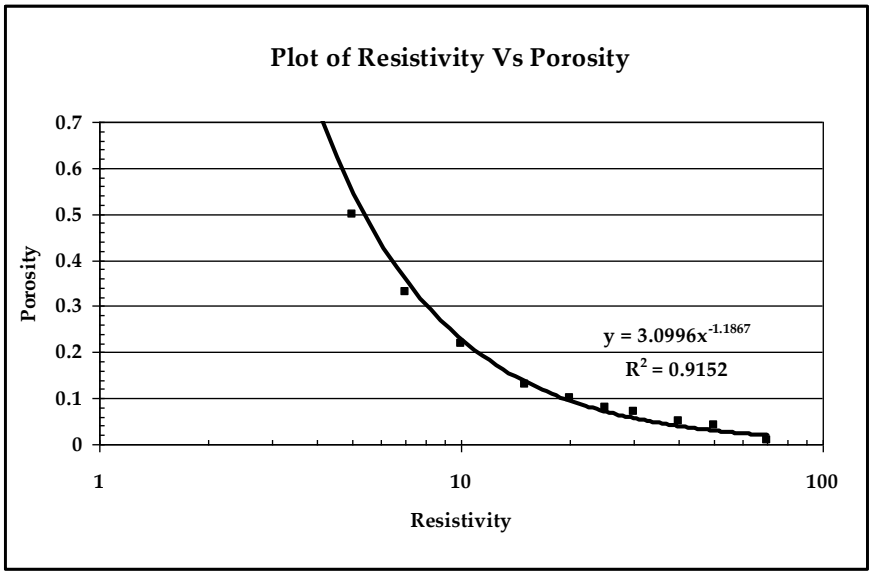

Figure 11: Plot of resistivity against porosity derived from solving a basis function for a double porosity model relating porosity to resistivity close to the fracture zone. The resistivity range is between 1 and 100 Ωm.

The relationship between porosity (Φ_f) and resistivity (ρ) is shown below:

$$\Phi_f = 3.0996\rho^{-1.1867} \qquad 2.28$$

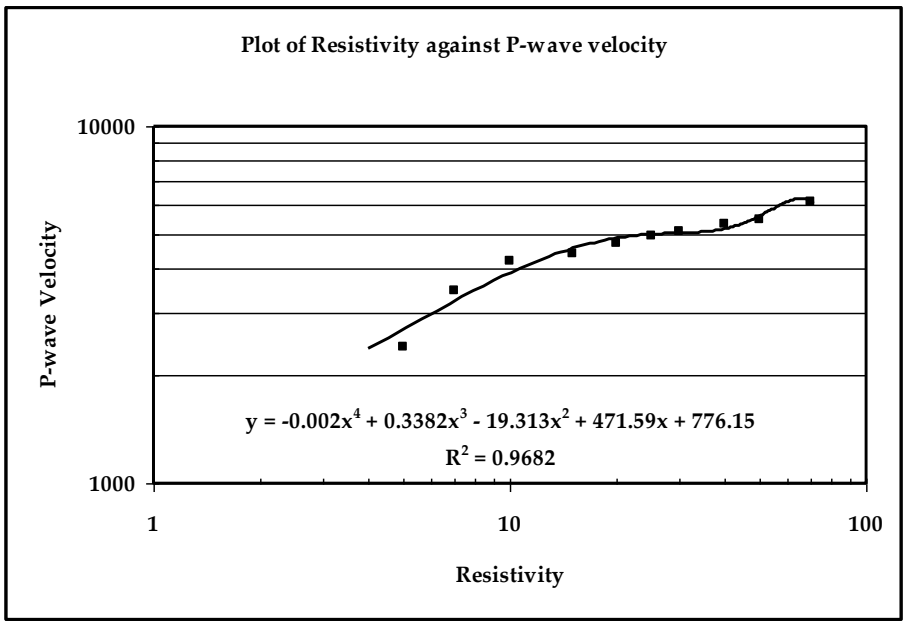

Figure 12: Plot of resistivity against P-wave velocity generated from the porosity derived from resistivity close to the fracture zone using equation 2.13.

Based on our analysis, it is further assumed that in areas of high resistivity on either side of the fracture zone, the P-wave velocity approaches that of the rock matrix velocity. The low

resistivity at a depth of more than 3 km is interpreted as the heat source, and in this dissertation it is anticipated that P- and S-wave reflections of the down going waves.

The initial porosity model parameters are estimated by solving the basis function for the relationship between resistivity and porosity by using the limits defined in equation 2.27 above and equation 2.13 to generate the P-wave velocity. The relationship between P-wave velocity and resistivity is given by

$$V = -0.002\rho^4 + 0.3382\rho^3 - 19.313\rho^2 + 471.59\rho + 776.15 \qquad 2.29$$

The relationship between porosity and P-wave velocity (Figure 12) taking into account the approximation in equation 2.23 is given as

$$\Phi_f = -6x10^{-15}V^4 + 1x10^{-10}V^3 - 8x10^{-7}V^2 + 0.0021V - 1.3238 \qquad 2.30$$

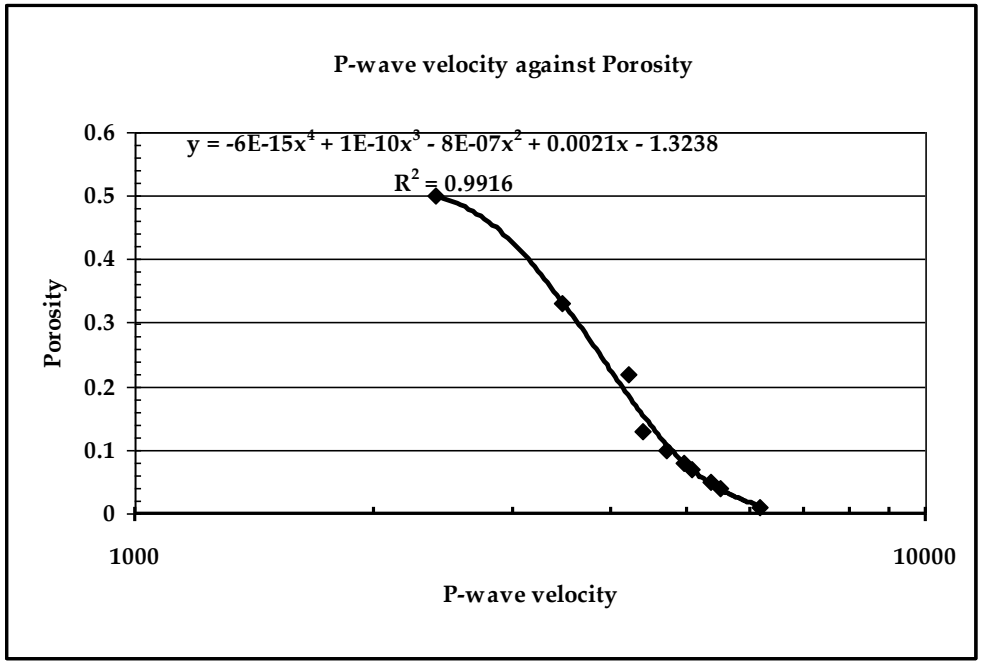

Figure 13: Plot of P-wave velocity against porosity derived from the resistivity.

3.0 Data Acquisition, Processing and Analysis

3.1 Magnetotelluric data acquisition and processing

The Krafla data was acquired during two field campaigns in the summers of 2004 and 2005. Acquisition of high quality magnetotelluric (MT) and microearthquake (MEQ) data at the Krafla geothermal field was completed in September 2005 and complemented the data set acquired in 2004. These data have been used in the Joint Geophysical Imaging study of the hydrothermal systems to understand the fluid movement in the hydrothermal system.

The MT data acquisition was carried out at predetermined sites to complement the existing data; the final location depended on the conditions at the site. The magnetic coils and potential electrodes were oriented in the orthogonal NS and EW directions. The electric field was measured using lead chloride porous pots. The magnetic sensors were buried 30 cm below the surface to minimize wind effects. Many of the sites were covered by young volcanic rocks. The acquisition of high quality data within such areas has demonstrated the use of MT on highly resistive rocks. Some sites straddled known fractures in order to study the effect of open fractures on the MT data. The ground conductivity was improved by placing the electrodes in a salt water and clay mixture.

The ground contact resistance was generally between 1,000 and 6,000 Ohms. The background spontaneous potential (SP) was generally high due to electrochemical potentials. Other sources of noise included power lines, wind noise, and thunderstorms. At the Casa Diablo geothermal field, the contact resistivity was high. Coupled with high wind noise in the forested areas, ground movement, and thunderstorms, this had a significant effect on the data quality at low frequencies.

The Phoenix MTU-5A equipment together with MTC-50 coils was used for data acquisition in the frequency range of 400-0.0025 HZ at Krafla hydrothermal area. The telluric lines were typically 50 - 70m. The lines were kept short to minimize the effects of AC from power lines. Tests showed that longer telluric lines did not improve the data quality. The three MT loggers were deployed everyday in different locations and recorded data automatically from 4 pm to 9 am.

The data was automatically acquired over four frequency bands. The highest frequency band was sampled at 2,400 samples per second; the intermediate band was sampled at 150 samples per second while the low frequency band was sampled at 15 samples per second. The fourth and lowest frequency band was sampled

continuously. The high frequency MT band covers the frequency range 317- 0.352 Hz, the intermediate band covers frequency range 0.2929-0.0003 Hz, and the low band covers the frequency range 0.009-0.00001 Hz.

In these surveys data was acquired for 17 hour continuous periods. In the second MT deployment of 2005, some of the data was acquired with the Phoenix AMT system, with a sampling rate of 24,000 samples per second for the highest frequency band, 2,400 for the intermediate band, and 150 for the low frequency band (which corresponds to the fourth band in the MT system). The data parameters for each site were recorded on data sheets and checked every day. Roving remote reference stations were situated in areas on the periphery of the geothermal system away from power line noise, especially within the Casa Diablo and Krafla geothermal fields.

Data from a total of 100 MT and 40 MEQ sites were acquired at the Krafla hydrothermal system during the field campaigns in 2004 and 2005 (Figure 14).

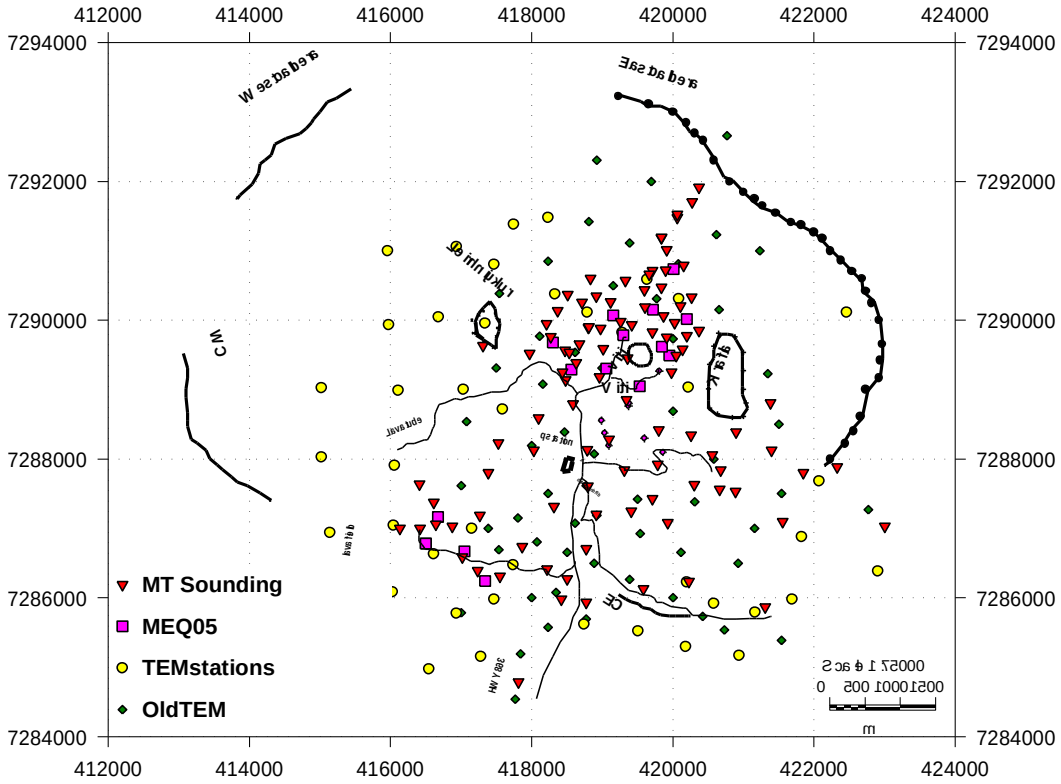

Figure 14: Location of MT soundings, TEM and MEQ stations at Krafla in Iceland. MT stations are shown in red triangles both and include data from both 2004 and 2005 field campaigns, TEM sites for data acquired after 1990 is shown in yellow circles while the data acquired before 1990 is shown in blue squares and MEQ stations in purple squares for 2005 campaign.

3.2 MT Data Processing

When data was downloaded from the flash cards to the computer, the site parameters and acquisition times of the time series were verified. The time series was converted to Fourier transforms, which were then processed into crosspower estimates. The robust processing, a statistical procedure which uses an iterative weighting of residuals to identify and cancel out data that may be biased by non-Gaussian noise was used. The crosspowers were analyzed to obtain impedances, resistivity and phase consistent data. These estimates were then converted to the standard Electronic Data Interchange (EDI) format.

The data was decomposed to the principal axis, a mathematical decomposition commonly used in MT data interpretation to minimize the diagonal elements of the impedance tensor. TEM data was used to correct for static shifts and then to choose the TE and TM polarizations. After the decomposition, 1-D and 2-D inversions were carried out. The data was then used to plot resistivity sections and maps to assist in evaluating the hydrothermal systems.

3.3 MT data quality

The MT data was affected by wind, power lines, seismic noise from movement of trees, thunderstorms, and the high contact resistivity due to recent lava flows close to the surface. Precautions were taken to acquire the best data under the prevailing field conditions. Two measurements close to the Krafla power station could not be used because of the effects of electric fences with DC current. In a few instances, thunderstorms caused saturation on the electric and magnetic signals.

3.4 Microearthquake data acquisition

In the summer of 2004, Duke University deployed 20 new Geospace GS-1 seismometers at Casa Diablo in California, Krafla in NE Iceland, and at Mt. Longonot in Kenya. In the summer of 2005, Duke University deployed 15 more stations to the north and southwest of the Krafla power station. The GS-1 is a 3-component, 24-bit, 4-channel surface seismometer designed for seismic exploration in a variety of terrains. The new seismometers were designed with a natural frequency of 1 Hz, well suited for optimal response to microearthquakes.

The locations of the seismometers were chosen with several features in mind. The first and most important requirement was that the network of stations be evenly distributed around the target areas (Figure 15). Other factors included accessibility and time required to service the stations.

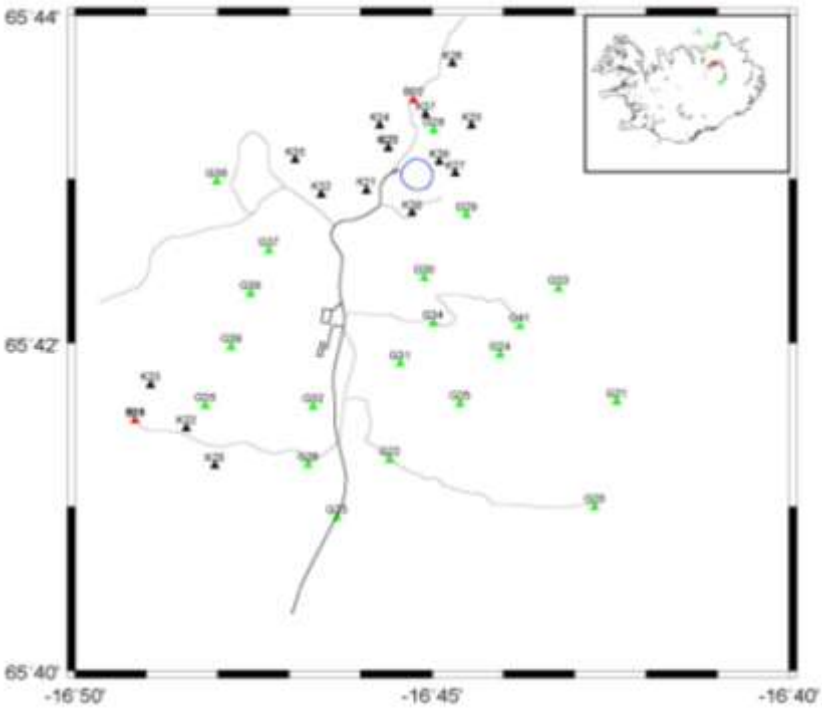

Figure 15: Location of MEQ stations at the Krafla hydrothermal system. MEQ stations from the 2004 campaign are shown in green triangles; the 2005 campaign stations are shown in black triangles. The locations of 2 down-hole seismometers installed after the 2005 field campaign are shown in red triangles.

The 2004 deployment at the Krafla hydrothermal system was designed to monitor earthquake activity in two areas. The first area was in the north and around the existing hydrothermal system, in order to monitor both natural and induced seismicity due to injection of hydrothermal fluids. The seismometers in the southern part of the hydrothermal system recorded very few earthquakes. Thus the 2005 array was deployed to the north and southwest of the existing hydrothermal field.

3.5 Analysis of resistivity data

3.5.1 1-D modeling of transient electromagnetic (TEM) data

The initial 1-D models for the TEM data from Krafla were generated by the TEMTD code written by Arnasson (2004) for a square loop with a receiver at the centre of the loop. The Occam and layered inversions were then performed by the program TEMTD (Arnasson, 2004).

3.5.2 Magnetotelluric (MT) data modeling and interpretation

3.5.2.1 Correction of galvanic distortions in MT data using TEM data

The initial TEM models generated by the program TEMTD (Arnasson, 2004) were input into the WinGlink program. The equivalent MT model of phase and resistivity generated from TEM data was then used to correct for static shifts in the MT data. In most cases the TEM model fit the TE mode of the MT data very well.

Based on the evaluations by Berdichevsky et al., (1998), both the TE and TM modes provide complimentary information on shallow and deep structures. The TE mode is more sensitive to deep structures and more robust to 3-D effects caused by resistive structures. The TM mode is more sensitive to near-surface structures and is affected by the static shift problem more than the TE mode. The characterization used for 1-D and 2-D inversion is that the TE mode is smoother and less distorted by lateral variations and so it is more effective in 1-D inversion. The TM mode is more appropriately matched in 2-D inversion because of the TM mode response to the lateral variations in the plane of the cross-section. Based on this criteria together with the overall pattern of the conductive bodies, TEM data was used to correct for static shifts which are caused by an electric field from boundary charges on near surface inhomogeneities (Pellerin and Hohmann, 1990). The static shifts were carried after static stripping.

The static shift represents a scalar multiplier of the original MT data and, in the case where there is no shift; the multiplier is equal to 1. The use of the TEM method to correct for static shifts is based on the assumption that TEM data are less affected by static shift errors because it does not use electrodes to measure the electric field (Pellerin and Hohmann, 1990). The TEM model at most of the sites fit very well with the TE mode resistivity and phase of the MT data, and as such, the TEM model was used to identify the TE and TM modes of the decoupled MT data. A good example is given by the TEM and MT data fits for sites KMT23 and KMT17 (Figure 16). At site KMT23, the TEM model fits with the more conductive principal resistivity ρ_{xy}, shown by the red spheres, while at site KMT17, the TEM model fits the higher resistivity curve, (ρ_{yx}), where the magnetic field is parallel to the strike direction. This highlights the importance of finding the best method of identifying the decoupled modes of the MT data to obtain a good model of the subsurface. In the TE mode, the electric field is parallel to the strike direction, while in the TM mode the magnetic field is parallel to the strike direction. The use of the TEM data is therefore important in finding consistent polarization directions of the MT data.

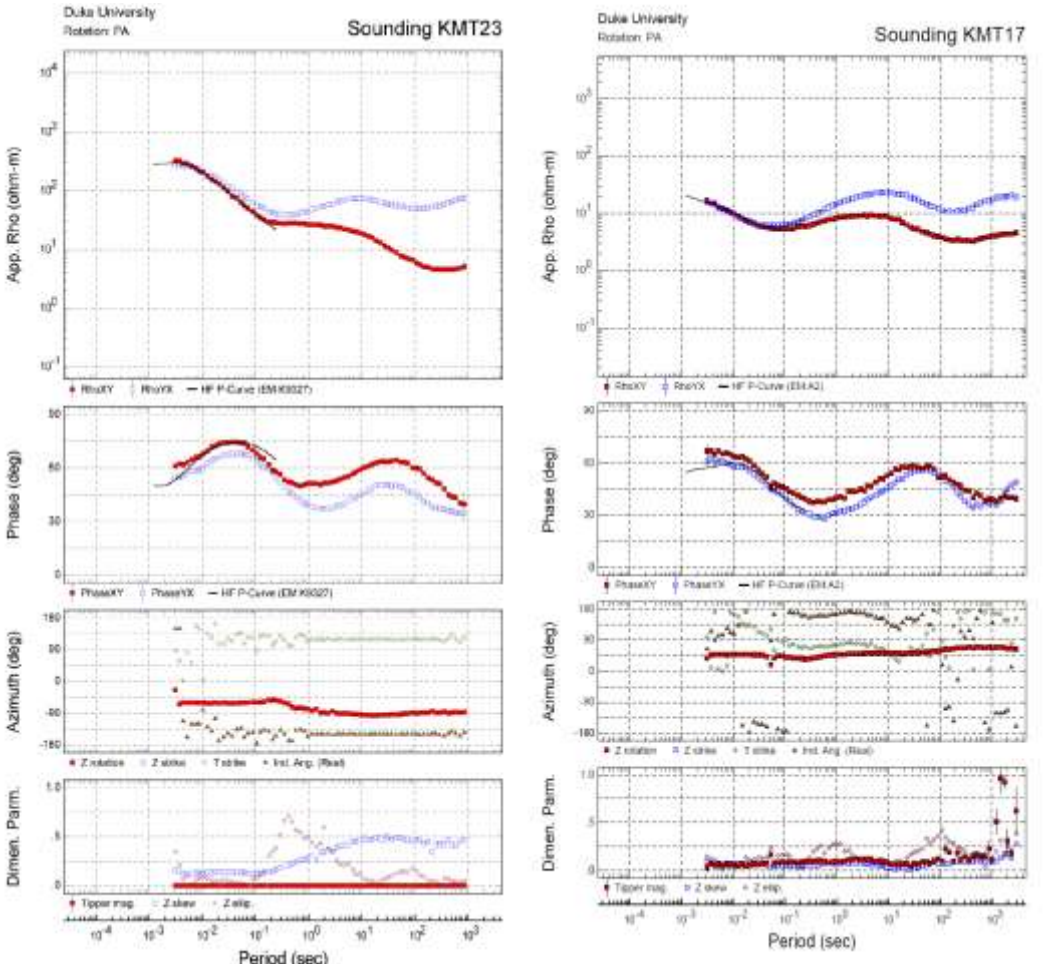

Figure 16: Joint interpretations of TEM and MT data at sites KMT23 and KMT17 in the Krafla geothermal field using the WinGlink program. The apparent resistivity, phase angle, azimuths of polarization and the dimension parameters are plotted against period (longer periods indicate deeper penetration depths). The plots show that 1-D TEM data (green solid line) fits one of the MT resistivity curves and phase. At site KMT23, the TEM model fits the ρ_{xy} while at site KMT17, the TEM model fits ρ_{yx}. The phase angles at both sites vary between 30° and 75° while the skew at short periods are less than 0.2 indicating possible 1-D at shallow depths less than 1500m probed by the TEM method.

The 1-D models generated from TEM data were used to generate equivalent 1-D MT models at the same site. The synthetic 1-D MT models were then used to correct for the static shifts in both TE and TM modes of the MT data.

The MT data was evaluated for static shifts after static stripping to determine the amount of shift before carrying out 1-D and 2-D MT data interpretation. The shifts were determined for the MT data sets collected in 2004 and 2005. The shifts for the TM mode are generally higher than those for the TE mode confirming the interpretation that the TM mode is more affected by near surface lateral resistivity changes. At some sites both the TE and TM modes are affected by static shifts. It is not very clear why this happens, but it can be attributed the spatial variation in the effects of near surface hydrothermal alterations underlain by a consistent subsurface resistivity strike (Pellerin and Hohmann, 1990).

The shifts are highest within the area covered by surface hydrothermal alterations within the geothermal field. The TE mode shift at most of the sites is generally lower than that of the TM mode. The TE mode shift at most sites is less than 3 while the TM mode shift at many sites is more than 20. The shifts in the areas outside the hydrothermal system are generally low for both TE and TM mode indicating near 1-D resistivity distribution even in areas close to fracture zones. For instance, at sounding KMT47 (Figure 17) which was acquired across a visible fracture shows a very small shift. The EW dipole crossed the fracture zone, while the NS dipole ran along the fracture. At high frequencies, the data shows no shift. From this data and the conceptual model, it is inferred that the presence of fractures alone is not a sufficient condition to cause the splitting in the MT data observed at some of the sites. The splitting in the MT data is therefore, likely to be caused by conductivity gradients due to the presence of hydrothermal fluids along fractures.

The shifts have a spatial variation across the area of study but are independent of topography. The shifts are generally low, but at some sites the TM mode shift is quite high (by a factor of more than 2). This seems to confirm that the TM mode is more affected by static shift than is the TE mode. From the plot of elevation and shift, there is some evidence of clustering around the same elevation, indicating that although the shifts are independent of topography, they show spatial variability with MT soundings in the same area having the same shift.

The dimensionality of the data was also analyzed by determining the ellipticity and skew. The ellipticity varies with frequency, and it is high at some sites both at high and low frequencies. As Ranganayaki (1984) pointed out, ellipticity can be affected by 3-D resistivity structures, and even though the TE and TM mode resistivity shows one dimension, the ellipticity can still be high (>0.2). From the example given

below for site KMT 47, ellipticity is high at frequencies between 320 and 90 Hz even though the resistivity looks 1-D.

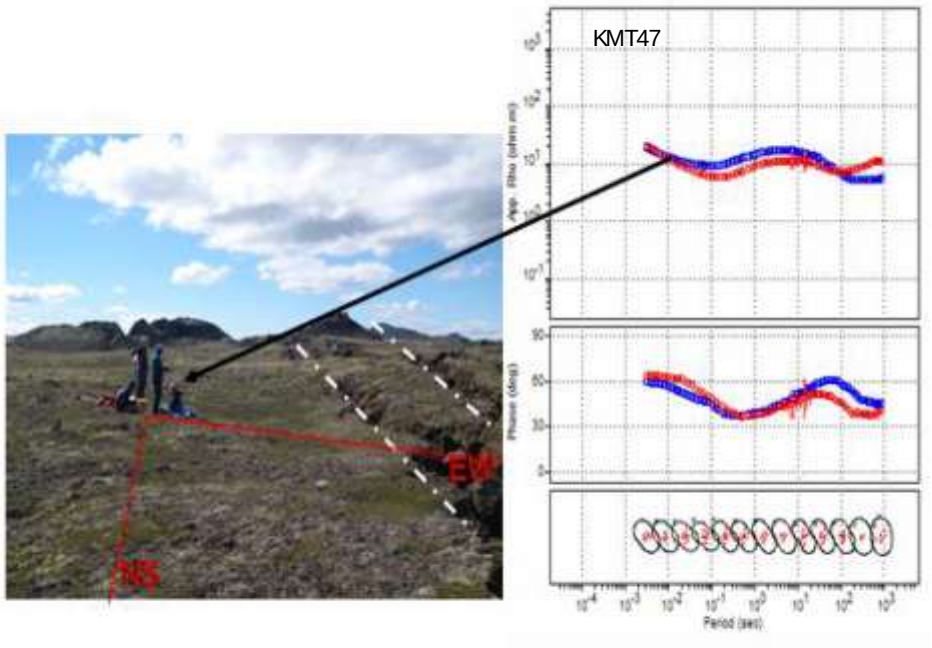

Figure 17: Plot of apparent resistivity, phase and polarization for site KMT 47 located close to NS fracture in the Krafla geothermal field. E-W dipole crosses the fracture (shown by a white dotted lines) while NS dipole runs parallel to the fracture. The upper panel shows the apparent resistivity for the TE mode (blue circles) and the TM mode (red circles). The middle panel shows the phase and the bottom panel shows the polarization direction, which is in the NW-SE direction at almost all frequencies.

In the example for station KMT 47 (Figure 18), the skew is very low (<0.2) even at low frequencies, indicating that the structure is close to either 1-D or 2-D. Based on this analysis, our interpretation is that the near surface layers are 1-D and the splitting in the MT data is caused by contrasts in impedance at depth and not lateral changes on the surface. This interpretation is used together with shear wave splitting to analyze anisotropy.

After initial editing of the MT data, TEM data acquired by the Icelandic Geosurvey (ISOR) at Krafla was used to correct for the static shifts. 1-D models were generated from the collocated data using the 1-D inversion program developed by Arnasson (2004). The 1-D models were then imported into the WinGlink MT data interpretation software and used to correct for static shifts. The use of TEM data assumes similar overlapping depths of penetration for both TEM and MT data (Spies, 1989).

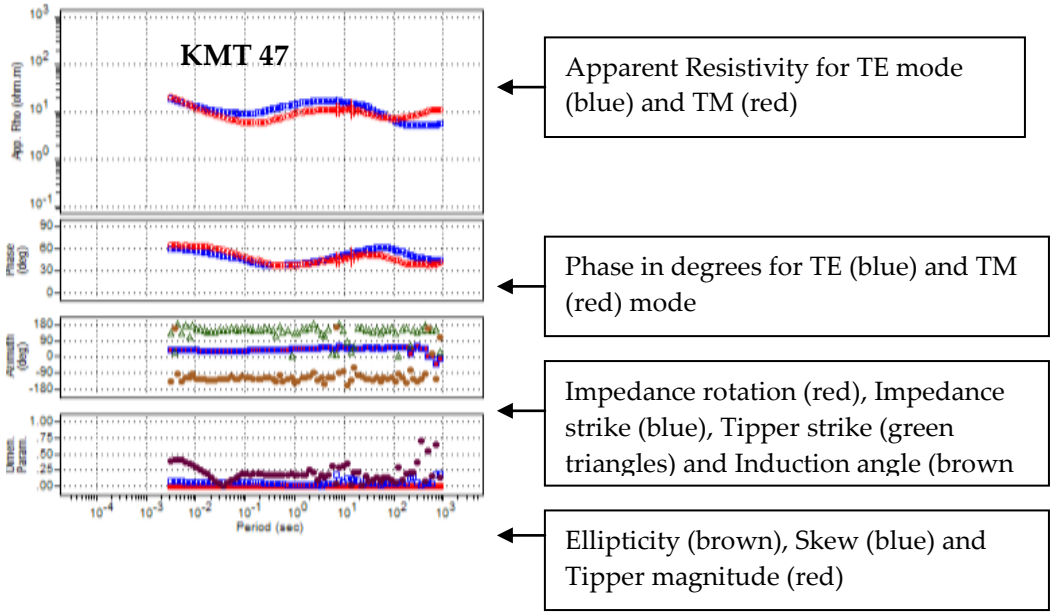

Figure 18: Apparent resistivity, phase, azimuths and dimensional parameters of site KMT 47. The resistivity shows near 1-D structures.

3.5.2.2 1-D models

The 1-D interpretation was carried out both for layered and Occam's inversion using the MT invariant (which is the geometric mean of the TE and TM modes) for the entire MT data set after rotation to the principal axes. The inversion was carried out by specifying an initial model and a root mean square (RMS) of less than 5% for both resistivity and phase of the MT data. Occam's 1-D models consisted of 40 layers of constant thickness on the log scale. Fifty inversions were carried out at every site, and the data were used to construct maps and cross sections to evaluate the spatial variation in resistivity in the study area. An example of 1-D invariant model for (Figure 19) KMT 37 is shown below:

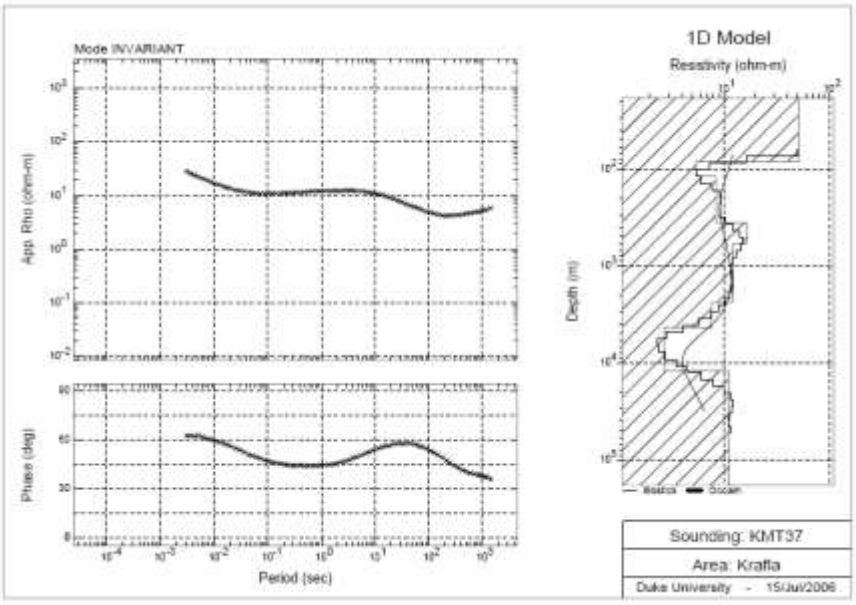

Figure 19: Invariant resistivity model of site KMT 37 indicating a general 5 layer model. The panel on the top left shows the variation of apparent resistivity with period in seconds. The panel on the bottom left shows the changes in phase with period in seconds. The panel on the right shows the variation in resistivity with depth for the 1-D layered and Occam's models.

The models generally show a resistive near-surface layer, a second conductive layer, a third resistive layer, a fourth conductive layer and a resistive half-space. The results of Occam's inversion were used to construct 1-D stitched sections for the invariant resistivity (Figure 20). The vertical contours in the 1-D model should be treated skeptically because MT data resolves conductivity gradients rather than sharp boundaries (Simpson and Bahr, 2005). This means that the resistivities and thickness of the structures are not well resolved.

The models show a narrow zone of low resistivity, which is about 3,000 ±10% m wide at a depth of 3,000 ±10% m. The resistivity, however, increases southwards indicating a boundary of the hydrothermal system. The low resistivity zone is wider at depth and narrower towards the surface, where it connects to a horizontal low resistivity between 0 and 500 mbsl that seems to dip to the SW along the profiles. This layer does not extend to the north of the profile, indicating the possibility of a sharp resistivity boundary.

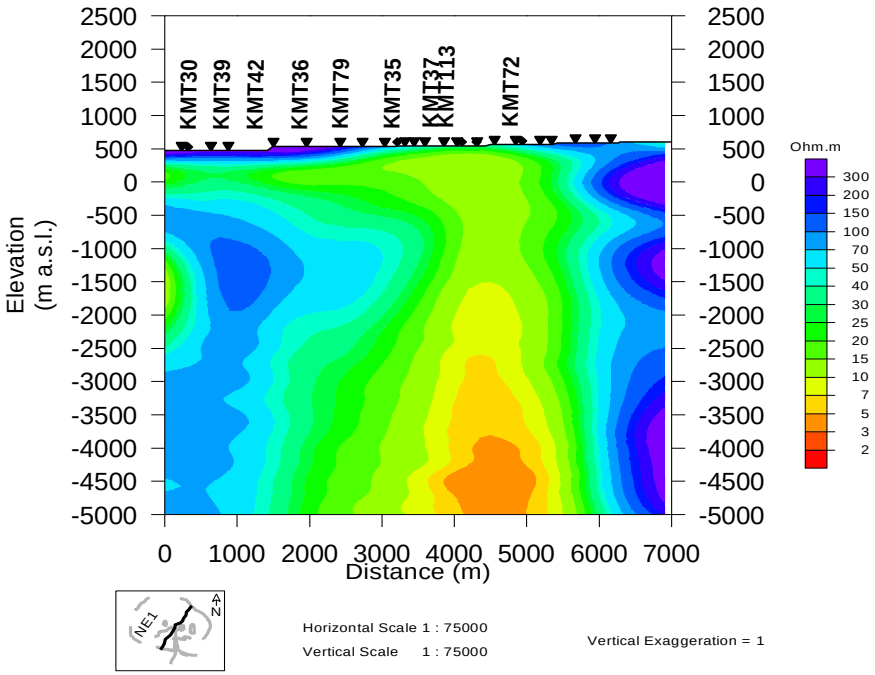

Figure 20: 1-D stitched model from the invariant resistivity data along a NE-SW profile across the Krafla hydrothermal area. The elevation is plotted on the y-axis while the distance from the origin along the profile is plotted on the x-axis. Low resistivity is found in the middle of the profile with high resistivity on both sides of the low resistivity zone. The low resistivity zone occurs between KMT36 and KMT 113 and is centered on site KMT35.

3.5.2.3 1-D resistivity maps

Resistivity maps were prepared from the results of 1-D Occam's models to show the spatial distribution of resistivity at fixed elevations. The maps show that resistivity varies considerably both laterally and with depth. These maps together with the 1-D sections have been used as the basis for the 2-D modeling.

The resistivity map at 200 masl derived from Occam 1-D invariant models (Figure 21) shows that low resistivity occurs to the NE and SW of the area of study. The resistivity boundaries in the northern part are poorly defined because no MT data was acquired in this area. This map probably shows the near surface alteration patterns which seem to correlate with the area of recent volcanic activity. The resistivity distribution shows a linear feature trending in the NW-SE direction across the Krafla hydrothermal system. This feature correlates with the surface alteration and the postulated fracture zone that probably aligns with a shear zone that has been buried by recent volcanic activity. The low resistivity zone is found mainly in the central part of the caldera.

The low resistivity at 1000 mbsl (Figure 22) is found mainly to the north of the study area with a distinct NW-SE trend bound by high resistivity boundaries suggesting structural

control. The low resistivity zone is narrower than that at 200masl, also indicating control by vertical structures.

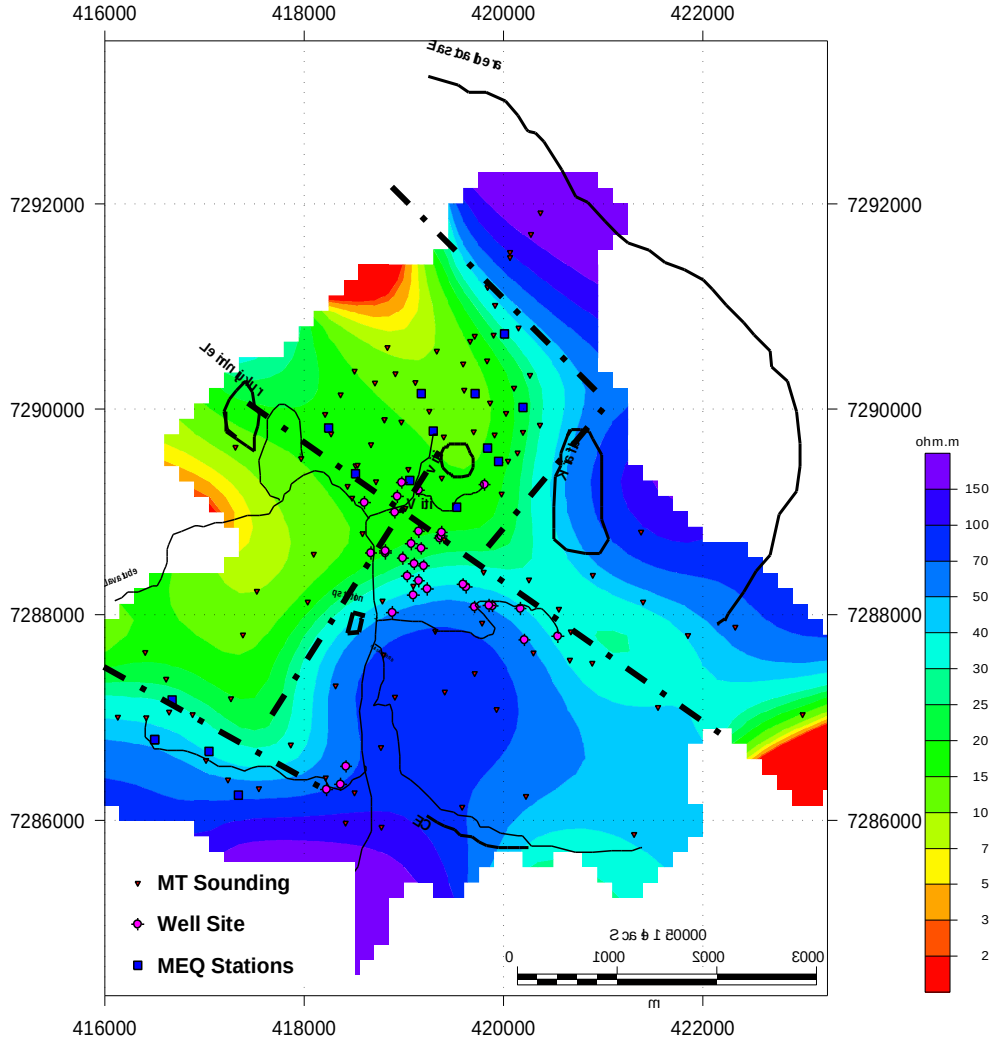

Figure 21: Occam 1-D resistivity map at an elevation of 200 masl. The blue colors indicate high resistivity while the red colors indicate low resistivity. The location of existing geothermal well sites is shown in pink; location of MT stations is shown in black triangles while the location of MEQ stations for the 2005 deployment is shown in blue squares. The resistivity boundaries are sharp, suggesting structural control with postulated NW and NE trending structural controls.

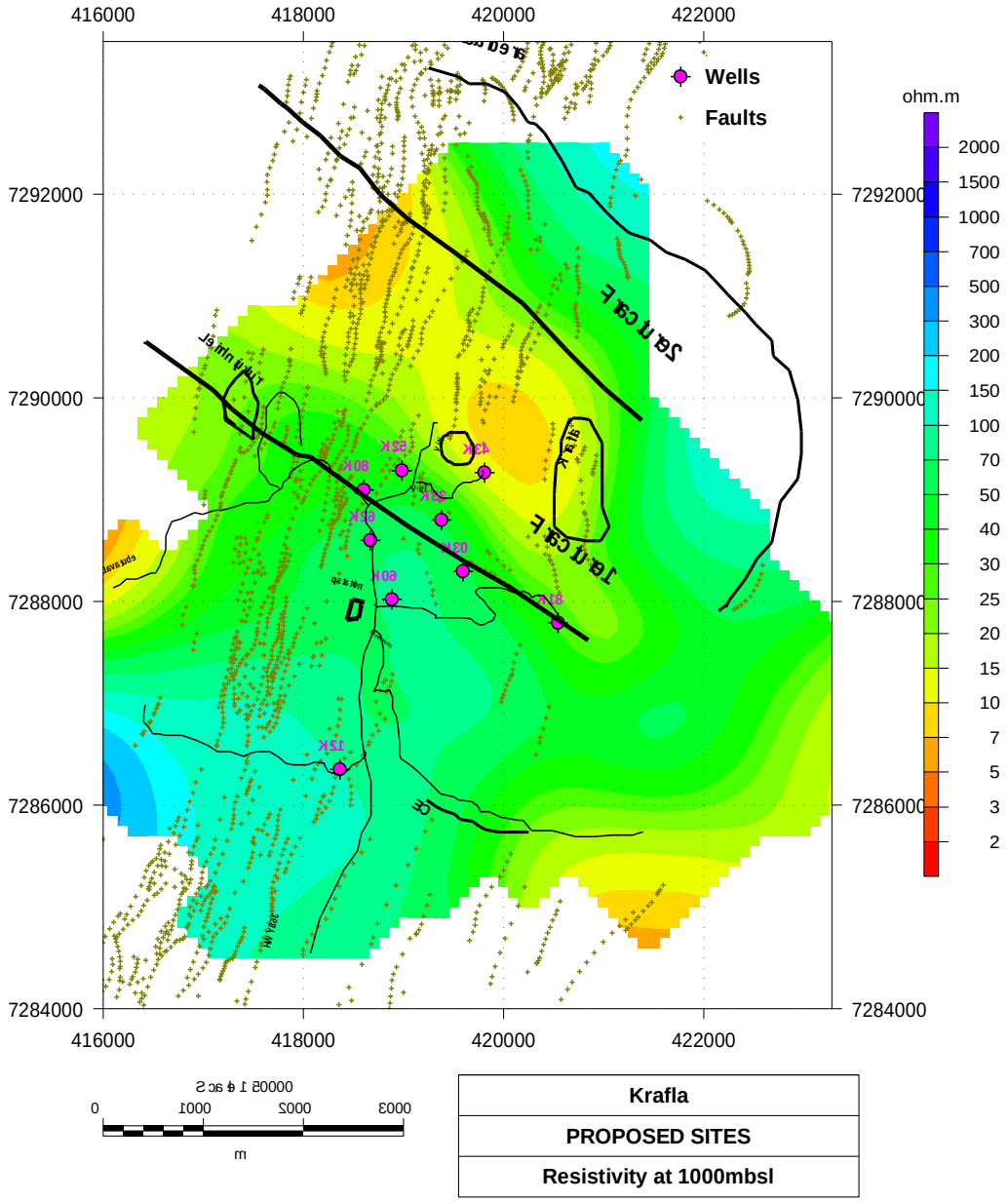

Figure 22: Occam 1-D resistivity map at an elevation of 1000mbsl. The blue colors indicate high resistivity while the red colors indicate low resistivity. The location of existing geothermal well sites is shown in pink; location of MT stations is shown in black triangles while the location of MEQ stations for the 2005 deployment is shown in blue squares. The low resistivity area is found mainly to the north of the present production area with a distinct NW-SE trend bound by high resistivity boundaries suggesting structural control.

At an elevation of 3,000mbsl (Figure 23), the low resistivity is about 3,000 ±10% m wide and covers a larger area than that at 1,000mbsl. The lowest resistivity zone occurs to the north of the study area with a distinct NW trending linear feature.

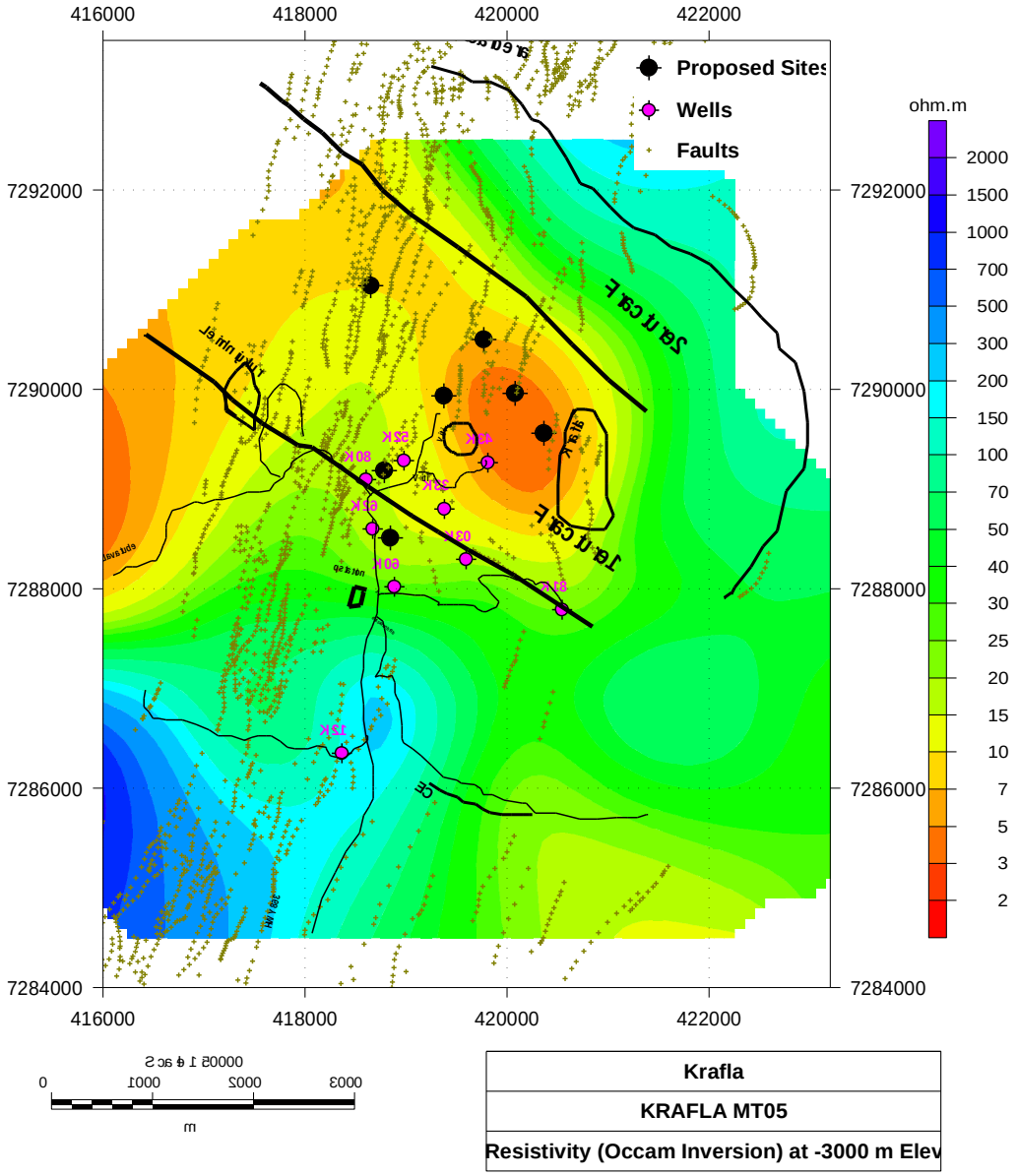

Figure 23: Occam 1-D resistivity map at an elevation of 3000 mbsl. The blue colors indicate high resistivity while the red colors indicate low resistivity. The location of existing geothermal well sites is shown in pink; location of MT stations is shown in black triangles while the location of MEQ stations for the 2005 deployment is shown in blue squares. The low resistivity area is found mainly to the northern part of the study area and covers a wider area than that at 1000 mbsl. The area to the south shows consistently high resistivity indicating that extends to a depth more than 3000m.

This low resistivity zone is interpreted as representing the top of the heat source for the hydrothermal system. As we discuss later in Chapter 4, this low resistivity zone coincides with the location of microearthquakes, which are located at depths less than 3km. The low resistivity area is found mainly to the northern part of the Krafla hydrothermal system. The area to the south shows consistently high resistivity indicating that the high resistivity extends to a depth more than 3,000m.

The hydrothermal system is therefore defined by a low resistivity zone that coincides with the location of shallow earthquakes. Most of the earthquakes occur above the deep, low resistivity which is interpreted as the heat source for the hydrothermal system. If this interpretation is correct, then it can be postulated that the deep, low resistivity represents partially molten rock that is interpreted as the heat source for the hydrothermal system. The low resistivity zone in also interpreted as area of low acoustic impedance, such that down-going S-waves are converted into up-going P-waves that have an arrival time between the up-going P- and S-waves.

3.5.3 2-D MT modeling

The model used in this dissertation consists of a fault zone which is defined as a region of high-fracture porosity. The fault zone consists of the main fracture with a core bounded by a damaged zone embedded in a host rock. The 2-D synthetic model is based on the conceptual model for the hydrothermal system (see Figure 5), the structural model of a fault zone (see Figure 6), existing models of S-wave and P-wave attenuation zones (see Figure 4) and the results of 1-D MT modeling. The choice of the orientation of the profiles was based on; the structural NNE trend of the fissure swarms; the trend of the postulated NW-SE transforms fault/shear zone and the conductance. The synthetic models were developed to test whether anisotropy can realistically be modeled using different mesh sizes and resistivity contrasts to simulate anisotropy at the base of the clay cap. The anisotropy is presumed to be caused by variations in resistivity within isotropic bodies which can also be modeled as columns of alternating high and low resistivity. In particular, for the case a hydrothermal system where fluids flow along faults and fractures, it is assumed that spatial variation in the physical properties of rocks on the scales of the fractures. However, the effect of alteration, temperature gradients and variations in hydrothermal fluids chemistry can cover a larger area than the fracture size.

The synthetic model (Figure 24) based on the geological and 1-D resistivity interpretation has a surface high-resistivity layer, corresponding to recent lava flows

and hyaloclastites. The surface layer resistivity was based on the TEM interpretation. The second layer has low resistivity and corresponds to the clay cap. This layer has variable resistivity at the base which can contribute to anisotropy. Third layer below the clay cap has higher resistivity than the low resistivity clay cap. The fracture zone is characterized by a low resistivity zone that increases in resistivity outward from the core.

The largest resistivity contrast is at the boundary of the fault zone and the host rock and also at the base of the clay cap and the heat source. Several forward models were tried out but only the best model which reproduced the splitting in the observed data is shown. The response of the 2-D model in the low resistivity zone shown in Figure 24 can also be modeled as a series of alternating high and low resistivity columns (Figure 25).

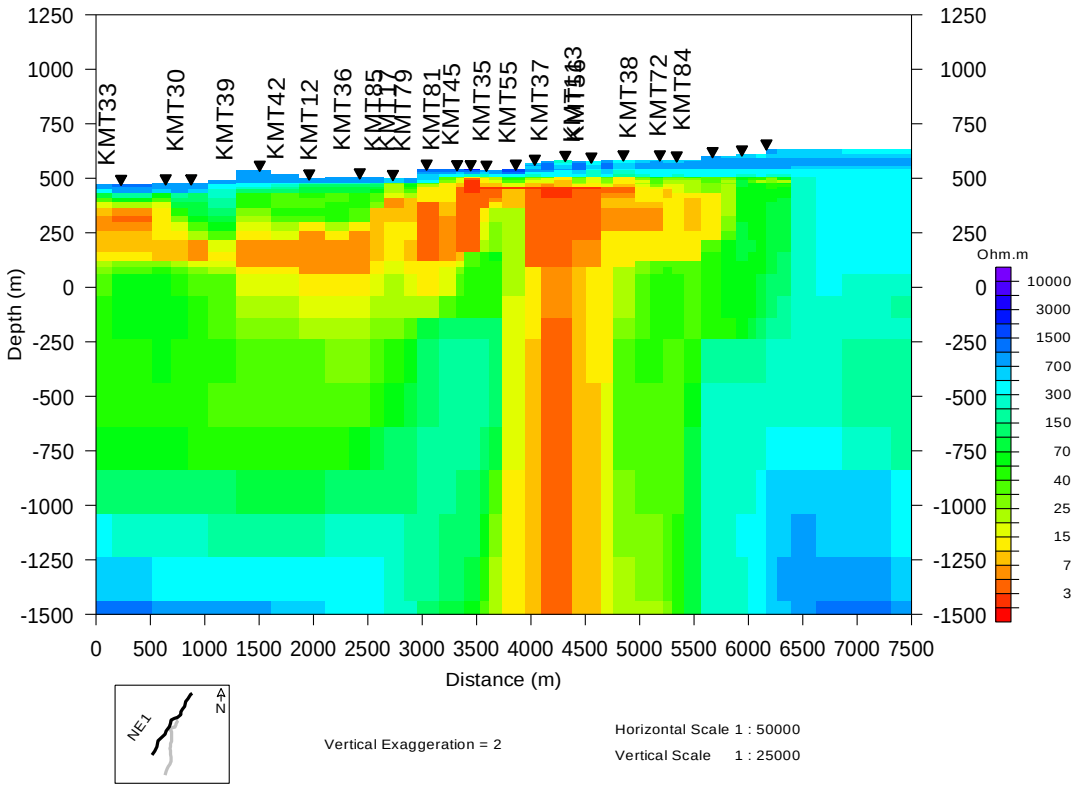

Figure 24: The synthetic 2-D resistivity model for the near surface layers close to a fracture zone modeled as an area of lower resistivity than the surrounding host rock which has higher resistivity. The clay cap is defined by the horizontal layer of low resistivity which can be viewed as a zone of columns of variable low resistivity extending from the base of the clay cap.

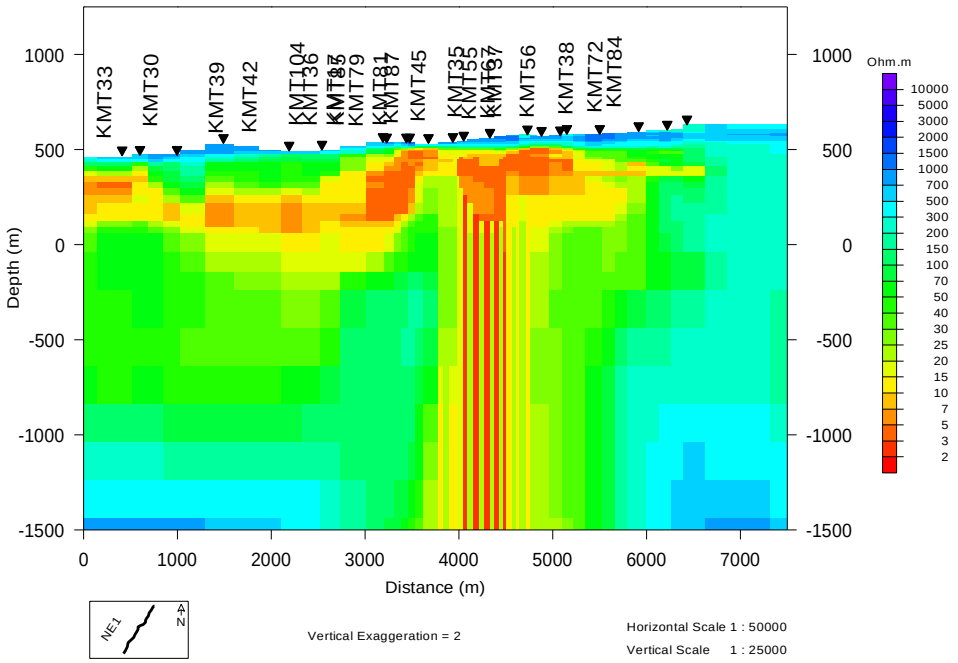

Figure 25: Synthetic 2-D resistivity model for the near surface layers close to a fracture zone modeled as an area of lower resistivity than the surrounding host rock which has higher resistivity. The resistivity in low resistivity zone below the clay cap is modeled as alternating columns of low and high resistivity extending from the base of the clay cap.

The model is sensitive to the depth of the base of the clay cap and the size of the fracture zone. Since most of the sites have a separation of about 300m the grids are interpolated between the stations. The vertical grid near the surface is about 30m increasing logarithmically with depth. The effects of vertical fractures are modeled as contrasts in resistivity. In general, the forward model has a nearly horizontal surface layer with high resistivity. The second layer has low resistivity mainly to the southwest and is underlain by high resistivity at depth. The resistivity close to the fracture zone shows considerable spatial variation both laterally and with depth. The lowest resistivity zone is centered on sounding KMT45. The resistivity increases laterally on both sides of the low resistivity zone.

The static shifts can be produced by inserting either more resistive or conductive lateral grids close to the measurement stations. The focus is mainly to model the observed splitting in the impedances phases of the MT data, by considering the spatial variation in resistivity below the clay cap. The response from models in figures 24 and 25 are the similar. This indicates that MT data might not differentiate between macroscopic and microscopic anisotropy at depth. The postulated heat source is modeled as a low resistivity zone (Figure 26) with resistivity increasing outwards from the center.

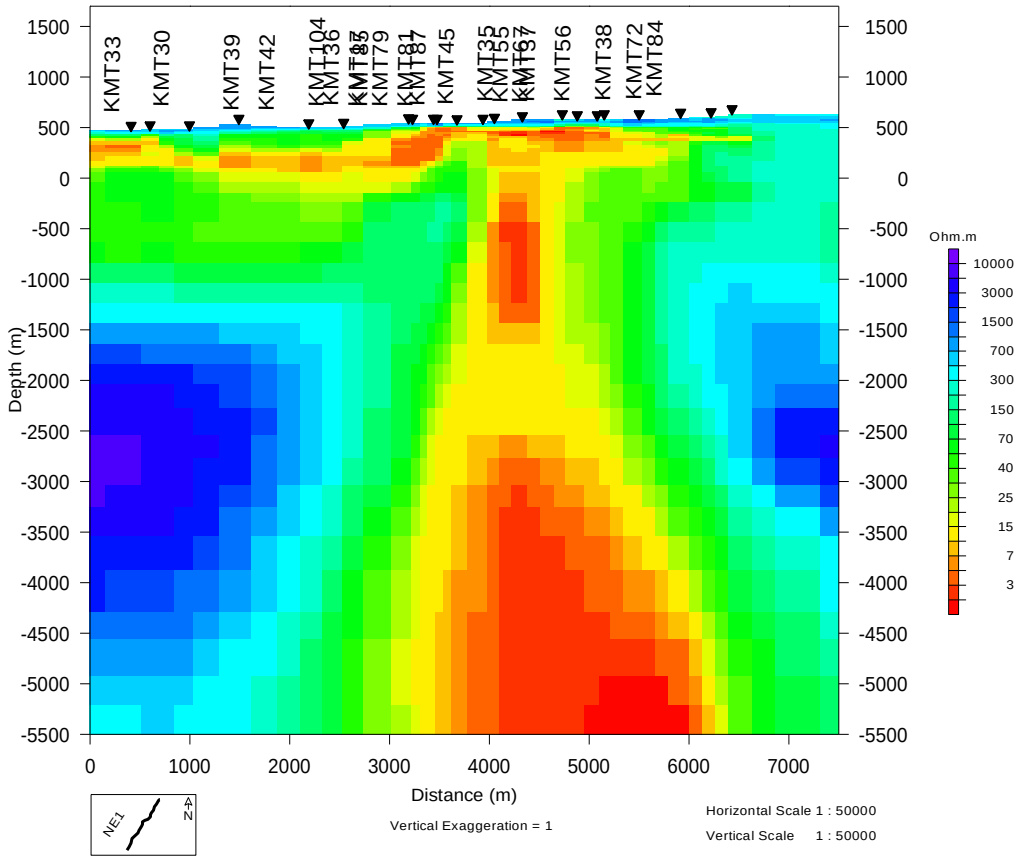

Figure 26: Synthetic 2-D model of the fracture zone including the postulated low resistivity heat source based on TEM and 1-D MT data of a NE-SW profile. The deep low resistivity zone is about 3km wide below a depth of 3km. The vertical column of low resistivity corresponds to the postulated core. Resistivity increases outwards from the core towards the host rock.

The low resistivity is bound by high resistivity which corresponds to the bulk resistivity of possibly unaltered basaltic rocks with either low temperature or low fracture porosity. The response for the forward model shows that the low resistivity zone affects the resistivity in one of principal resistivity directions in such a way that the resistivity continuously reduces with depth.

The response of the forward model shown below (Figures 27 to 30) produces shifts in the data in the vicinity of the postulated fracture zone. The amount of shift depends on the resistivity contrasts at depth and the proximity to the postulated fracture zone. The resistivity at data acquisition sites on both sides of the fracture zone shows very little splitting in the resistivity in the principal directions. From the forward model, it can be concluded that the splitting in the MT resistivity data is

mainly caused by the resistivity contrasts at depth rather than lateral surface contrasts.

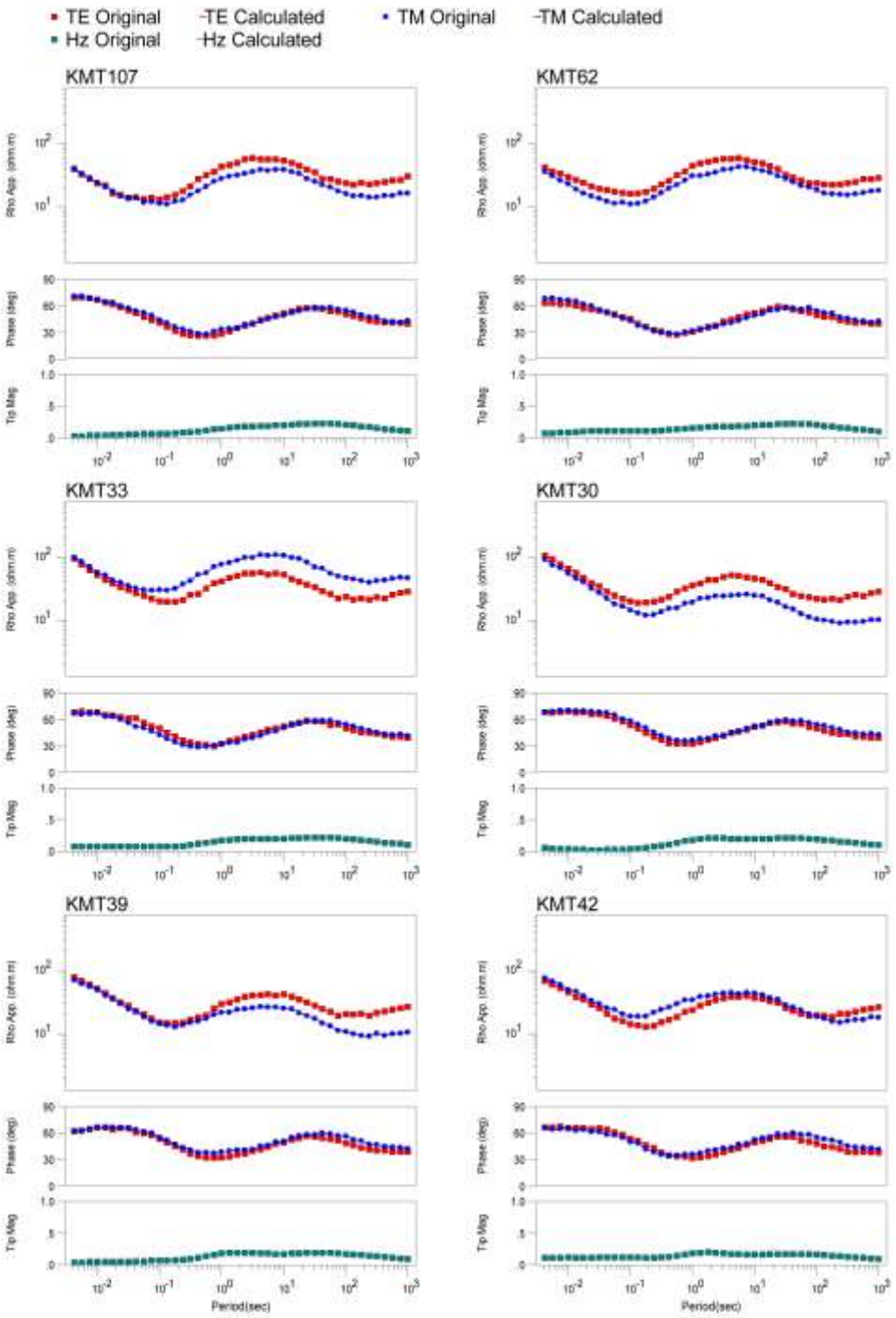

Figure 27: The response of 2-D forward model at the first six sites on profile NE1 in the Krafla hydrothermal system. These sites show 1-D resistivity characteristics with very little splitting in the TE and TM mode data sets.

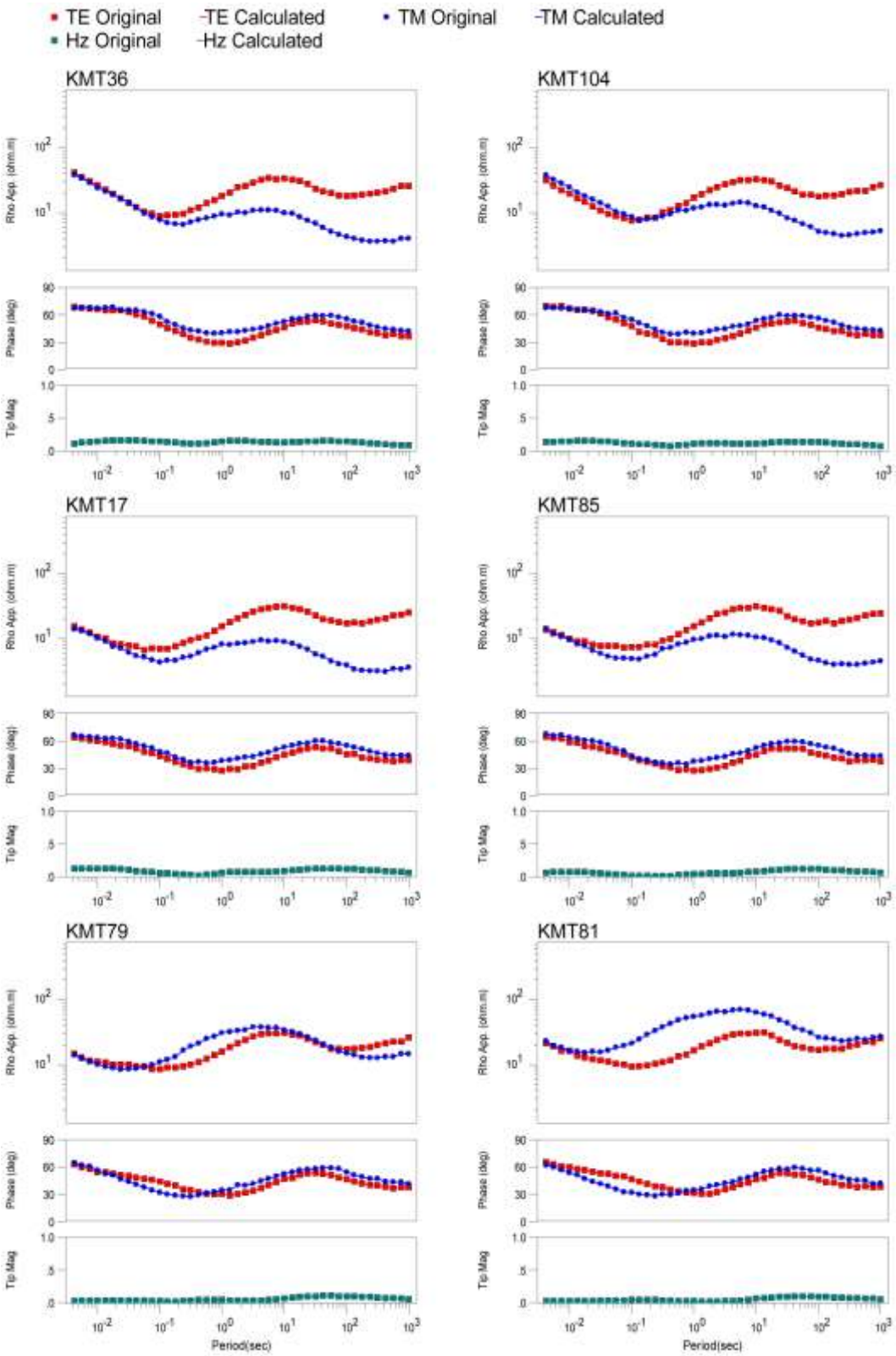

Figure 28: 2-D forward response for sites close to the fracture zone. The response shows significant splitting in the MT data. Some of the AMT soundings show very isotropic characteristics at high frequencies indicating that the anisotropy might be caused by resistivity contrasts at depth.

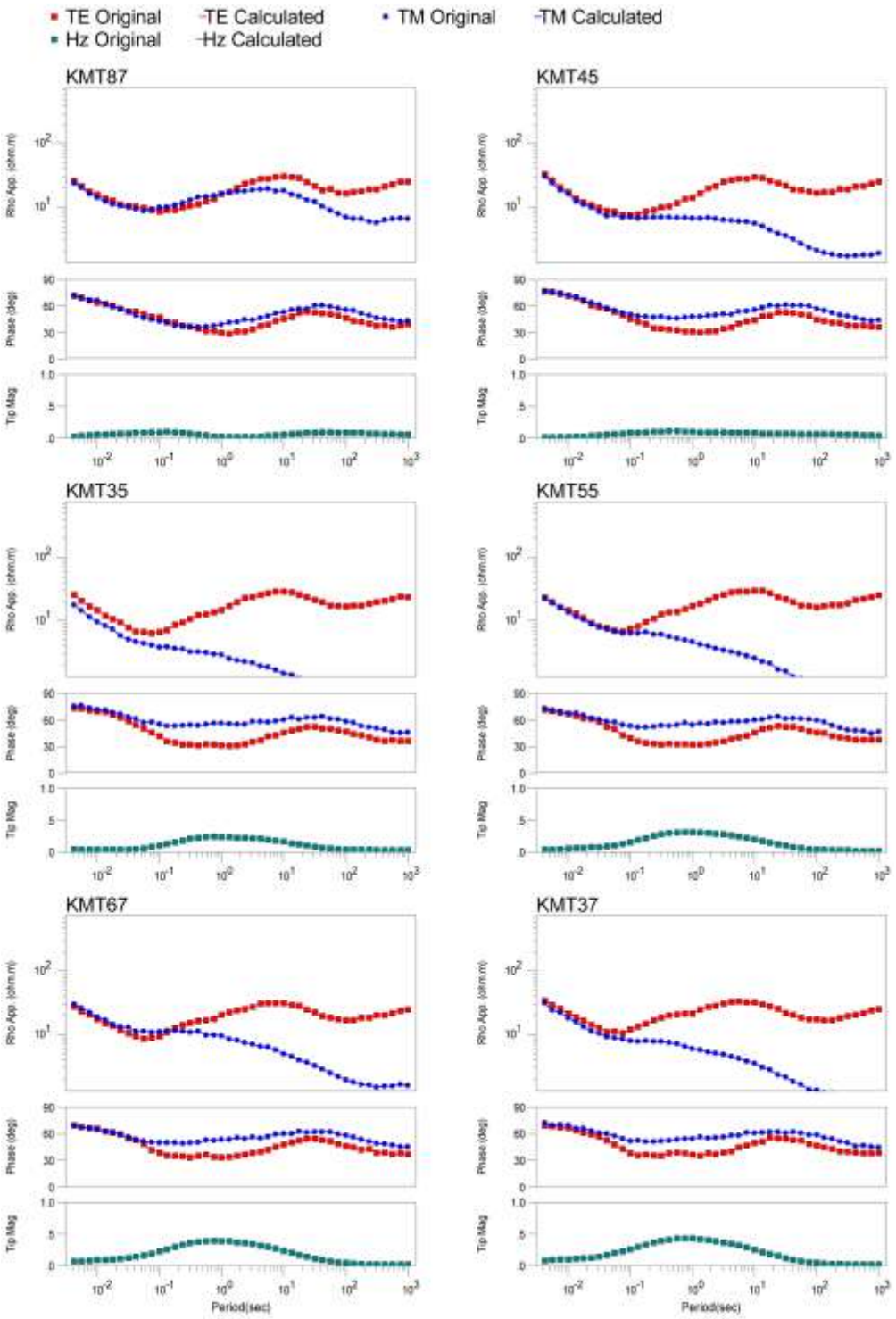

Figure 29: 2-D forward response for sites within the fracture zone. The response shows the largest splitting in the MT data. Site KMT87, which is located on the boundary of the postulated fracture zone shows very little splitting in the MT data at high frequency. The low resistivity in is the fracture zone and the postulated heat source. The splitting in the MT data is attributed to the resistivity contrasts between the lower resistivity in the fracture zone and the postulated heat source and the higher resistivity in the host rock.

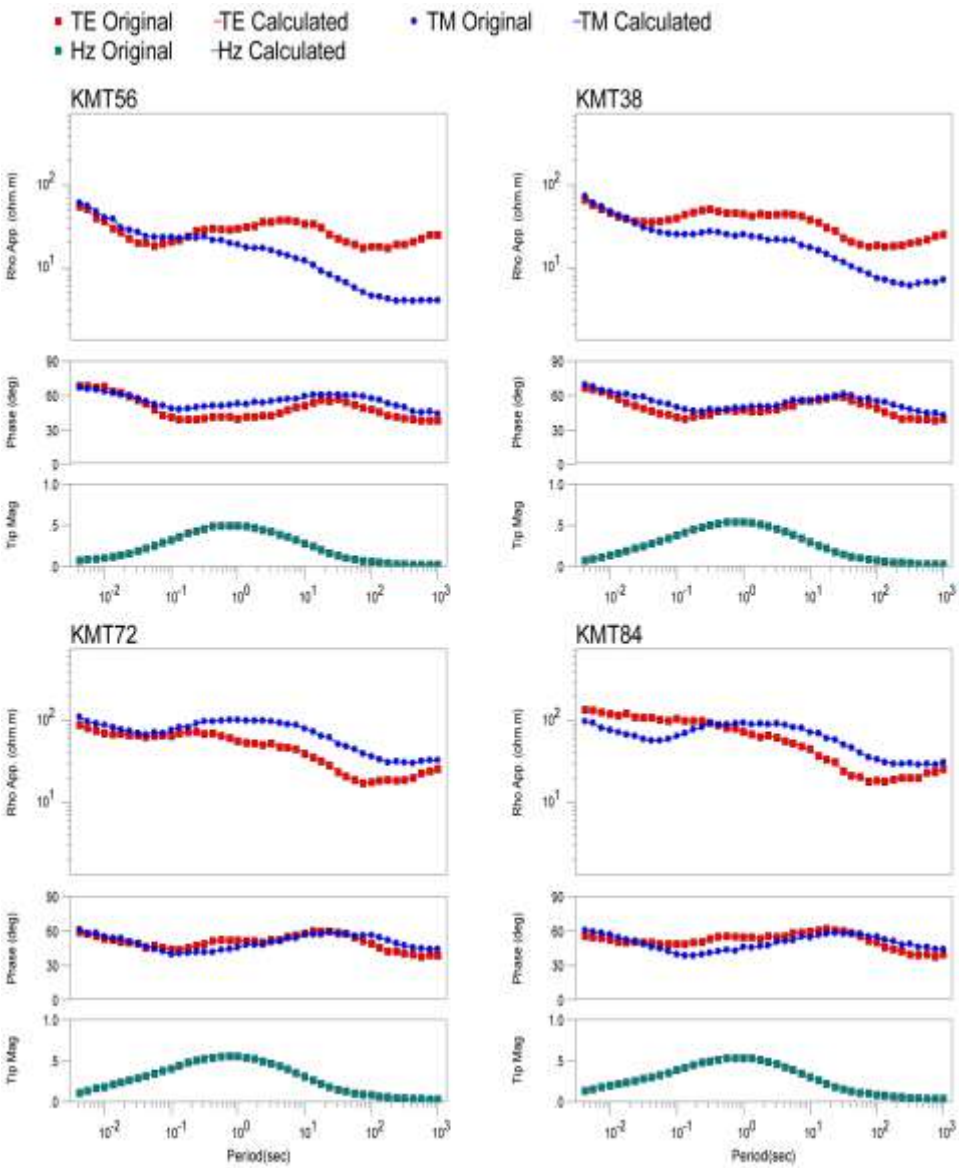

Figure 30: 2-D forward model responses for sites to the north east of the fracture zone. The response shows no splitting in the MT data. The last site on the profile KMT84 shows high resistivity and no anisotropy.

An alternative explanation might be that the resistivities at lower frequencies are affected by regional lateral inhomogeneities located some distance from the area of study. While this is possible from theoretical modeling, the available regional studies indicate (Bjornsson et al., 2005) show that the resistivity increases away from the active Neovolcanic Zone towards the older rocks. Modeling of the regional blocks are as high resistivity isotropic zones, cannot produce the consistent splitting observed on the MT data. Based on this results and the theory of shear wave splitting, we postulate that fluid-filled fractures within the hydrothermal system cause both S-wave and MT anisotropy. A comparison of S-wave and MT anisotropy is discussed in chapter 4.

3.2.3.2 2-D MT inversion across a fluid filled fault zone

The 2-D smooth model inversion routine in WinGlink (Mackie, 1996) was used to carry out the inversion of MT data. The inversion was carried out for both TE and TM modes for 6 decades of data on the log scale covering frequency range of 320-0.001Hz for the MT data and 10,400-0.1Hz for AMT data.

The choice of the profiles is based on the analysis of the data which shows significant structures trending in the NE and NW directions. It was therefore anticipated that the principal resistivity directions would be in these directions. The 2-D inversion was carried out on the same profile as that used for the forward problem with the desired misfit set to 5% for the resistivity, phase and the vertical magnetic field. The 2-D inversion shows a very good fit for both resistivity and phase for most of the data. The TM mode shows a better response than the TE mode and the vertical magnetic field for all the data.

The 2-D inversion model for profile NE1 across the postulated NW-SE trending structures (Figure 31) shows a low resistivity zone hosted within high resistivity.

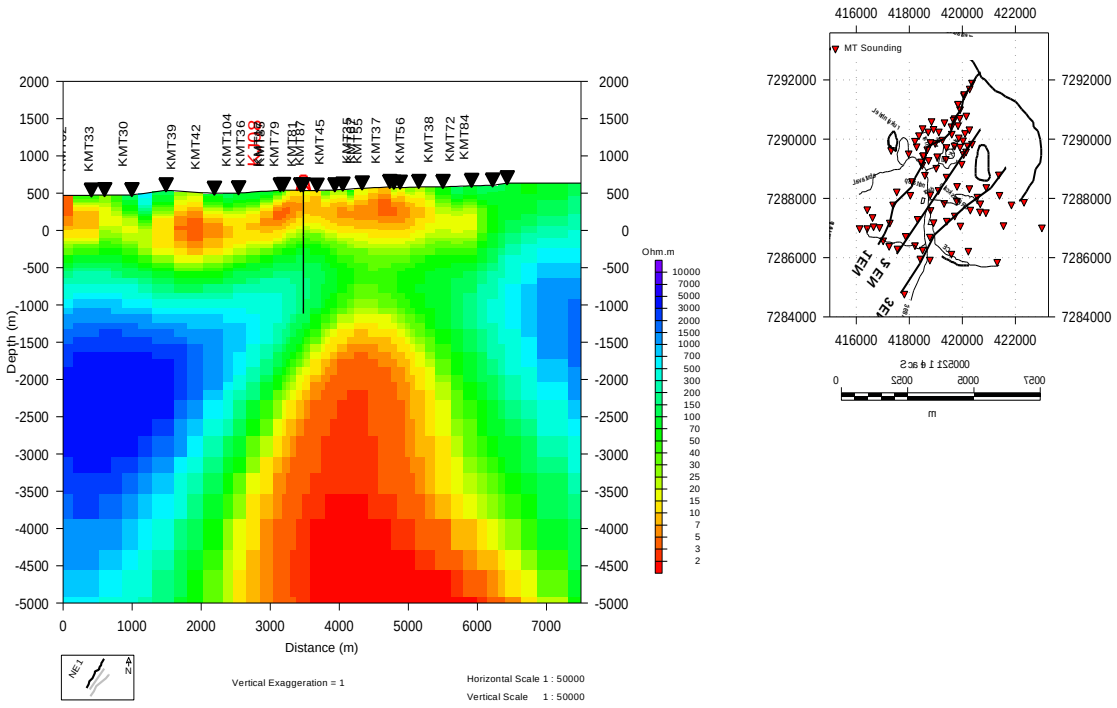

Figure 31: 2-D inversion model along profile NE1. The model shows low resistivity at a depth of more than 3,000m is interpreted as the heat source. The near-surface lateral low resistivity is interpreted as a hydrothermal reservoir at a temperature of 180-220 ˚C. The temperature was measured in well KJ08 (see figure 32) shown on the model.

Generally, the 2-D models can be divided into:

1. Near surface horizontal layer with high resistivity which corresponds to layers of recent volcanic rocks.
2. A second low resistivity horizontal layer which corresponds to the clay cap. This layer might be attributed to either hydrothermal mineral alteration caused by lateral movement of hydrothermal fluids or mixing meteoric water with gas from the underlying reservoir. This low-resistivity layer does not extend to the northeast, probably indicating that the lateral flow is mainly to the southwest or generally southwards. This layer is also present on the 2-D inversion profiles to the south on profile NE2.
3. The third layer shows considerable lateral variation in resistivities. A distinct low resistivity zone occurs within a high resistivity host rock. The low resistivity zone becomes wider with depth. The low resistivity zone has been interpreted as a fracture zone on top of a heat source. The low resistivity is attributed to circulation of hydrothermal fluids. The high resistivity zone may be attributed to lower fracture porosity and circulation of lower temperature hydrothermal fluids. The temperature from well KJ08 (Figure 32) supports this interpretation.
4. The lowest resistivity at a depth of more than 3,000m is interpreted as the heat source for the hydrothermal system within the Krafla caldera. The heat source seems to dip both to the northeast at southwest. In the southwest and northeast sections of the profile, the 2-D inversion model shows that the high resistivity (more than 100Ωm) zone is more than 4,000m thick.

The final RMS for the 2-D inversion was less than the targeted 5% for most of the MT data. The plots of the 2-D response together with the data show a similar trend to that of the synthetic model. The responses for stations that are far away from the fracture zone and the heat source show no difference between the TE and TM modes of the MT resistivity

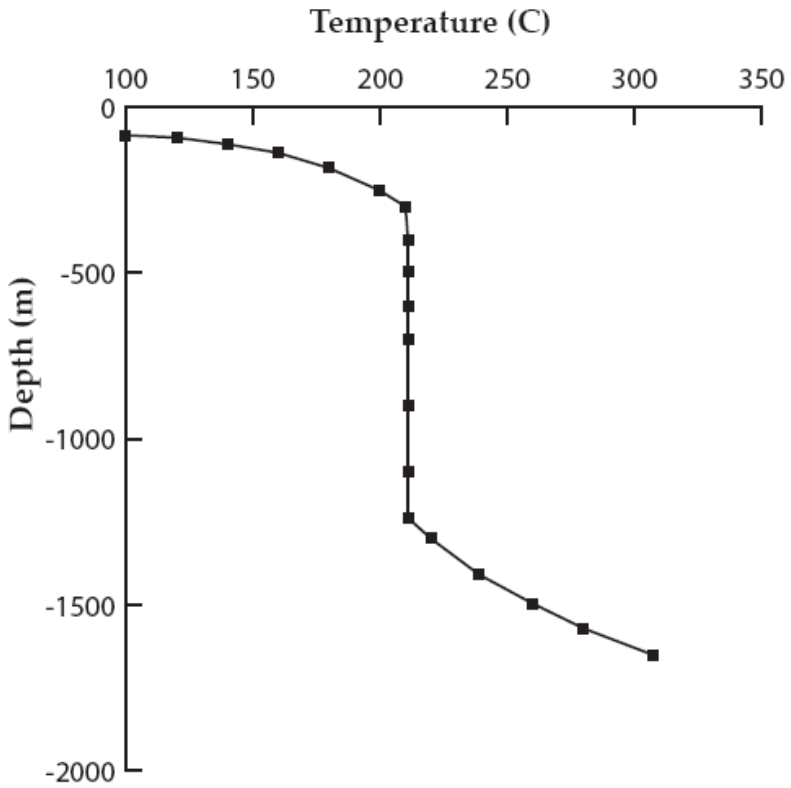

Figure 32: Graph of measured temperature in well KJ08 at Krafla geothermal field. Measured temperature (˚C) is plotted against the depth of the well (m). The graph shows that the temperature gradient close to the surface increases rapidly to a depth of 250 m. The temperature then shows isothermal conditions to a depth of 1240m. Below this depth, the temperature increases rapidly, indicating a conductive gradient.

3.5.4 3-D MT modeling

3.2.4.1 Data parameters and memory requirement.

One limitation of the code is the large memory required to store the sensitivity matrix. The total size of the dataset is defined by the data parameter N defined below:

$$N = N_p N_S N_r = 18*50*8 = 7200$$

Where N_p, in the number of periods which are 18 for this study, N_S is the number of stations (50 for this study) and N_r is the number of responses (maximum 8).

The model parameter size M is defined by the product of number of discretization blocks in the north-south direction (M_X), the number in the east-west direction M_y, and the number in the vertical direction M_y as shown below;

$$M = M_X M_y M_Z = 12000$$

The memory requirement is 1.2*(8*7200*7200+8*12000*12000) = 1880064000=1.88 Gbyte. This is a serious limitation in resolving the 3-D structure that can be used to map the structure of the hydrothermal system on a scale that can used to evaluate reservoir properties. Attempts were made to reduce the data to two samples per decade but still there was no converge in the sensitivity matrix. The sizes of the data blocks were also increased in an attempt to reduce the model size but still no convergence in the calculation of the forward model.

3.2.4.2 Data preparation

50 MT stations were chosen from the data to cover a nearly uniform grid covering an area of 5 km^2 around the Krafla hydrothermal system. The data at each site was reduced to 3 frequencies per decade for six decades. The data was edited manually to preserve the general resistivity trend at each site. After the editing, the data was transformed from the EDI format to the format required for the WSINV3DMT code using a Mat lab code. The data input file contains the number of stations, number of periods, and the number of responses (the real and imaginary parts of the off-diagonal and diagonal impedance tensors). The data locations are listed in meters with respect to the centre station. The initial model specifies the number of resistivity grids, the block sizes in the north-south, east-west and vertical directions. The resistivity distribution in each block is specified by pre-assigned resistivity indexes.

After spending 3 months working on this, we could not get the data to converge even after reducing the data at each site to 2 data points per decade. Any further reduction in data would results in poor model resolution. The limitation in this 3-D inversion is the computation memory.

3.3 MEQ data analysis

The data from two surveys carried out in July-August 2004 and August 2005 in the Krafla geothermal area was used to locate microearthquakes and evaluate shear wave splitting anisotropy. In the summer of 2004, twenty microearthquake monitoring stations sampled at 500 samples per second (2ms) were deployed in the

southern part of Krafla geothermal area. Additional data used in this research was collected by the University of North Carolina at Chapel Hill in July-August 2004. Additional MEQ data was collected by Duke University in the northern part of Krafla using 15 three component geophones with a natural frequency of 1Hz and a sampling rate of 250 samples per second (4ms). MT data was collected at the same sites. The mechanisms for generating earthquakes in hydrothermal systems have been outlined in the introduction.

3.3.1 Location of microearthquakes at Krafla

The locations of microearthquake stations were determined from the internal GPS measurements. The microearthquakes are located at a reference datum which is the average of the stations which is 550m. Station corrections are incorporated to account for the elevation differences with respect to average elevation. The station corrections are computed by locating many earthquakes with zero corrections and then assigning the average time errors as station correction.

In the 2005 data set, 198 MEQ events were used for the location of earthquakes with a minimum of 4 stations required to pick an event. In the 2004 data set, 50 MEQ events were used to locate the earthquakes. Only the high quality events with clear P and S-wave arrivals were used.

The earthquakes are found mainly in the hydrothermal systems with a NW-SE trend (Figure 33). The shallowest earthquakes are found to the northern part of the Leirbotnar and Sudirhlidar in the Krafla hydrothermal system and to the west of Krafla Mountain especially around well KJ34. Most of the earthquakes occur at elevations of less than 1800 mbsl. A second area of shallow microearthquakes is found in the area designated as Krafla NW to the north of Leirhnjukur. Most of the earthquakes in this area are found at a depth less than 1,200m. Stations K34 and K35 are the closest to this source. This area is close to the source of the 1979-1984 volcanic eruptions of basaltic lava flow. The area to south and southwest of the Krafla hydrothermal system recorded very few earthquakes during the field campaigns both in 2004 and 2005.

The shallow earthquakes around well KJ34 are associated with an area of high productivity and injection from the geothermal wells (Figure 34). From this observation, it is possible that the shallow earthquakes may be correlated to areas of enhanced fluid flow due to high fracture porosity.

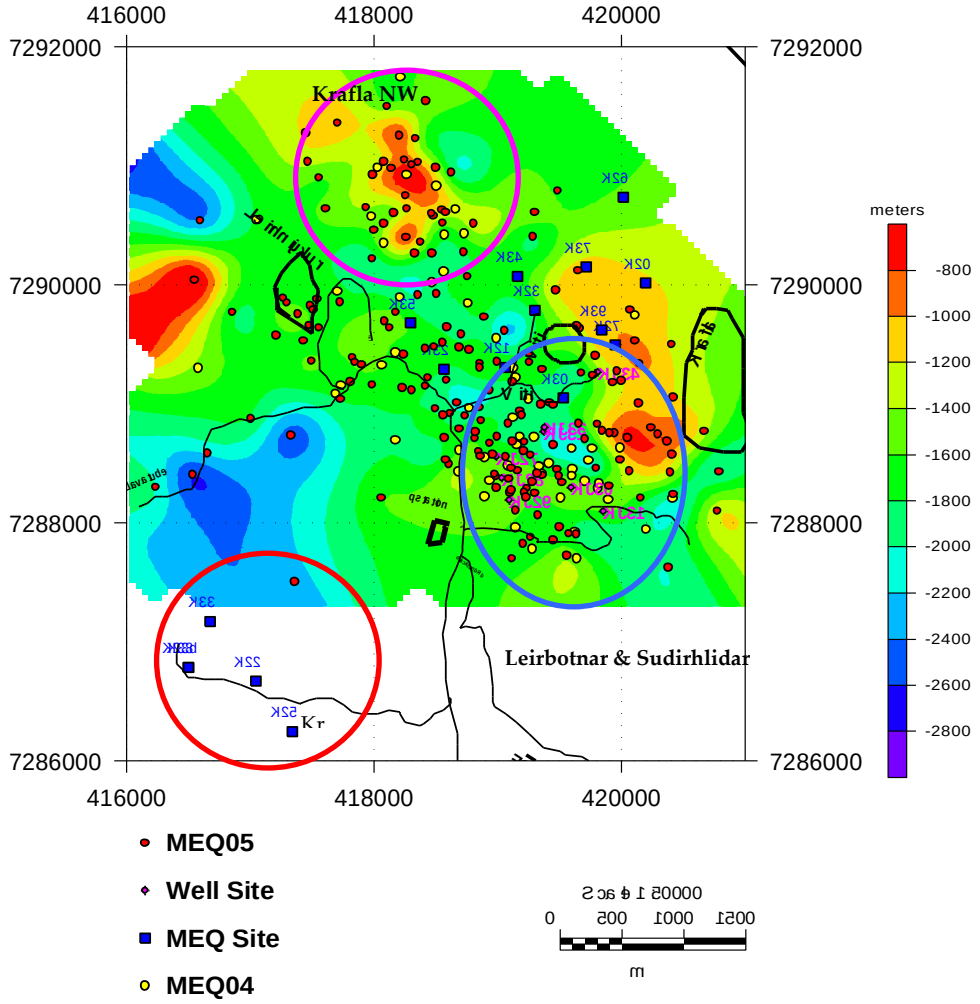

Figure 33: Plot of the elevation of microearthquakes from the 2004 and 2005 field campaigns at the Krafla geothermal field. Two areas of shallow earthquakes are found in the Leirbotnar and Sudirhlidar field and in Krafla NW area.

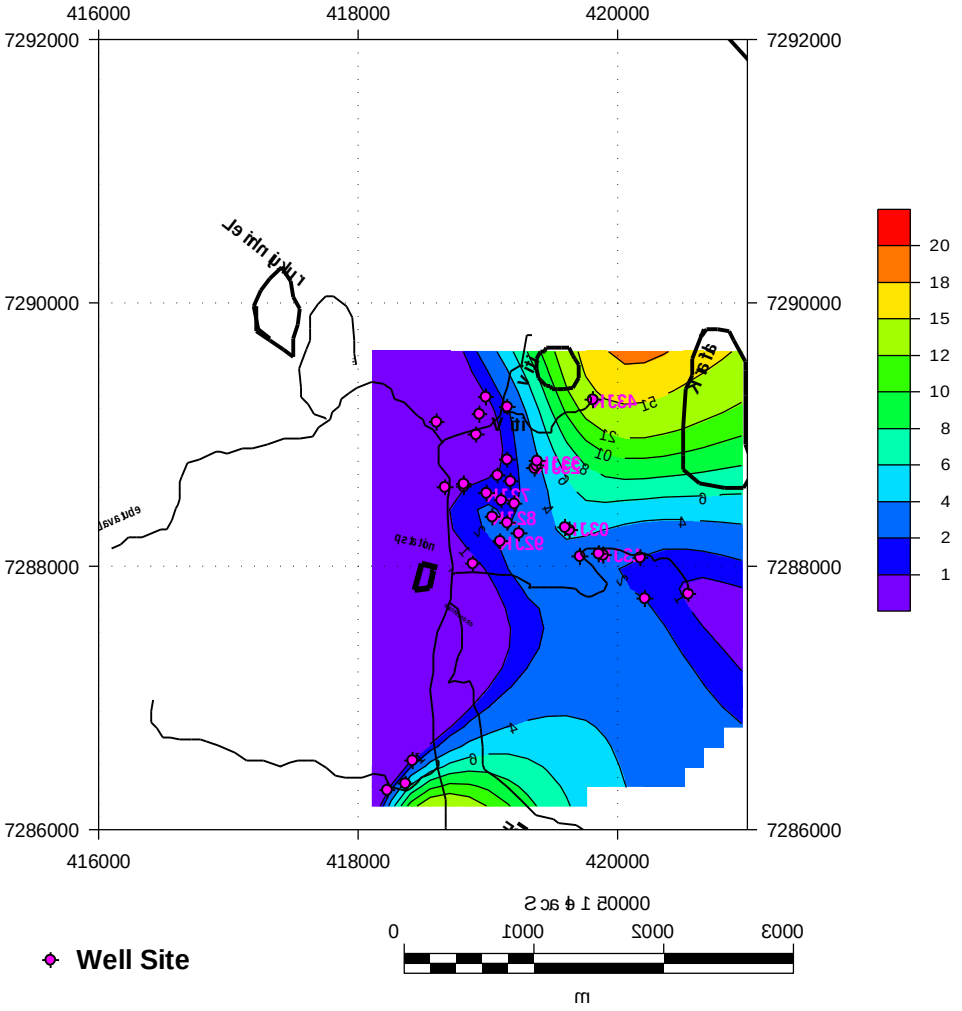

Figure 34: Plot of the output in megawatts (MWe) from the existing geothermal wells at Krafla. The highest production is found in the area around well KJ34 to the west of Mt. Krafla.

3.4 S-wave splitting and MT polarization results from Krafla

Some of the earthquakes recorded during the 2004 and 2005 field deployment at Krafla, Casa Diablo and Mt. Longonot show shear-wave splitting. An example of shear wave splitting is given for station K21 from Krafla with a time delay after rotation to the principal directions (Figure 35). The coda for the earthquake is less than 2 seconds and the difference between P-and S-wave arrival is less than 0.5 seconds.

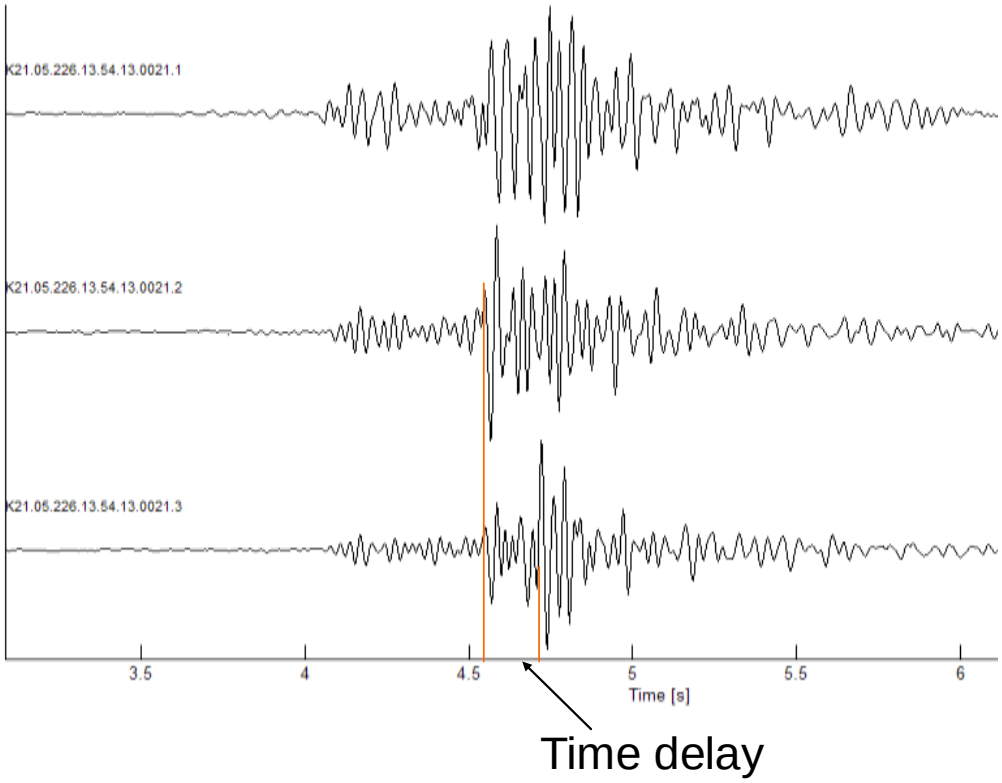

Figure 35: An example of shear wave splitting from Krafla in Iceland with clear P-wave and S-wave arrivals. The time delay is less than 0.2 seconds.

In shear wave splitting models, the only data available is arrival times and location of stations. In this dissertation, it is assumed that S-wave splitting is caused by vertical fluid-filled fractures. The fast S-wave is aligned in a direction parallel to the fractures while the slow S-wave is aligned in a direction perpendicular to the fractures. In general, the fractures are aligned parallel to the direction of maximum compression stress. The time delays between the fast and slow S-waves give information about the average crack density along the ray paths. The main interest is to determine the shear wave polarization direction and compare it to the polarization in the magnetotelluric data.

The major problem is determining the sizes, depth and density of fractures. In hydrothermal systems, the interest is in large-scale fractures that channel hydrothermal fluids. In developing the fracture model, emphasis is on the size, orientation, depths and intersection of fractures. Some studies of shear wave splitting have been carried out in some geothermal fields like the Geysers (Elkibbi and Rial, 2005, Elkibbi et al. 2005). Shear wave splitting data in the Geysers is interpreted as due to stress-aligned fractures in otherwise isotropic medium (Rial and Elkibbi 2000). The time delays were found to be between 8 and 40 milliseconds per kilometer.

When shear wave splitting is observed after rotation to the direction of fast and slow polarization, the corresponding time delay was determined. Both the polarization direction (θ) and time delays (δt) can be used to estimate crack density and anisotropy.

The shear wave polarization directions for each site is determined and compared to that of MT data. All the MEQ data were evaluated for shear wave splitting and polarization directions by rotating the S-wave particle motions to fast and slow polarization directions. This was done by searching for the angle that maximizes the amplitude ratios of the horizontal components of the S-waves. After rotating the S-waves in the direction parallel and perpendicular to this angle, the time delay was found by cross correlation of the amplitudes. For site K21, a total of 106 out of 198 microearthquakes analyzed from the 2005 field deployment showed shear wave splitting. Further analysis showed that 50 events had high quality data (Figure 36).

The mean direction for the 51 events at site K21 is about 48±10 degrees from north with a range generally between 30 and 60 degrees. The time delay varies between 8 and 132 milliseconds. Generally, the smaller time delays seem to occur at lower angle polarization directions while higher time delays occur at slightly higher angle polarization directions. This would seem to suggest that maybe there are two orientations with different amounts of fluid content.

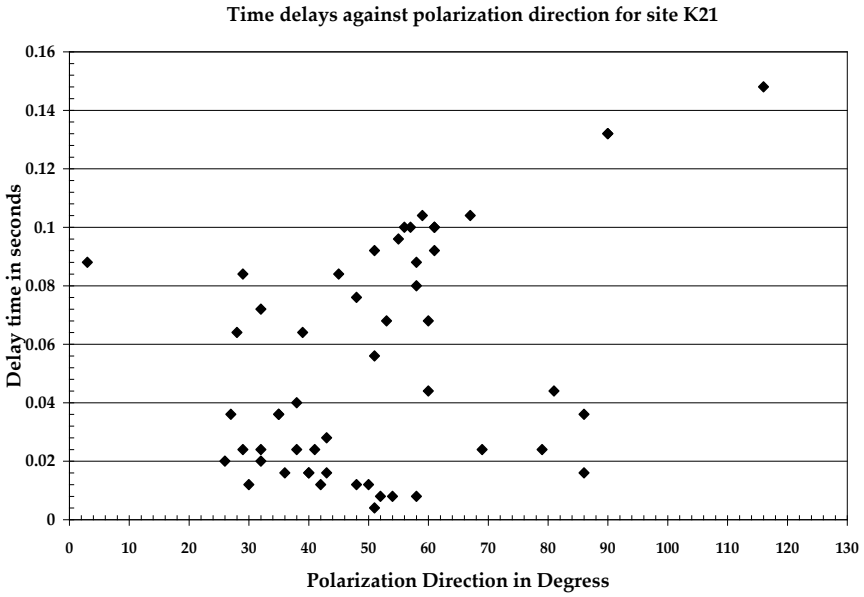

Figure 36: Plot of the polarization direction of the fast shear wave against the delay time for 51 events for site K21 at Krafla. The time delay varies from 8 to 132 milliseconds. The polarization direction is mainly between 30 and 65 degrees with a mean value of about 48 degrees.

In comparison to the polarization direction at different frequencies for the MT data at the same site (KMT115), the MT tipper strike direction is about 45 degrees for the frequency range of 10400 to 4.10 HZ. The tipper strike direction changes to a higher angle at frequencies between 4.10 and 0.127 HZ (Figure 37). This shows that the deeper structure might have a different strike direction from that at shallow depths. The orientations of the shallow and deeper structures are therefore expected to play an important role in controlling ground water and hydrothermal fluid movement.

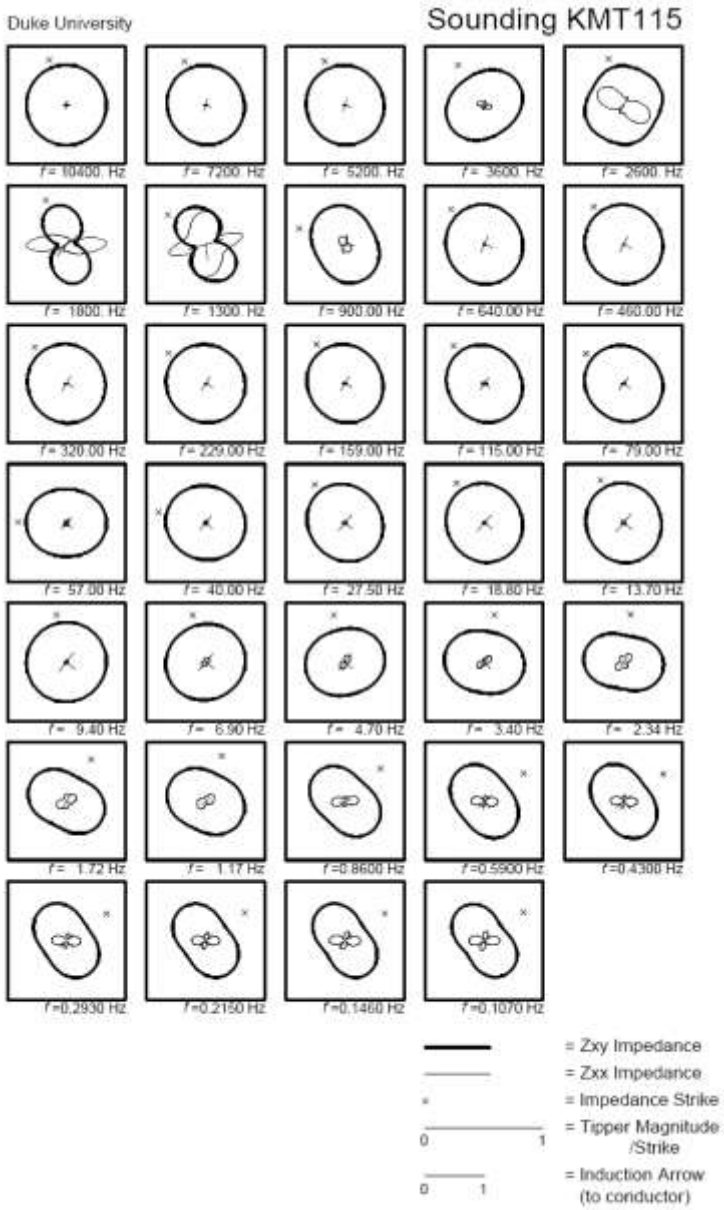

Figure 37: Plot of Zxy and Zxx impedances, impedance and tipper directions after static stripping for site KMT 115 collocated with MEQ site K21. The magnitude of Zxy is much more than Zxx, indicating that the resistivity at this site is nearly 1-D.

A statistical analysis was carried out on both MT strike direction and the fast shear wave splitting direction for site KMT 115 and K21 (Figure 38) by plotting the median polarization direction for each bin of 10 degrees for the range of 0-180 degrees. The dominant polarization direction for both MT and shear wave splitting is 30-60 degrees.

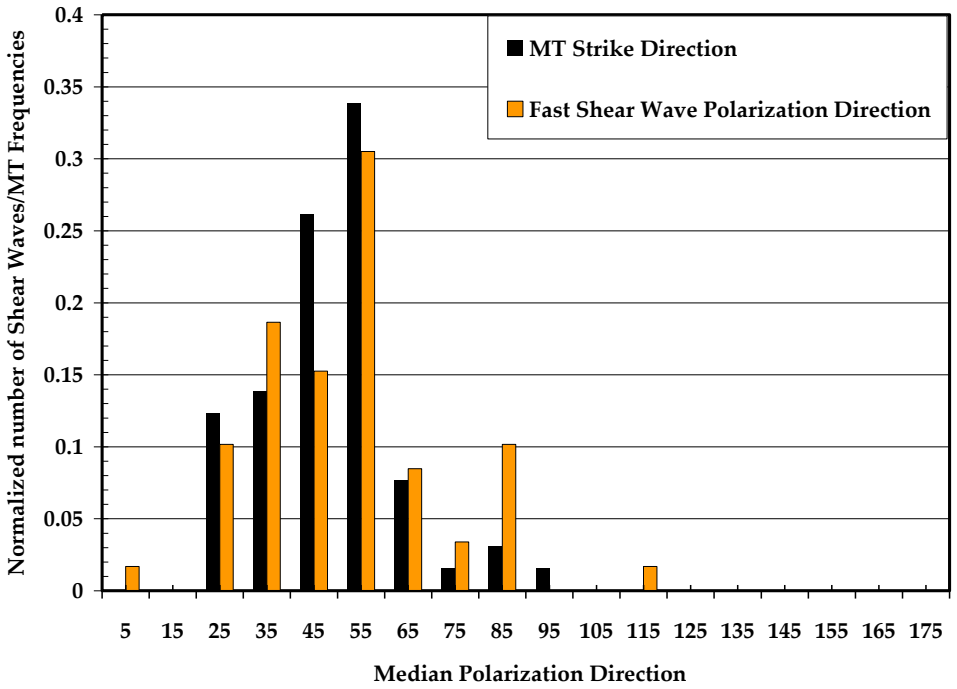

Figure 38: Plot of normalized fast S-wave splitting direction for site K21 and MT strike direction for site KMT115. The dominant polarization directions for both fast S-wave splitting and MT strike are between 20 and 60 degrees from the geographical north.

Further analysis of the S-wave splitting data for MEQ sites K21, K32, K34, and K35, shows that sites K21 (Figure 38) and K34 (Figure 39) have similar polarization direction, which is different from that at sites K32 (Figure 40) and K35 (Figure 41). Site K34 has a dominant polarization direction of 40-80 degrees while K35 has a dominant polarization direction of 100-130 degrees.

The results of the S-wave splitting for all the data collected at Krafla show that there are two dominant directions (Figure 42) in the EW to NW direction and nearly N to NE direction. S-wave splitting occurs predominantly in the northern part of Krafla geothermal field. This would seem to suggest that fluid-filled fractures found in this area have two structural trends. This region is also associated with significant splitting in the MT data. However, it is important to note that some of the MT data shows very high splitting at relatively high frequencies, suggesting that the

anisotropy might be a shallow effect close to the stations. Some of the stations with significant MT splitting at high frequency do not show any significant shear wave splitting.

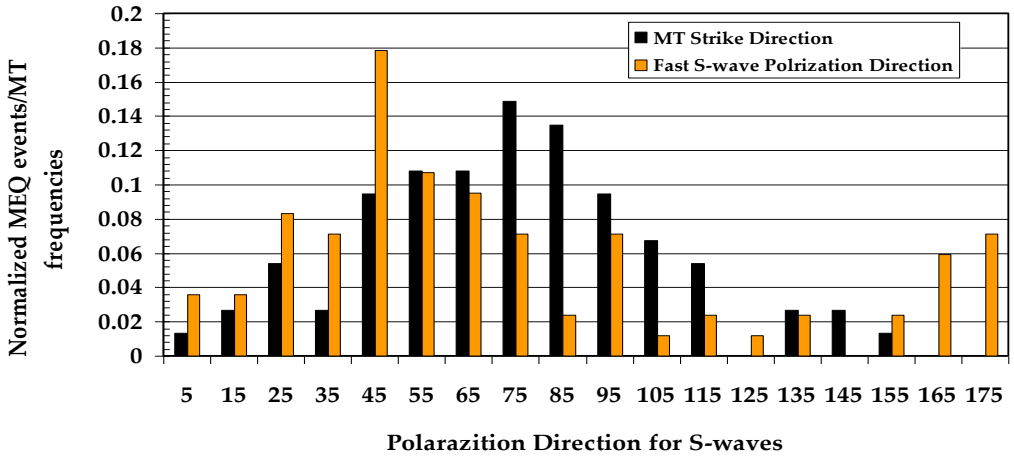

Figure 39: Polarization of the fast S-wave splitting at site K34 and MT strike directions at site KMT91 in the Krafla hydrothermal system. Dominant direction for both data sets is between 20 and 100 degrees from the geographical north.

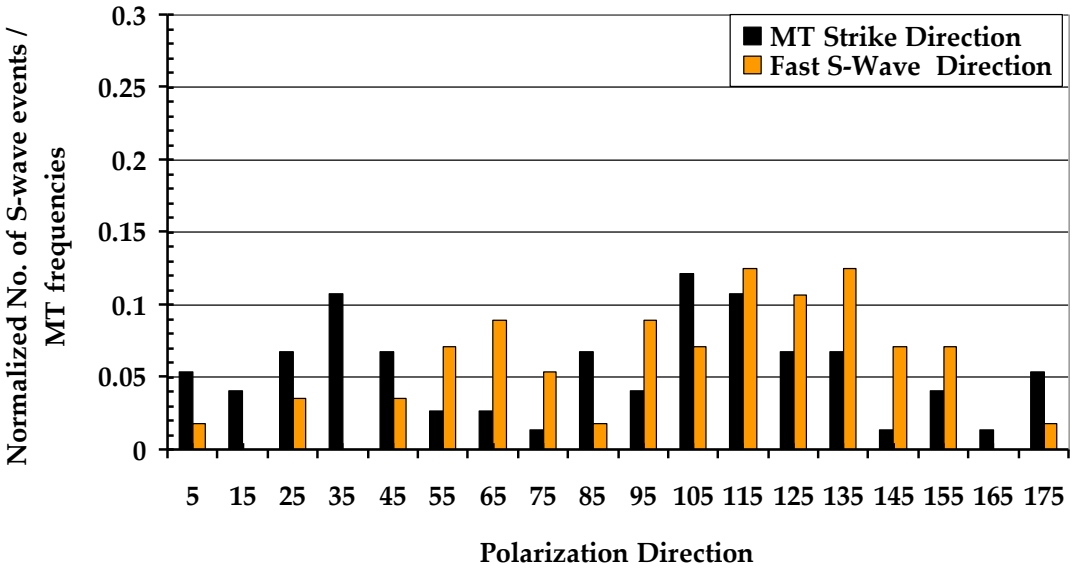

Figure 40: Polarization of the fast S-wave splitting at site K32 and MT strike directions at site KMT73 in the Krafla hydrothermal system. The dominant fast S-wave polarization direction is mainly between 90 and 140 degrees. The MT strike direction is mainly between 90 and 140 degrees from the geographical north.

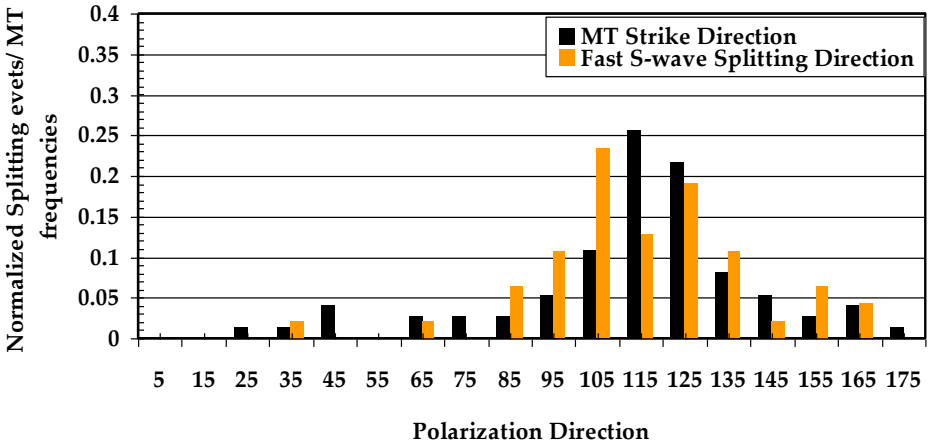

Figure 41: Polarization of the fast S-wave splitting at site K35 and MT strike directions at site KMT44 in the Krafla hydrothermal system. Dominant direction for both data sets is between 90 and 130 degrees from the geographical north.

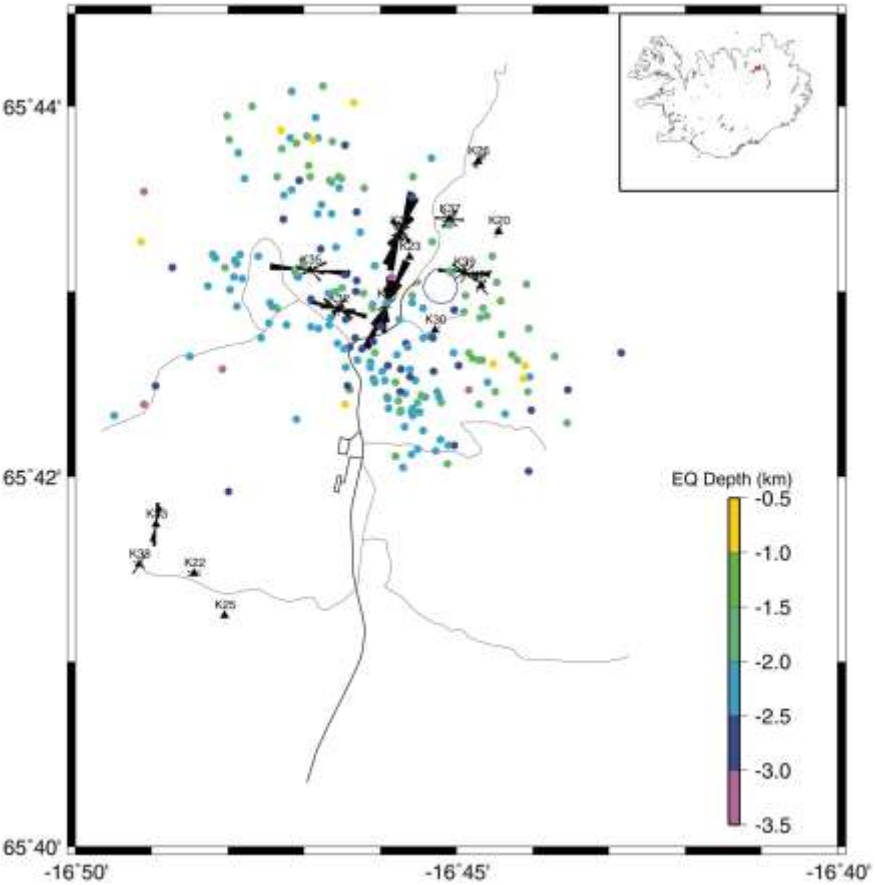

Figure 42: Shear wave polarization directions for the MEQ data collected from the Krafla hydrothermal system. The polarizations are plotted for bins of 10 degrees. Most of the microearthquakes occur within a NW-SE trend and are found at a depth of less than 2500 m. Sites K32 and K35 have the same polarization while K34 and K21 have the same polarization.

The shear wave splitting directions for the northern part of Krafla are similar to those obtained from MT data tipper strike directions (Figure 43) with two main directions.

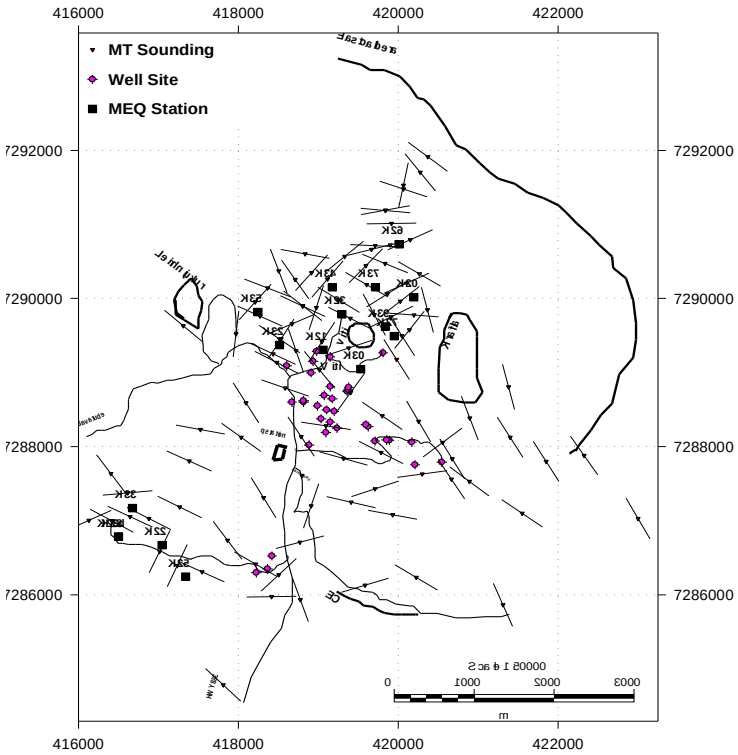

Figure 43: MT polarization directions for averaged data from Krafla for the high frequency range 320-100 HZ corresponding to shallow depths. The northern part of Krafla shows two main polarization directions in the NE-SW and WNW-NSE. The southern part shows mainly one direction of polarization. These polarization directions are similar to those of shear wave splitting (see Figure 42).

The dominant direction is generally in the NW-SE direction which seems to be the dominant regional trend in the Krafla Caldera. The other direction is in the NE-SW direction which is sub-parallel to the rift axis. The NE-SW trending polarization is more dominant at high frequencies of the MT data. In contrast, the NW-SE trending structures persist to lower frequencies indicating a deeper regional trend. This may suggest that the NE-SW trending structures that are sub-parallel to the rift axis are shallow. These trends are also parallel to the NW-SE and NE-SW trends of the interpreted Caldera. The MT tipper strike direction for low frequencies (Figure 44) shows a dominant direction that varies between nearly E-W to NW-SE. The E-W trend in the northern part of Krafla is similar to that obtained from shear wave splitting at some sites.

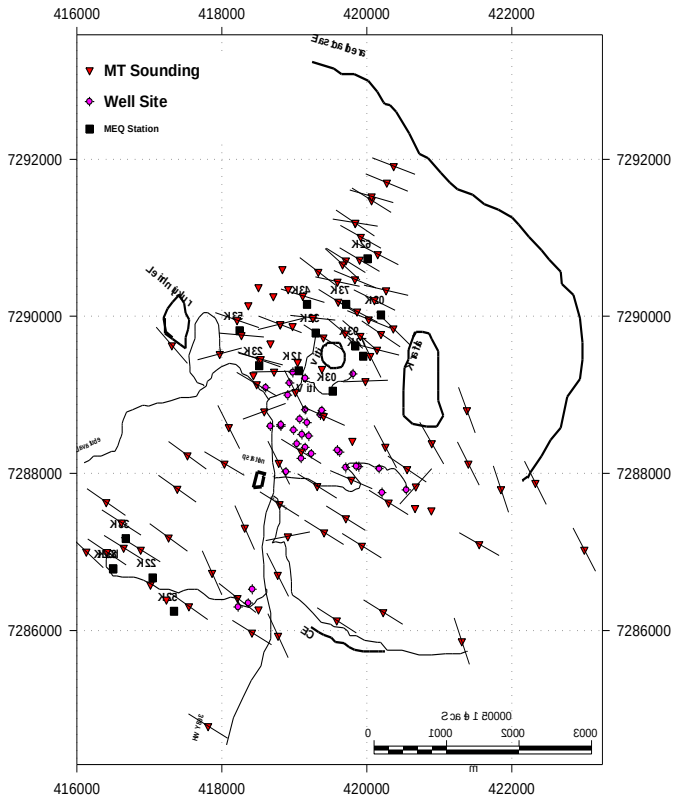

Figure 44: MT polarization directions for averaged data from Krafla for the low frequency range 0.025-0.004 HZ corresponding to the deep structure. The dominant structure in the Krafla area is mainly in the NW-SE. This polarization direction is similar to that obtained for S-wave splitting for some of the stations (see Figure 42).

As discussed later in Chapter five, the NW-SE trend might be related to the some of the NW-SE trending transform faults. These structures might therefore be important channels for circulation of deep hydrothermal fluids while the NE-SW trending structures might be important in channeling fluids at shallow depths. Since S-wave splitting occurs in the last zone that the zone that the waves propagate through, combined use of MT and shear wave splitting might very be useful in identifying the depths at which the splitting occurs. An analysis of the depth (Table 2) at which the MT splitting occurs indicates the splitting occurs at shallow depths at KMT 91.

Table 2: Depth at which splitting in the MT data occurs at 4 of the sites with significant number of S-wave splitting records at Krafla

MT Station	MEQ Station	Depth
KMT 91	K34	430±10%
KMT 115	K21	830±10%
KMT 44	K35	760±10%
KMT 17	K32	760±10%

The analysis of MT polarization at different frequency windows shows spatial and frequency dependence. Quantitatively high frequencies give an indication of the polarization at shallow depths while low frequencies show the polarization at deep levels. The polarization at 200 Hz, which is the average direction over the frequency range 320-100 Hz, shows three main directions of orientation. The main directions are NW-SE, NE-SW and EW. These directions are similar to those of mapped faults. The earthquakes are also located along these faults that continue to the south of the study area. At lower frequencies of about 1 Hz, the polarization is mainly in the NW-SE direction indicating that the overall regional resistivity strike direction is in this direction. However, a few sites show a NE-SW trend and E-W trend (Figure 44).

The polarization directions both from MT measurements and S-wave splitting are the same as the directions of the main faults. The earthquakes within the study area and to the south also occur along the faults. This indicates that some of the faults might be active and as such may create high fracture permeability. If the factures are filled with fluids, then the areas that recorded the highest number of S-wave splitting events and large time delays may be interpreted as high permeability zones.

3.5 Analysis of Vp/Vs ratios

In general for any station (i) station, the travel time is expressed in terms of the distance, arrival time, origin time, and the P-wave velocity. The plots of the difference between the S-arrival and the P-arrival time $\left(t_s - t_p\right)$ against the P-arrival time t_p for some selected earthquakes shows that there is a variation in the V_p/V_s ratios given by the slope of the gradient of the graph. The V_p/V_s ratio varies between 1.66 and 1.89 (Figures 45 and 46). Analysis of many of the earthquakes gives an average V_p/V_s ratio of about 1.75 which is consistent with values of 1.75-1.76 determined by travel times from P and S-waves from shots and microearthquakes in northern Iceland (Menke et al., 1998).

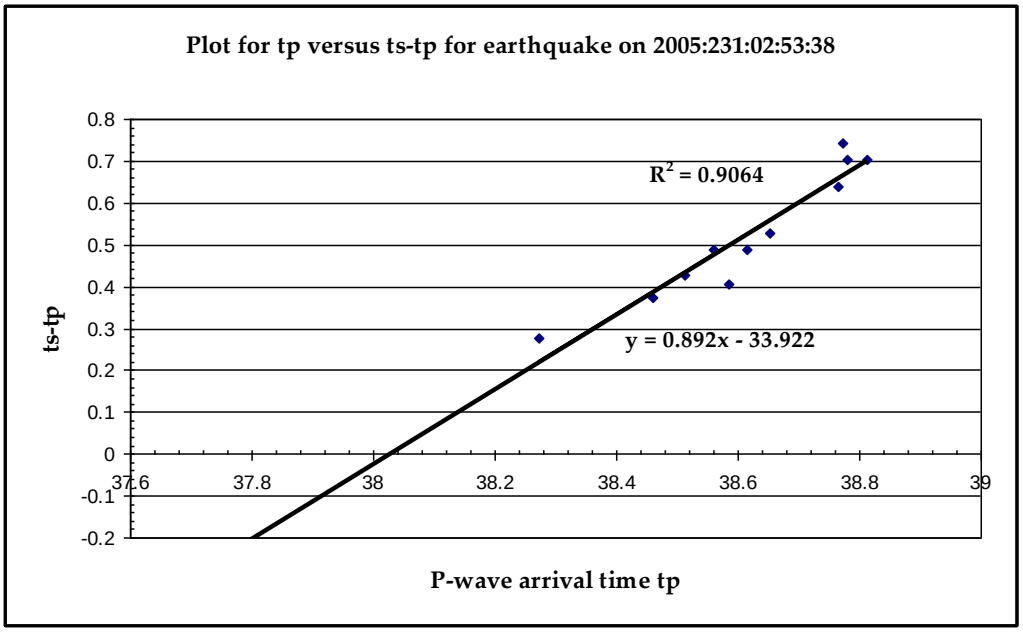

Figure 45: Plot of P-wave arrival time against the difference between the S-wave arrival and the P-wave times for an earthquake at the Krafla hydrothermal system. The gradient is used to obtain the V_P/V_S ratio.

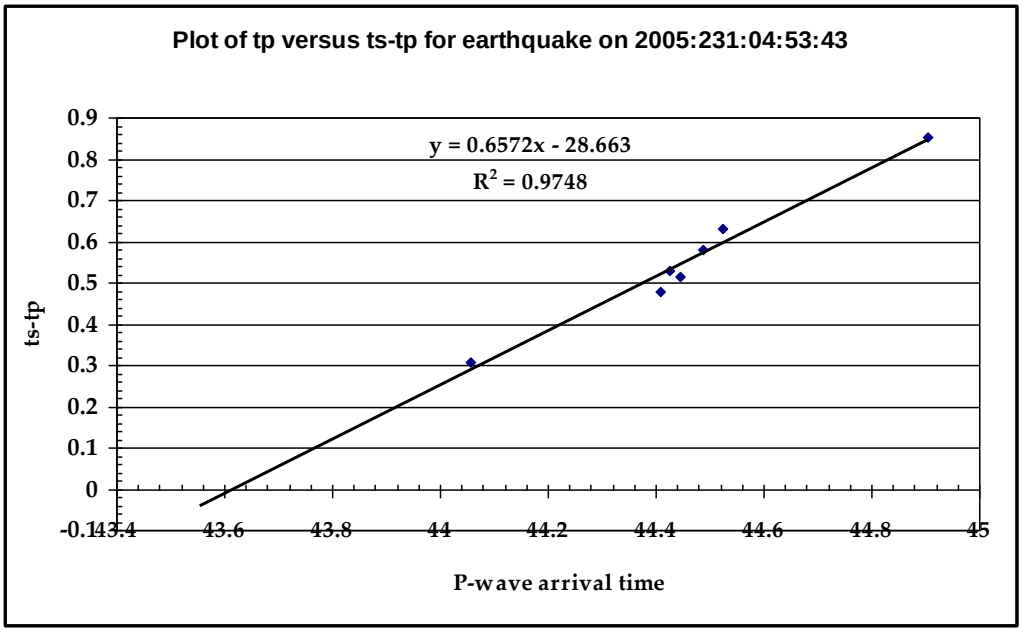

Figure 46: Plot of P-wave arrival time against the difference between the S-wave arrival and the P-wave times for an earthquake at the Krafla hydrothermal system. The gradient is used to obtain the V_P/V_S ratio.

3.6 Analysis of possible relationship between S-wave splitting anisotropy and MT anisotropy

The number of earthquakes recorded at all the three case study sites at Krafla, Mt. Longonot, and Casa Diablo were very few for a 3-D tomographic inversion. We have therefore made an attempt to analyze the postulated relationship between S-wave splitting and MT anisotropy. The analysis is based on equation 2.38 for MT resistivity anisotropy and equation 2.56 for S-wave splitting. In this analysis, we used the data from the four sites at Krafla that recorded excellent S-wave splitting and MT anisotropy. The depth to the base of the clay cap was determined from the MT measurements (Table 2) to normalize the S-wave splitting anisotropy. This was based on the assumption that S-wave splitting is caused by aligned systems of open, fluid-filled fractures below the clay cap. The plot of the normalized MT and S-wave anisotropy (Figure 47) shows a linear relationship.

Table 1: Normalized MT and S-wave anisotropy at four of the sites with excellent number of S-wave splitting records at Krafla

MT Station	MEQ Station	Depth	Normalized MT anisotropy	Normalized MEQ anisotropy
KMT 91	K34	430	1.77	0.46
KMT 115	K21	830	0.98	0.29
KMT 44	K35	760	0.75	0.27
KMT 17	K32	760	0.69	0.23

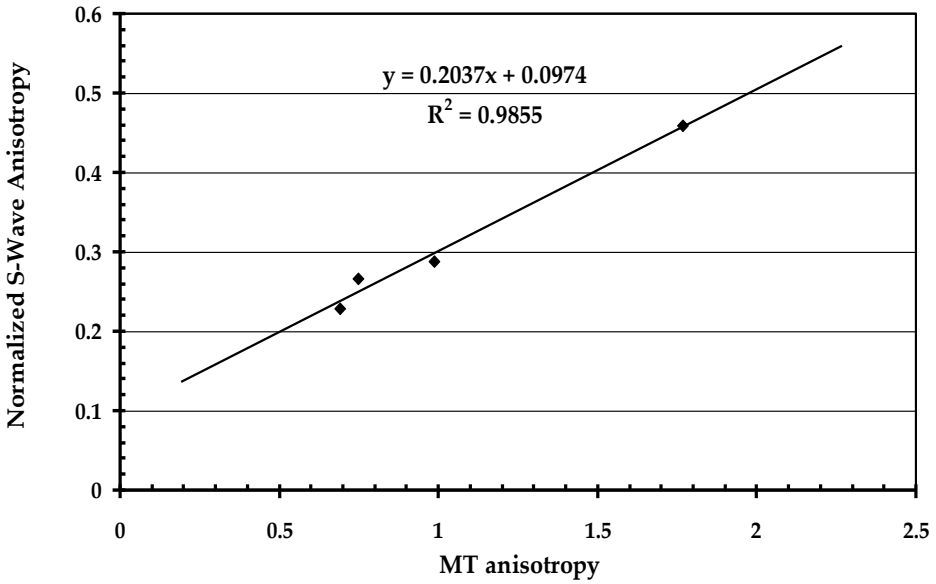

Figure 47: Plot of normalized MT and S-wave anisotropy and collocated sites with exceptionally excellent S-wave splitting.

A Vp/Vs ratio of 1.75 was used to evaluate equation 2.56. This preliminary result indicates that there might be a linear correlation between the S-wave anisotropy and MT anisotropy. This result is complementary to that determined in section 3.4 of this dissertation that showed a strong correlation between S-wave splitting polarization and the MT tipper strike directions. This led to the conclusion that both measurements are affected by fluid-filled fractures. The area around MT station KMT 91 and MEQ station K34 have the highest anisotropy. This result can be very useful in modeling anisotropy both in MT and S-wave data to determine both fluid-filled fracture density and depth to the base of the clay cap. The areas with the highest anisotropy could be the best targets for drilling high production geothermal wells. This result will be included in the future joint tomographic modeling of fluid-filled hydrothermal systems that show significant MT and S-wave anisotropy.

4. Joint interpretation of earthquake and resistivity measurements across buried fault zones in hydrothermal systems

The changes in the measured resistivity values across a site are interpreted as variations in fracture porosity with depth. The higher resistivity, in the direction perpendicular to the electric strike is used as an estimate of the bulk resistivity of un-fractured rock. The resistivity and velocity are affected by porosity, fluid content and type, degree of fracturing, rock grain size and the clay content. We assume that porosity affects the propagation of seismic waves through the medium at collocated data acquisition sites. The available geological well data are used to evaluate the degree of hydrothermal alteration to complement the joint interpretation of resistivity and earthquake data. This information is useful in comparing resistivity and isotherms and the rank of hydrothermal mineral alteration.

Fractured rocks will tend to have high porosity, and therefore generally high interface conduction and possibly lower resistivity. Resistivity of near surface material is heavily affected by groundwater and rank of hydrothermal alteration. We have modeled the MT frequency dependent anisotropy to show the changes in anisotropy with depths using a similar scheme developed by O'Brien and Morrison (1997), who indicated that the larger scatter in the TE and TM mode resistivity can be accounted for by changes in azimuthal polarization. Heise and Pous (2001) point out that it is generally hard to determine whether the splitting in the MT resistivity curves at a site are caused by anisotropy or 2-D or 3-D effects. In this dissertation, we have assumed that in hydrothermal systems, the splitting in MT data is caused by effects of fluid flow in a fractured fault zone. This scheme is used for the MT data in Krafla where the downhole geology is reasonably uniform and the near surface is quite homogenous. The anisotropy modeling has been carried out after using TEM data to correct the static shifts in MT data. Synthetic MT undistorted by statics was computed from co-located TEM 1D models and actual MT data was static shifted to fit the synthetic MT.

4.1 P-wave velocity models from resistivity data

Based on the assumptions in this dissertation, it is possible to generate a velocity model from the measured resistivity with the assumption that for resistivity above 130 Ωm, the P-wave velocity approaches that of the rock matrix of un-fractured and unaltered rock. This limit of resistivity dependence on porosity might be different for each hydrothermal system depending on the degree of fracturing, the chemistry of pore-fluid, degree of hydrothermal alteration, rock type and temperature.

As an initial example, we consider the average invariant resistivity for a 7-layer model for the sites in the area where most of the earthquakes are located. The resistivity is obtained from the averages of all the 1-D models within the NW-SE trending fractures. The relationship between resistivity and porosity is used to obtain the corresponding values of porosity in each layer, which is then used to compute P-wave velocity (Table 3).

Table 2: Computed P-wave velocity from resistivity values obtained from MT data. The upper limit for the resistivity-porosity dependence is 70 Ωm; above this value the porosity approaches zero, while the P-wave velocity is equivalent to that of the unaltered host rock.

Resistivity	Porosity	P velocity from MT
5	0.50±10%	2500±200
7	0.25±10%	3460±200
10	0.15±10%	4200±200
15	0.13±10%	4390±200
20	0.10±10%	4700±200
25	0.08±10%	4935±200
30	0.07±10%	5060±200
40	0.05±10%	5335±200
50	0.04±10%	5485±200
70	0.01±10%	6170±200

The 1-D velocity model generated from this approach compares well to previous models used to model seismic data in the Krafla area (Brandsdottir et al., 1997). The main difference is at depth, where previous models assumed that velocity generally increases with depth. The 1-D models documented by Brandsdottir et al. (1997) show sharp increases in velocity with depth (Figure 48). The model generated from resistivity generally agrees with the models used in experiments in Krafla in 1963 and 1973. The model used in 1995 shows higher velocity values, which correspond to areas with higher resistivity where very few earthquakes occur.

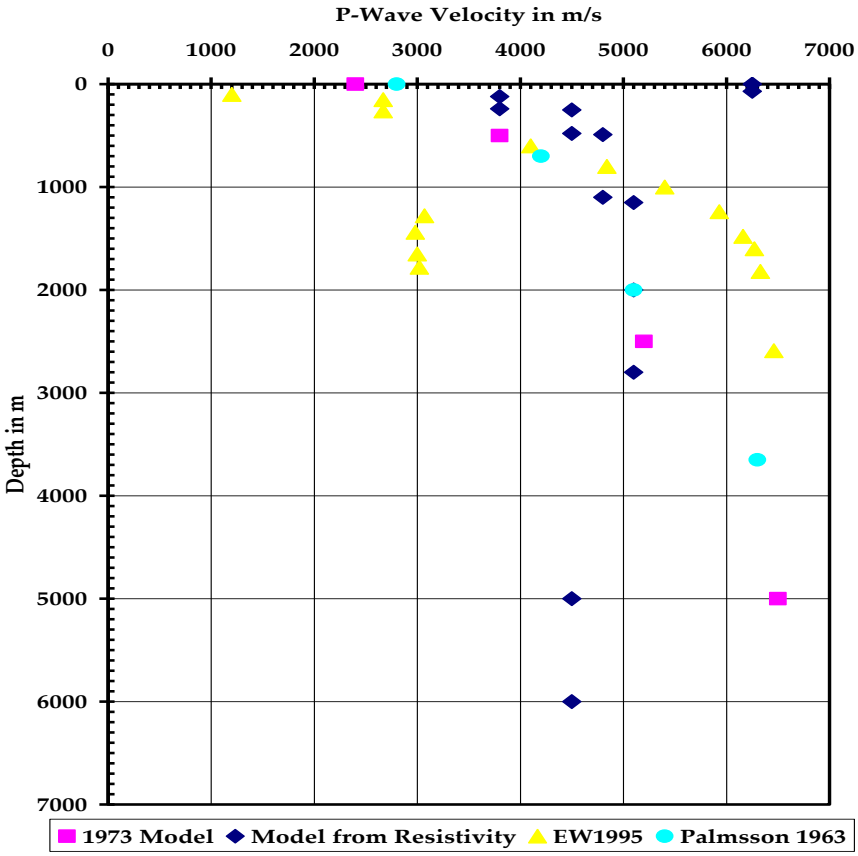

Figure 48: Plot of 1-D P-wave velocity models used in seismic studies at Krafla. The model generated from averaged resistivity values is shown in blue squares, while the model by Brandsdottir et al., (1997) is shown as yellow triangles. The resistivity generated model shows that P-wave velocity generally decreases with depth in areas with low resistivity interpreted as the heat source for the hydrothermal system.

Several P-wave velocity models have been used to determine the structure of the Krafla area. Plots of some of the models together with that generated from the resistivity from this study are very comparable within the depth range of 0-1,000m. One advantage of using the resistivity model is that it can give a better understanding of the deeper velocity model. The use of resistivity can also improve the 3-D model velocity structure. In particular the resistivity generated model indicates that the P-wave velocity decreases at a depth of more than 3,000m. Due to high resistivity near the surface, the P-wave generated model gives high velocity near the surface.

The resistivity generated P-Wave velocity model was used as the initial input in the location of microearthquakes taking into account the decrease in P-wave velocity with depth. The location of the earthquakes was plotted on resistivity maps and cross-sections to determine the spatial distribution of the earthquakes and their

relationship to the resistivity distribution. The results of the coincident interpretation of the earthquake and resistivity data are presented in the section below.

4.2 Joint interpretation of earthquake and resistivity measurements

The Krafla hydrothermal system shows a relatively higher level of seismicity than the hydrothermal systems at Longonot in Kenya and the Rhyolite Plateau area at Casa Diablo in California. This may be attributed to various factors including:

1. Proximity to a known active volcanic centre or tectonic region.
2. The effects of production of steam from geothermal wells coupled with injection of hydrothermal fluids.
3. The sensors were optimally located close to the source of earthquakes at Krafla. This is based on the comparison of the results from two deployments at Krafla in 2004 and 2005. In 2004, the sensors were located far away from the source of the earthquakes and as a consequence, very few earthquakes were recorded. This has the potential of an erroneous conclusion that the hydrothermal systems may be aseismic.
4. Seismic activity is periodic.

The majority of the earthquakes at Krafla generally occur at depths shallower than 3,000 m. The earthquakes have a NW-SE trend similar to that of the low resistivity (Figure 49). This trend cuts across the known tectonic structures of the rift zone which general are generally in the NS to NE-SW trend. The earthquakes occur at the boundary of low and high resistivity. Our analysis in this dissertation shows that very few earthquakes occur in the southern part of the Krafla hydrothermal system. This southern part of Krafla is also associated very high resistivity zone with a thickness of more than 4,000m. Our interpretation is that this indicates that either the heat source is very deep or few permeable fractures that transmit hydrothermal fluids.

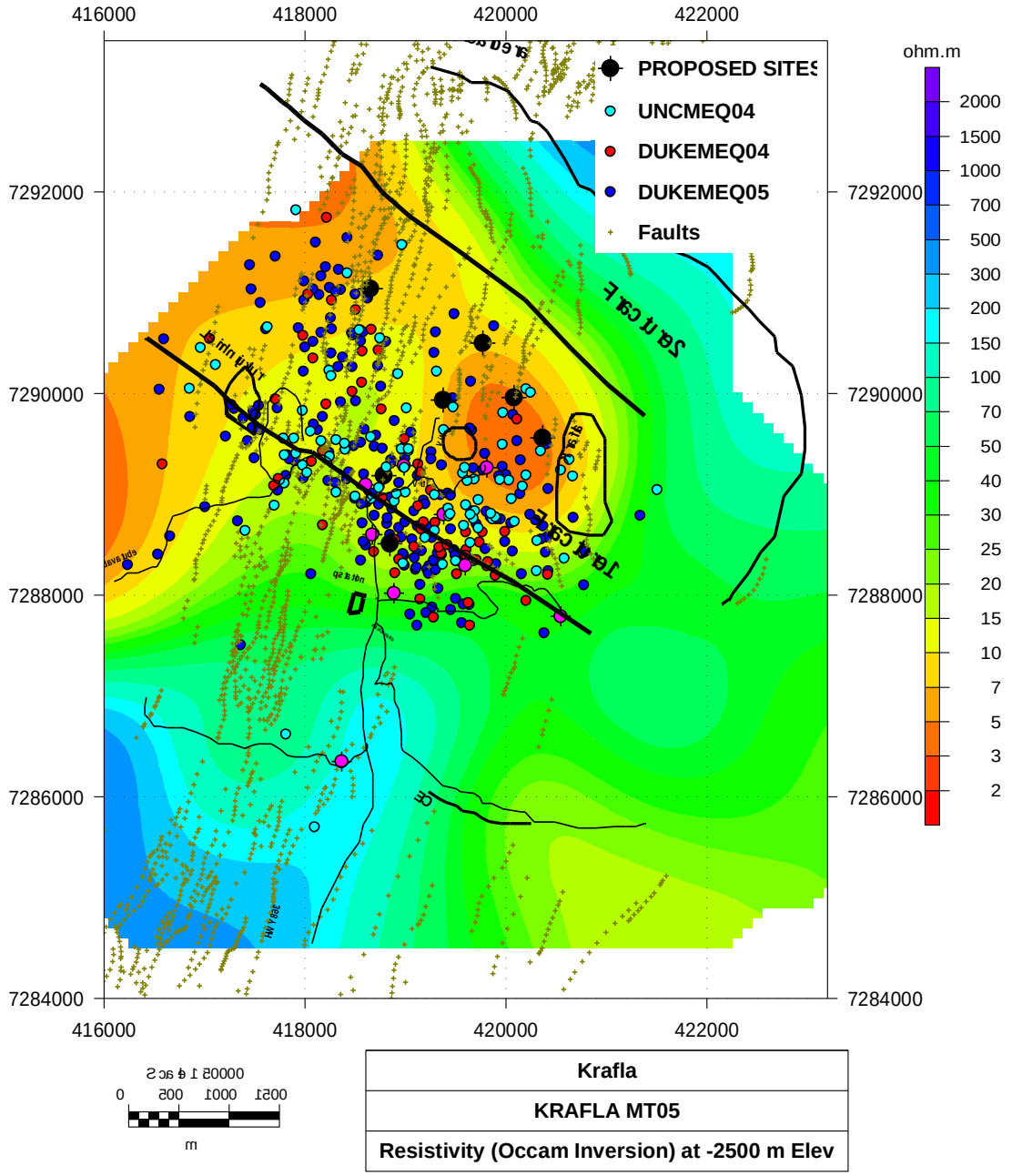

Figure 49: Plot of resistivity at a depth of 3,000m and the location of earthquakes. The earthquakes have a NW-SE similar to that of the low resistivity zone. The majority of the earthquakes seem to be located on the boundary between low and high resistivity.

As discussed in chapter 5 of this dissertation, the NW-SE trend might be related to the older shear zones that might still be active. These shear zones might therefore be important in channeling hot hydrothermal fluids from depths because of higher fracture permeability. Based on the analysis of the polarization directions, the NE-SW trending fractures are assumed to be shallower, and therefore might be important in controlling shallow ground water movement and lateral flow of hot hydrothermal fluids. This lateral flow might be mixed with shallow meteoric water to form good conditions for the alteration of the rocks to low temperature clays, which are very conductive. This altered layer is what forms the clay cap over the hydrothermal system.

The plot of 2-D resistivity along NE-SW trending profiles (Figures 50 and 51) that cut across the postulated fracture zone that formed by the NW-SE trending shear zones shows that earthquakes occur on the boundary of low and high resistivity. Nearly all the earthquakes that occur on the boundary of the low resistivity and high resistivity at depths show evidence of conversion of the S-wave to P-wave. The conversions were only recorded on four MEQ stations (K21, K34, K35 and K32) within the postulated fracture zone. These stations also showed the highest number of S-wave splitting events.

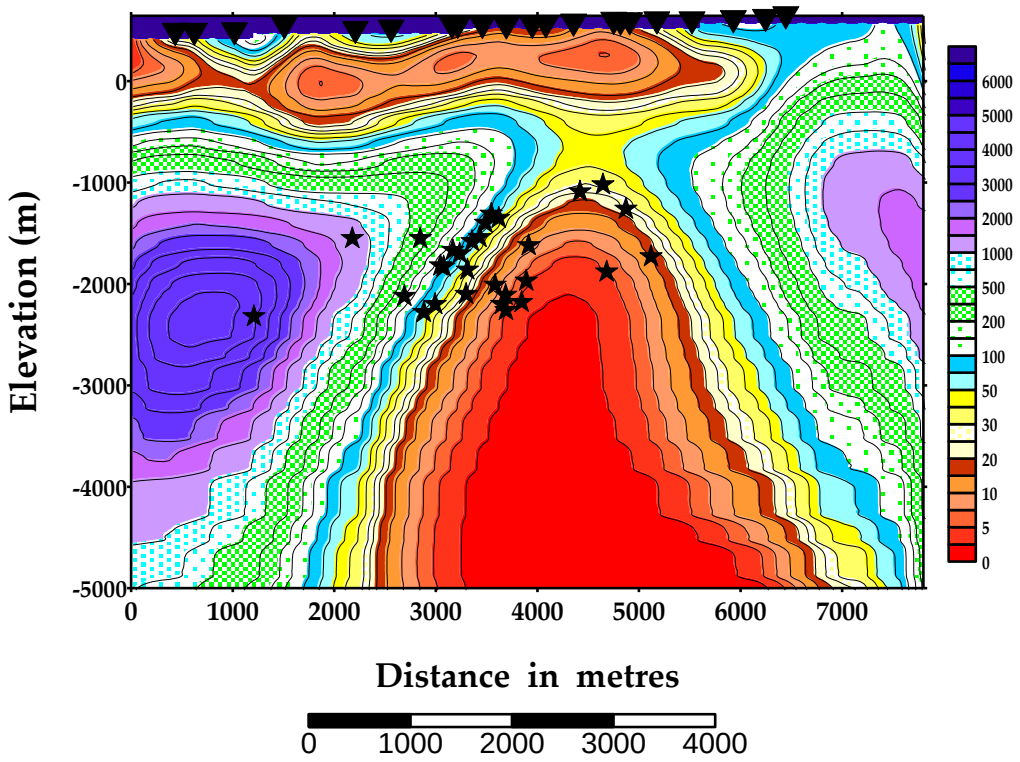

Figure 50: Plot of 2-D resistivity model for profile NE1 to the northern part of Krafla. The earthquakes occur on the boundary of the low and high resistivity above the interpreted heat source. The near surface low resistivity defines the cap rock.

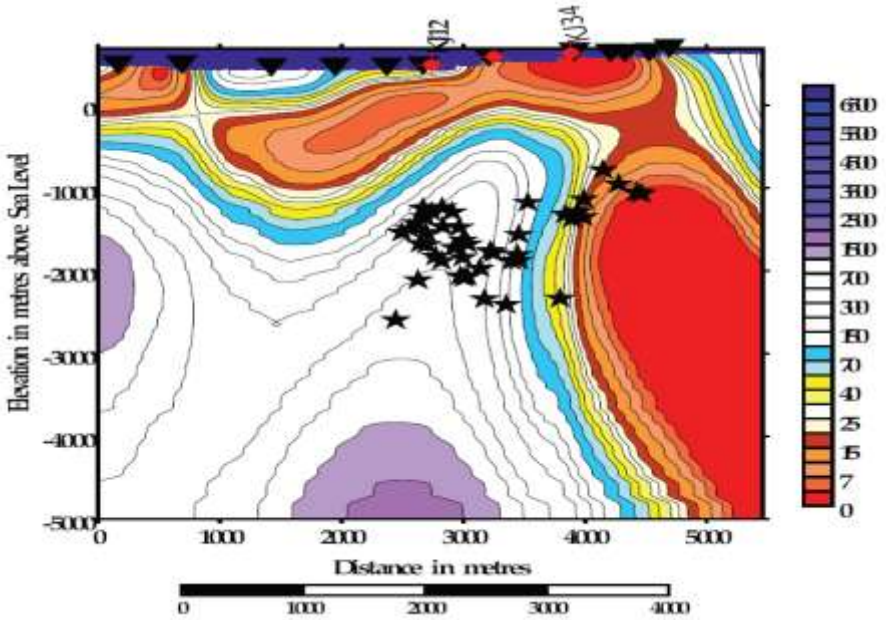

Figure 51: Plot of 2-D resistivity model for profile NE2 through the Krafla geothermal field. The earthquakes occur on the boundary of the low and high resistivity and below injection well KJ12.

The plot of resistivity and location of earthquakes across the Krafla geothermal field shows that earthquakes occur below the injection well KJ12 and well KJ34, which is the highest production well at Krafla. This implies that the earthquakes might be caused by injection of cooler hydrothermal fluids and production of steam for the Krafla power station. Injection in the deep Krafla reservoir, which is at a temperature of more than 250˚C, seems to induce earthquakes. This is probably due to stress related gradients that result from cooling of the geothermal reservoir (Mossop and Seagal, 1995). In this case, the seismic events cluster around the injection well, and seem to extent towards the low and high resistivity boundary that could be permeable. In the Krafla hydrothermal system, the low and high resistivity boundary is associated with a fracture. The pressure transients along the fracture can trigger some seismic activity. The cluster of shallower events around well KJ34 is probably associated with production from the well.

A plot of the existing temperature data from the wells along profile NE2, (Figure 52) shows that the near-surface low resistivity is associated with hydrothermal fluids at temperature of 200-260°C. The resistivity is consistent with alteration mineralogy patterns. Studies of alteration mineralogy have identified five alteration zones including a smectite-zeolite zone (<200°C) down to 210m depth, a mixed-layer clay zone (200-230°C) down to 420m depth, a chlorite zone (230-250°C) down to 820m, a chlorite-epidote zone (250-280°C) to a depth of about 1,000m. In most of the wells, the epidote-actinolite zone (>280°C) occurs below a depth of

1,000m. Measured temperatures in the lower part of the wells are roughly comparable with the alteration temperatures. This evidence indicates a stable high-temperature environment.

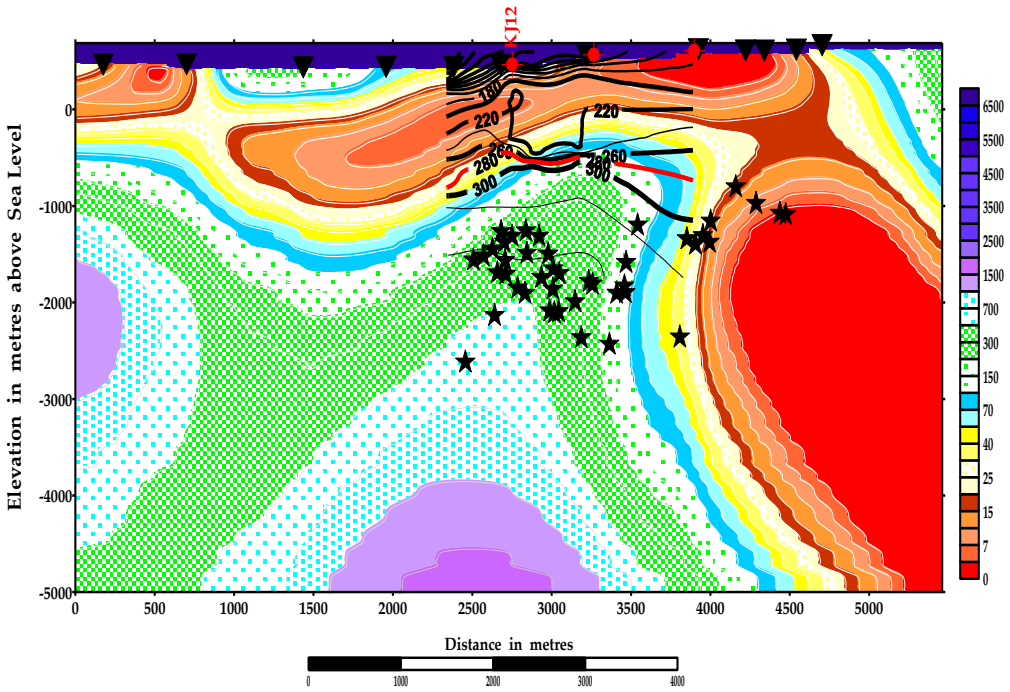

Figure 52: Plot of earthquakes and temperature along the NE2 resistivity section. The near surface low resistivity is associated with hydrothermal fluids at a temperature of 200-260°C. The resistivity below KJ12 is high probably indicating lower fracture porosity.

The temperature isotherms are of great importance to the conceptual understanding of reservoir structure and overall permeability. The high production from well KJ34 seems to suggest that the lower resistivity is probably due to high permeability while higher resistivity below the injection well is due to lower permeability. In this case, the natural state temperature pattern is the most reliable indicator of permeability in the Krafla geothermal reservoir. The most permeable areas are therefore expected be in the areas with lower resistivity and shallow earthquakes.

The plot of a 2-D NW-SE trending profile (NW1) together with the measured temperature in the wells (Figure 53) shows that the low resistivity zone is also associated with elevated temperatures.

This seems to confirm that the lower resistivity zones are associated with higher permeability than the high resistivity zones. Based on the correlation between temperature measurements and the MT resistivity model, it is reasonable to assume

that the low resistivity zones are associated with higher permeability. This forms the basis of generating porosity and P-wave velocity from the resistivity models.

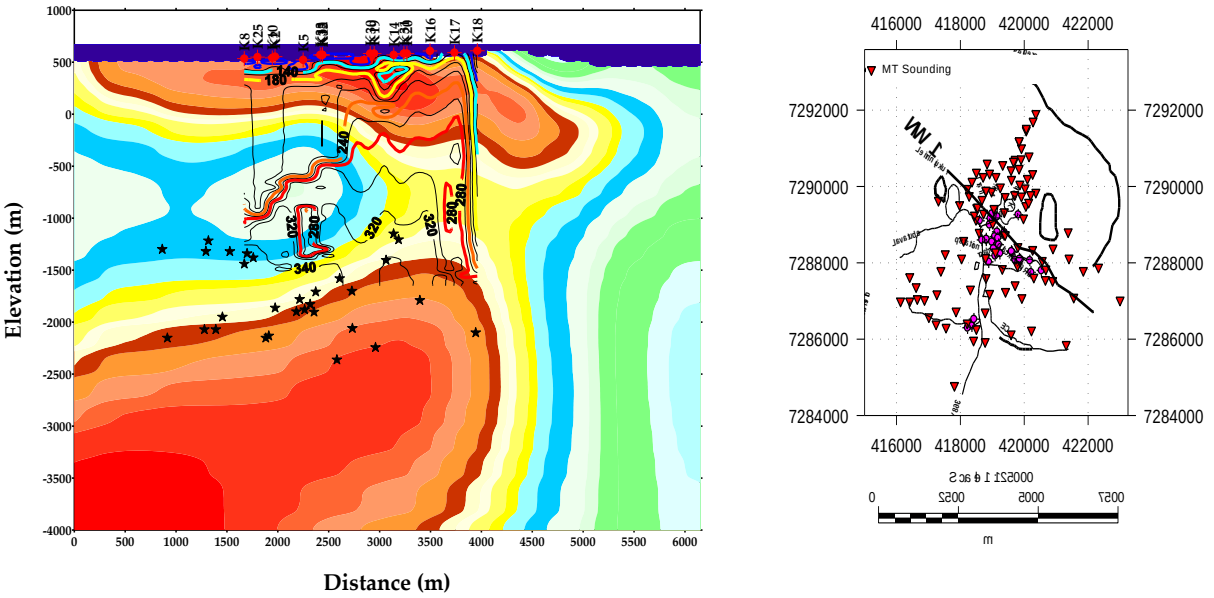

Figure 53: 2-D resistivity along profile NW1. Low resistivity zone is correlated to a zone of high temperature close to the surface. The sharp resistivity boundary at well KJ18 in the southeast is correlated with a zone of lower temperature. Earthquakes occur on the boundary of the deep low and high resistivity.

4.3 2-D porosity and P-wave velocity models generated from resistivity

This dissertation is focused on determining regions of high fracture permeability as targets for drilling high production wells. The imaging of fracture zones using MT and seismic methods provides complementary information that cannot be obtained by individual methods. The approach of joint inversion of seismic and electromagnetic data using a probability distribution function to determine porosity and reservoir gas saturation has recently been used to try to reduce the risk in petroleum gas reservoir exploration (Rubin G. Y., et al 2006). This method was applied to field measurements for a reservoir at 1400 mbsl. A joint inversion of EM and seismic data was carried out and the results improved the prediction for thin layers (20m at a depth of 1,544m) with gas saturation.

The approach in this dissertation is to define a porosity operator that relates both resistivity and p-wave velocity taking into account clay content, reservoir pore fluid resistivity, and temperature. The porosity operator was used together with the 2-D resistivity grid (see Figure 50) to generate porosity and P-wave velocity models. The

objective is to show that the porosity image (Figure 54) generated has the same structure as the resistivity model.

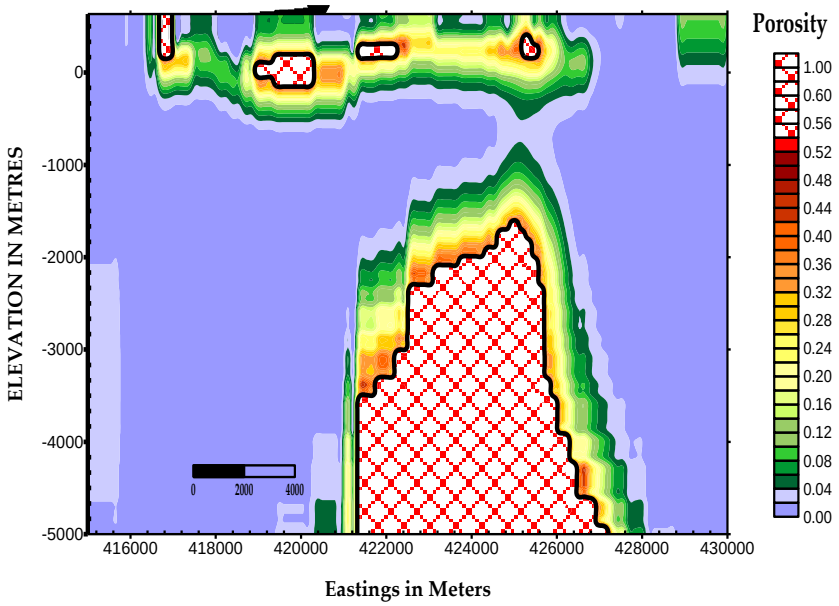

Figure 54: Porosity model generated from 2-D resistivity inversion model. The highest fracture porosity occurs within a narrow zone. The near surface high porosity corresponds to a region with low-temperature clays due to lateral movement of hydrothermal fluids. The low porosity corresponds to areas with high resistivity.

The areas with high resistivity show low porosity while areas with low resistivity show high porosity. We note that the values of porosity obtained have high errors (20%) because MT models have a better resolution of conductance rather than resistivity. The emphasis in this dissertation is on the contrasts rather than the obsolete values. Based on the porosity operator, although areas with resistivity less than 5 Ωm are shown as having high porosity, they only represent areas where the porosity operator is dependent of the high clay content and therefore not a reliable representation of the fracture model. In this case, the shallow areas with intermediate resistivity correspond to the clay cap. The deep low resistivity is associated with the interpreted partially molten heat source. The areas with very low resistivity therefore represent either regions with high clay alteration or high-temperature, partially molten rock. The good correlation between resistivity and temperature measurements shows that the deeper low resistivity zones are associated with high permeability and temperature. The porosity maps therefore give an indication of areas that could be targets for drilling high production wells. The P-wave velocity image (Figure 55) has the same structure as the resistivity model (see Figure 50). The areas with high resistivity show high P-wave velocity while areas with low resistivity show low P-wave velocity.

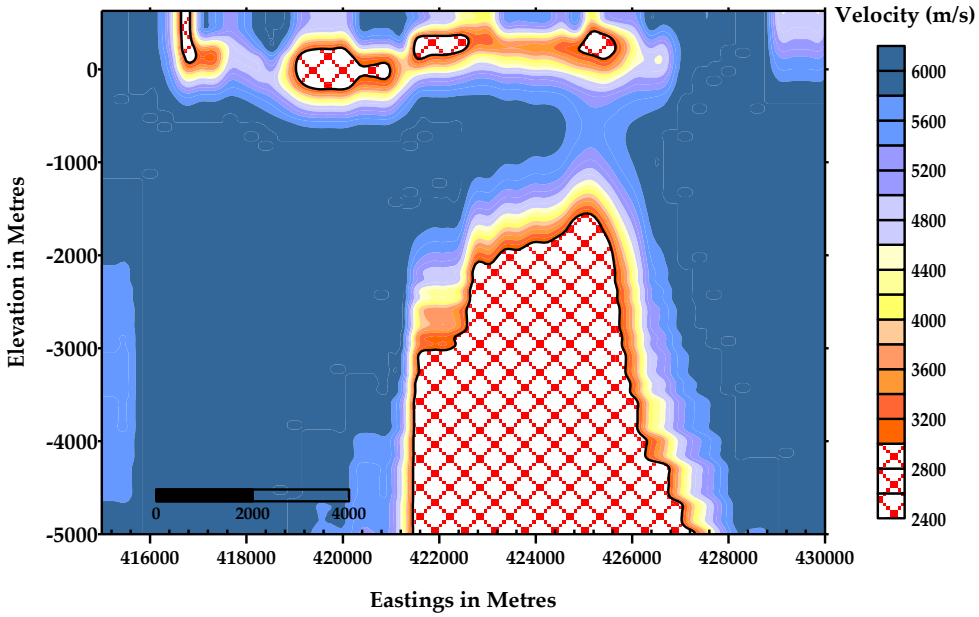

Figure 55: P-wave velocity model generated from 2-D resistivity inversion model. The lowest P-wave velocity occurs within a narrow area interpreted as a fracture zone. The near surface P-wave resistivity corresponds to a region with low-temperature clays due to lateral movement of hydrothermal fluids. The high P-wave velocity corresponds to areas with high resistivity and low porosity.

The areas with low P-wave velocity and low resistivity less than 5 Ωm are interpreted as regions with either high clay alteration or high-temperature partially molten rock interpreted as the heat source for the hydrothermal system. Evidence for the interpretation of a heat source is given by the postulated conversions of S-, to P-waves at the interface of the deep low resistivity zone.

4.4 Evidence of conversion of S-waves to P-waves

In this dissertation we assume and conclude that the S-wave splitting occurs at shallow depths mainly influenced by NE-SW and NW-SW trending fluid filled fractures. Geological and structural evidence from the existing geothermal wells shows that rock formations at shallow depths consist mainly of basaltic hyaloclastite formations and basaltic lava series. Intrusive rocks of basalt/dolerite composition occur below 530m depth and predominate from 990m down to the bottom of the well. Aquifers were confirmed at 100-155, 275, 600, 680, 730, 800 and 930m depth, mostly related to intrusion contacts and fractures.

The evidence for the interpretation of deep low resistivity as a heat source is based on the phases on some of the earthquakes, which show a reflection of the P-wave and conversion of the S-wave to a P-wave that arrives before the S-wave (Figure 56). The conversion of the S- to P-wave is postulated to occur at the top of the low

resistivity zone that is interpreted as a semi-molten heat source for the hydrothermal system. However, due to the limited number of stations that show these types of earthquakes, the data is not sufficient for a tomographic inversion.

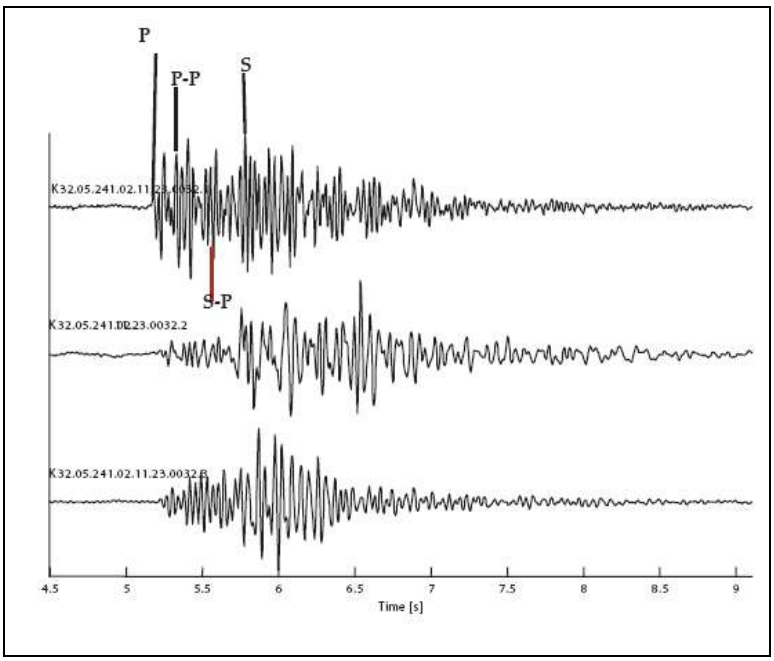

Figure 56: An example of a reflected P-P and converted S-P waves for earthquakes that are located above the heat source and recorded by K32 station located above the hypocenter of most of the earthquakes on the boundary of high and low resistivity.

Based on the conceptual model that a heat source occurs below the hydrothermal reservoir and the interpretation that the heat source is associated with low resistivity and lower P-wave velocity, it is expected that some reflections would occur for the earthquakes that have their origin above the heat source. Analysis of the earthquakes recorded during the field campaign in 2005, shows that some stations have clear large amplitude signals between the P-wave and S-wave arrivals. In this dissertation, we use the occurrence of these signals that show possible conversions of S-waves to P-waves as evidence that the deeper low resistivity might be partially molten rock. Stroujkova and Malin (2000, 2001 and 2002) used the methods of first-order scattering and stacking to find the likely location and shape of the reflecting zone on microearthquake clusters in the Mammoth Lakes. Based on the particle motions, it was postulated that the reflections were either from the transition of solid to partially molten rock or the transition from dry rock to fluid saturation. In this dissertation, we assume that the reflections are from the top of molten rock mixed with hydrothermal fluids. Similar reflectors have been found both in volcanic and rift zones (Ake and Sanford, 1988; Sanford et al., 1973).

5. Discussions, recommended sites for drilling, future work, summary and conclusions

5.1 Discussions

The results of this dissertation indicate that both MEQ and MT stations can be used jointly to map fluid-filled fracture zones in hydrothermal systems. Two systems of fractures have been identified from the MEQ and MT studies. The EW to WNW trending structures in the Krafla hydrothermal system seem to be at an oblique angle to the NW trending regional faults and lineaments (Figure 57).

The NW-SE trending faults and lineaments are also associated with earthquakes that have a NW-SE trend similar to those recorded at the Krafla hydrothermal system. This seems to suggest that the NW-SE trending fracture zones mapped by the interpretation of resistivity and earthquake data are active and might form important channels for upwelling of hydrothermal fluids. The hydrothermal system seems to occur at the intersection of the older NW-SE trending faults and younger NE-SW trending dykes and fissures swarms (Figure 57).

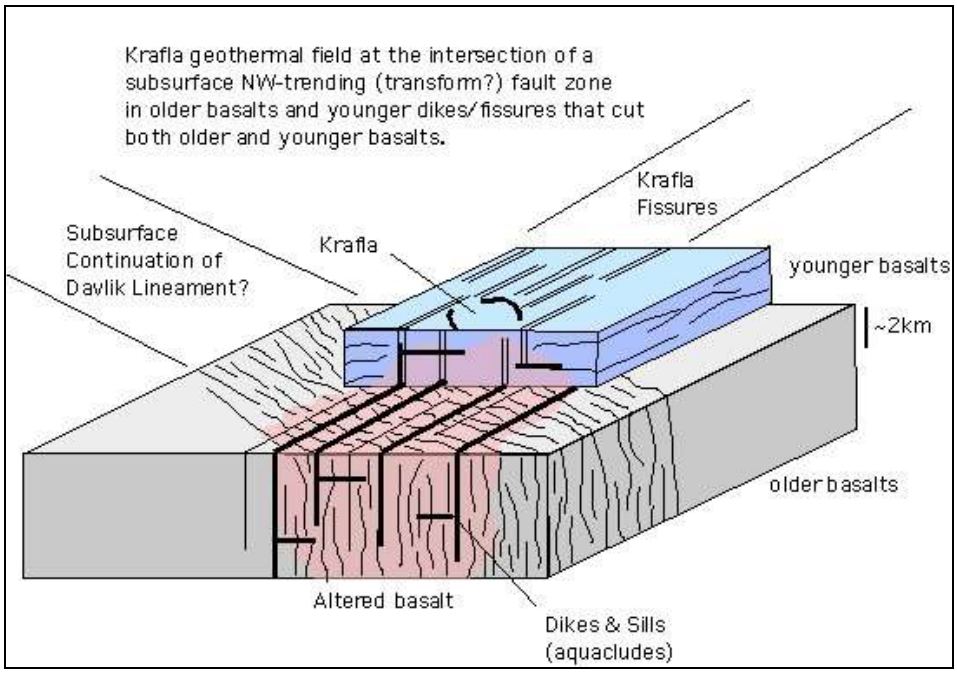

Structural map showing that the Krafla hydrothermal system possibly occurs at the intersection of subsurface NW-SE trending faults. The NW-SE also occurs in older rocks and younger fissure swarms. The fissures are associated with dyke swarms that control lateral movement of hydrothermal fluids.

The NW-SE trending faults occur within older rocks which are buried by younger rocks. It is possible that some of these NW-SE trending faults have been reactivated by recent tectonic movements, and as such they may be zones of active hydrothermal fluid circulation close to the surface. The circulation of hydrothermal fluids close to the surface determines the alteration patterns in the hydrothermal system, the MT strike direction, and the S-wave splitting. The circulation of the hydrothermal fluids might alter the rocks, therefore lowering the resistivity within the fracture zones. The occurrence of dykes and sills in the hydrothermal systems may form aquacludes by limiting both lateral and vertical flow of hydrothermal fluids.

Based on this structural and geological interpretation of the observed resistivity and seismic data, intersections of the faults and fractures are postulated to form important channels for the upwelling of hydrothermal fluids. The fracture distribution at the intersection of the faults is probably dependent on the stress field on the fault traces. The stress field is postulated to result in either extension of blocks or compression (Figure 58).

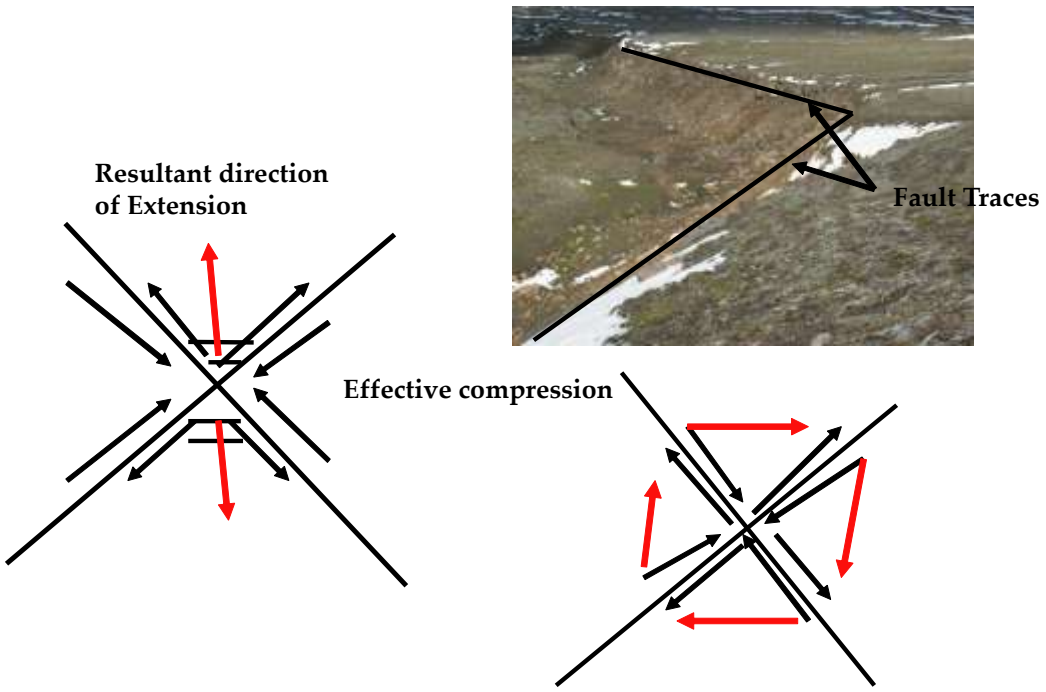

Figure 57: Postulated extension and compression of blocks at intersection of faults. The extension mechanism at the intersections of the faults may produce zones of enhanced permeability while the zones of compression may produce little variation in permeability from that of the host rocks.

The best target areas for enhanced fracture porosity would be expected to be at the regions with effective extension at the intersections of the faults. The region of effective compression would generally produce very low fracture porosity.

5.2 Recommended Sites for drilling

Based on the joint interpretation of seismic and electrical resistivity data, drilling targets for high production wells should be in the areas with both S-wave and MT splitting, well defined fracture orientations and well defined low resistivity at depth that is the heat source. The best targets should within the interpreted fracture zone (Figure 59) on the boundary of the deep low resistivity (Figure 60).

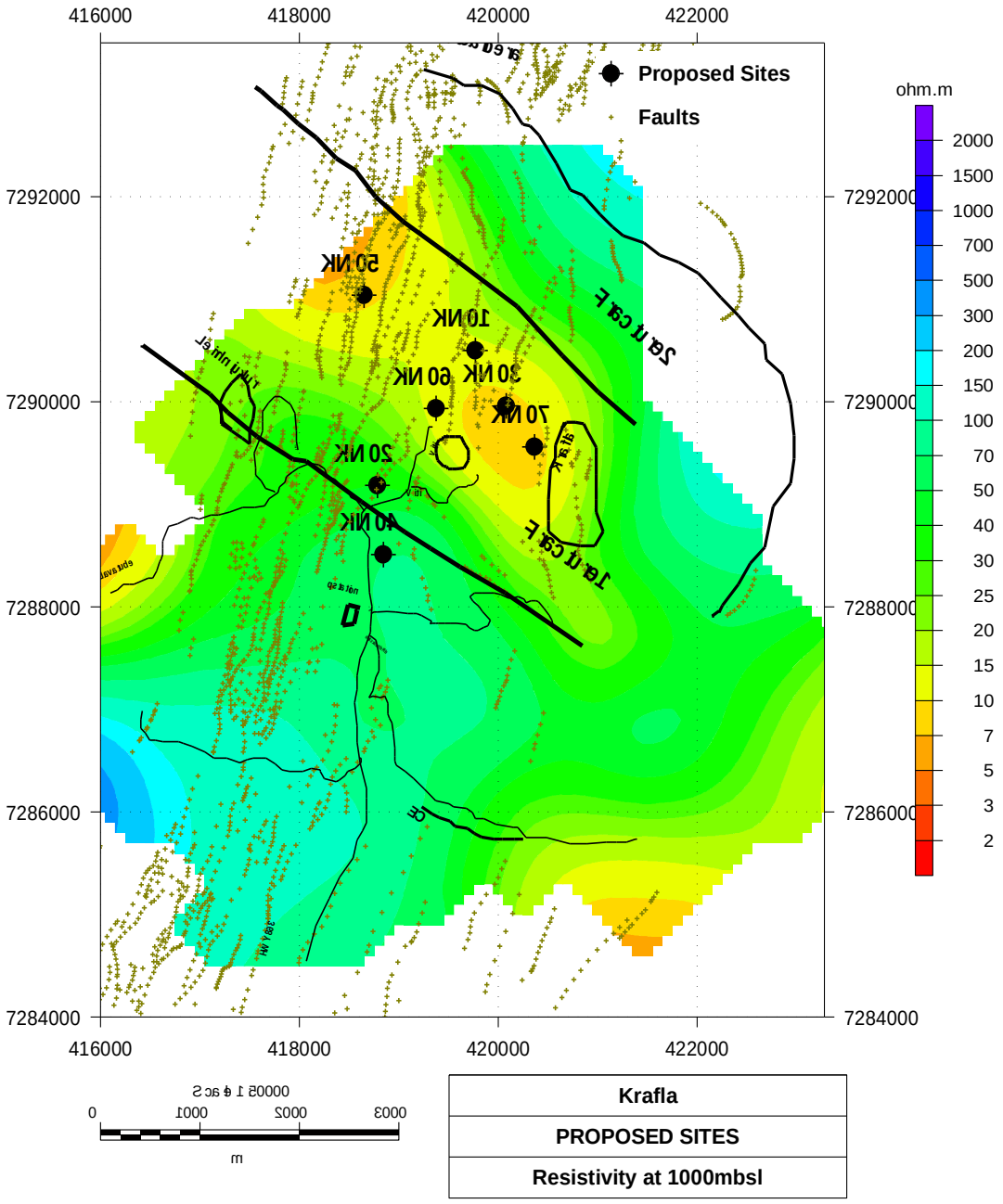

Figure 58: Recommended sites for drilling. The sites can be used as pads for directional drilling to for high production wells.

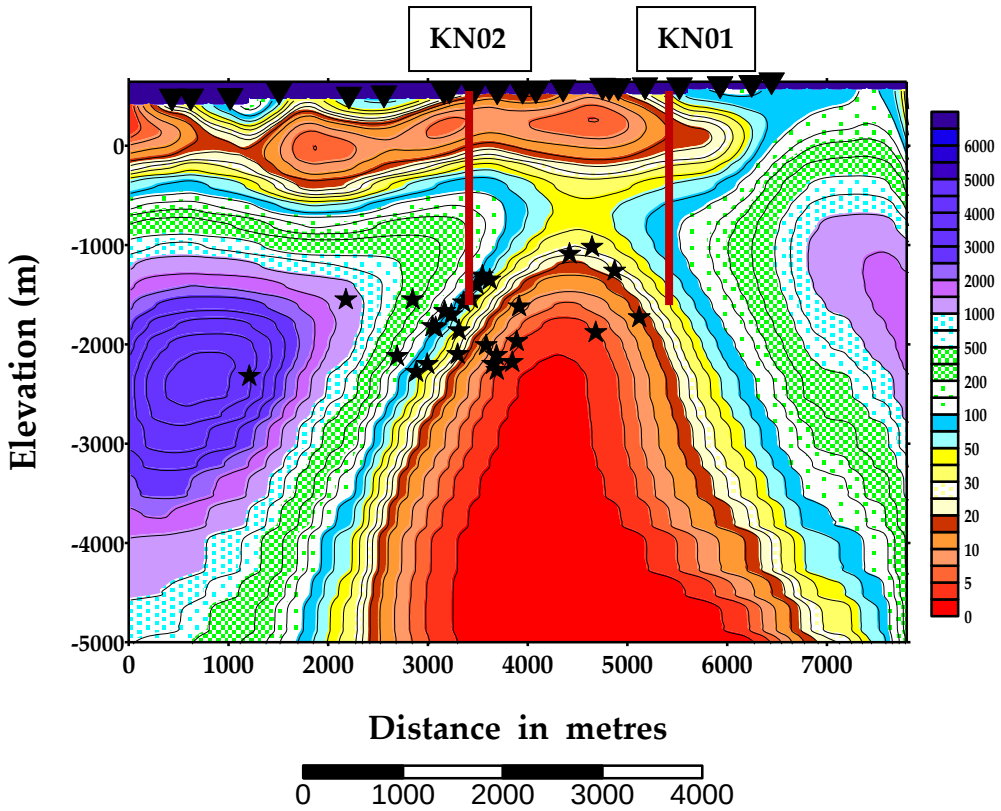

Figure 59: 2-D resistivity section showing the targets for drilling within the interpreted fracture zone.

The description of the sites and justification is given below:

KN01

This site has been given priority to explore the northern part of Krafla for the planned 40 MWe expansion. The target depth should between 2, 000- 2,500m. This site can be used for deviated wells to the west, east, south and north. The target directions should be such that they intercept the NW and NE trending structures.

KN02

This site has been given second priority to explore the fracture NW-SE trending fracture zone. A deviate well could be made to target the intersection of the NW and NE trending structures. The final number of wells to drill from this site would depend on the chemistry of the reservoir fluids. The target depth should between 2, 000- 2,500m.

KN03

This is a step out site for KN01. It can also be used for directional drilling to intercept the fractures and the intersections of the NW and NE trending structures.

KN04

This site is recommended for deep drilling to target the deeper low resistivity. This can be one of the sites for drilling for super critical steam. It could also be an experimental site for the benefits of drilling deeper with the existing field.

KN05

This site is recommended for investigating the low resistivity to the north east of Leirhnjukur. This is an area for potential expansion if the necessary permits are acquired.

KN06

This site is recommended for investigating the centre of the interpreted fracture zone.

KN07

This site is recommended for investigating the northern part of the high production well number 34.

5.3 Future work

Future work will mainly focus on carrying out joint inversion and 3-D tomography of MEQ and MT data to map fracture zones in hydrothermal system. The two approaches suggested are:

1. Joint tomographic modeling of fluid-filled fractures in hydrothermal systems based on the evidence of correlation between MT and S-wave anisotropy. This approach will be used to determine fracture density, orientation and depth.
2. Joint inversion of MEQ and MT data based on the porosity operator developed in this thesis. This will be useful in determining areas with high fracture porosity that can be targets for drilling high production geothermal wells.
3. Joint inversion of the S- to P-wave conversions to determine the depth to the postulated heat sources in the hydrothermal systems.

5.4 Summary and conclusions

This dissertation presents a method of using earthquakes and resistivity data to characterize permeable hydrothermal reservoirs. The field examples from Casa Diablo in the Long Valley Caldera, California, Mt. Longonot, Kenya, and Krafla, Iceland show that it is possible to map fracture zones that can be targets for high production geothermal wells. One of the major finding of this study is that successful use of MEQ shear wave tomography for geothermal exploration can be unreliable if the target area is not seismically active, even if the array is designed to detect low magnitude microearthquakes.

This study has demonstrated that joint interpretation of P- and S-wave velocity, S-wave polarization and splitting magnitude, resistivity, and magnetotelluric (MT) strike directions can successfully be used to determine fracture-porosity and orientation. The method has been tested with field earthquake and resistivity data,

core samples, temperature measurements, and for the case of Krafla, with a drilled well. The summary of the results is given below:

- Strong evidence exists for correlation between both the polarization and anisotropy in the MT and MEQ S-wave splitting data at sites close to fluid-filled fracture zones.
- A high density of fluid-filled fractures bound by less fractured host rocks exists at the Krafla.
- Microearthquakes are located on the boundary between low resistivity and high resistivity.
- Resistivity is lowest within the core of the fracture zone and partially molten magma chamber.
- Resistivity can be used to generate P-wave velocity independent from that generated by ray tracing.
- Fracture porosity imaged by the resistivity double porosity modeling varies between 5-45%. A porosity operator generated from a double porosity model has been used to generate valid P-wave velocity models from resistivity data. This approach is being developed further into a joint inversion scheme.
- Inappropriate deployment of MEQ can lead to the wrong conclusion that hydrothermal systems are not seismically active.

References

Ake, J., and Sanford, A (1988). New evidence for the existence and internal structure of a thin layer of magma at mid-crustal depths near Socorro, New Mexico. Bull. Seis. Soc. Am., 78, 1335-1359.

Armannsson, H., Gudmundsson, A., and Steingrimsson, B. (1987). Exploration and development of the Krafla geothermal area. Jokull, 37, 13-30.

Arnason, K. (1989). Central loop transient electromagnetic sounding over a horizontally layered earth (No. OS-89032/JHD-06). Reykjavik: Orkustofnun.

Arnason, K. (2006). A Programme for 1-D inversion of central loop TEM and MT data. In S., O. (Ed.) (pp. 9). Reykjavik: ISOR, Iceland Geosurvey.

Arnason, K., and Karlsdottir, R. (1976). A TEM resistivity survey of the Krafla high-temperature field. (In Icelandic with English abstract). Rekjavik: Orkustofnun.

Arnasson, A., Ragna, K., Hjalmar, E., Flovenz, O., and Steiner G. (2000). The resistivity structure of high temperature geothermal systems in Iceland. Proceedings of the world geothermal congress, Kyushu Japan, 923-928.

Berdichevsky, M. N., & Dmitriev, V. I. (2004). Inverse problems of magnetotellurics: A modern formulation. Izvestiya-Physics of the Solid Earth, 40(4), 276-292.

Berdichevsky, M. N., Dmitriev, V. I., Golubtsova, N. S., Mershchikova, N. A., & Pushkarev, P. Y. (2003). Magnetovariational sounding: New possibilities. Izvestiya-Physics of the Solid Earth, 39(9), 701-727.

Berdichevsky, M. N., Dmitriev, V. I., & Pozdnjakova, E. E. (1998). On two-dimensional interpretation of magnetotelluric soundings. Geophysical Journal International, 133(3), 585-606.

Berdichevsky, M. N., Vanyan, L. L., & Dmitriev, V. I. (1989). Methods Used in the Ussr to Reduce near-Surface In homogeneity Effects on Deep Magnetotelluric Sounding. Physics of the Earth and Planetary Interiors, 53(3-4), 194-206.

Bjornsson, A. (1985). Dynamics of Crustal Rifting in Ne Iceland. Journal of Geophysical Research-Solid Earth and Planets, 90(NB12), 151-162.

Bjornsson, A., Eysteinsson, H., and Beblo, M. (2005). Crustal formation and magma genesis beneath Iceland: Magnetotelluric constraints. Geological Society of America Special Publications, 388, 665-686.

Block, D. (2001). Water Resistivity Atlas of Western Canada. , Rock Foundation Convention of the Canadian Society of Petroleum Geologists. Calgary, Canada.

Brandsdottir, B., Menke, W., Einarsson, P., White, R., and Staples, R. (1995). Crustal structure of the Krafla central volcano in the northern volcanic zone of Iceland as determined through seismic observations. Reykjavik: Science Institute, University of Iceland.

Christensen, N., and Wilkens, R. (1982). Seismic properties, density, and composition of the Icelandic crust near Reydarfjordur. J. Geophys.Res., 87, 6389-6395.

Crampin, S. (1985). Evaluation of Anisotropy by Shear-Wave Splitting. Geophysics, 50(1), 142-152.

Crampin, S. (1994a). Crack Models for a Transversely Isotropic Medium - Comment. Journal of Geophysical Research-Solid Earth, 99(B6), 11749-11751.

Crampin, S. (1994b). The Fracture Criticality of Crustal Rocks. Geophysical Journal International, 118(2), 428-438.

Crampin, S. (1994c). Partial-Wave Summations in Atomic-Sphere Surface Calculations. Physical Review B, 49(19), 14035-14038.

Crampin, S., & Peacock, S. (2003). Seismic evidence for fluid-driven deformation. Journal of Geodynamics, 36(1-2), 67-77.

Crampin, S., & Peacock, S. (2005). A review of shear-wave splitting in the compliant crack-critical anisotropic Earth. Wave Motion, 41(1), 59-77.

Crampin, S., Peacock, S., Gao, Y., & Chastin, S. (2004). The scatter of time-delays in shear-wave splitting above small earthquakes. Geophysical Journal International, 156(1), 39-44.

Cumming, W., Nordquist, G., and Astra, D.,. (2000). Geophysical exploration for geothermal resources: An application for combined MT-TDEM. 70th Ann. Internat. Mtg: Soc. of Expl. Geophys, 1071-1074.

Einarsson, P. (1978). S-wave shadows in the Krafla caldera in NE Iceland, evidence for a magma chamber in the crust. Bull. Volcanol., 43, 1-9.

Einarsson, P., and Brandsdottir, B. (1980). Seismological evidence for lateral magma intrusion during the July 1978 deflation of the Krafla volcano in NE-Iceland. J. Geophys., 47, 211-220.

Elkibbi, M., & Rial, J. A. (2005). The Geysers geothermal field: results from shear-wave splitting analysis in a fractured reservoir. Geophysical Journal International, 162(3), 1024-1035.

Elkibbi, M., Yang, M., & Rial, J. A. (2005). Crack-induced anisotropy models in The Geysers geothermal field. Geophysical Journal International, 162(3), 1036-1048.

Evans, J., Forster C., and Goddard, J. (1997). Permeability of fault-related rocks, and implications for hydraulic structure of fault zones. J. Struct. Geol., 19, 1393-1404.

Flovenz, O., and Karlsdottir, R. (2000). TEM-Resistivity image of a geothermal field in N-Iceland and relation of the resistivity with lithology and temperature. Paper presented at the World Geothermal Congress, Kyushu, Japan.

Flovenz, O., Spangenberg, E., Kulenkampff, J., Arnason, K., Karlsdottir, R., and Huenges, E. (2005). The role of Electrical conduction in geothermal exploration. Paper presented at the World Geothermal Congress, Antalya, Turkey.

Flovenz, O. G. (1985). Application of Subsurface Temperature-Measurements in Geothermal Prospecting in Iceland. Journal of Geodynamics, 4(1-4), 331-340.

Flovenz, O. G., Georgsson, L. S., & Arnason, K. (1985). Resistivity Structure of the Upper Crust in Iceland. Journal of Geophysical Research-Solid Earth and Planets, 90(NB12), 136-150.

Groom, R. W., & Bailey, R. C. (1991). Analytic Investigations of the Effects of near-Surface 3-Dimensional Galvanic Scatterers on Mt Tensor Decompositions. Geophysics, 56(4), 496-518.

Gudmundsson, A. (2001a). An expansion of the Krafla power plant from 30 to 60 MWe Paper presented at the Geothermal Resources Council Transactions.

Gudmundsson, A. (2001b). Fluid overpressure and flow in fault zones: field measurements and models. Tectonophysics, 336(1-4), 183-197.

Gudmundsson, A., Berg, S. S., Lyslo, K. B., & Skurtveit, E. (2001). Fracture networks and fluid transport in active fault zones. Journal of Structural Geology, 23(2-3), 343-353.

Gudmundsson, A., & Brenner, S. L. (2001). How hydrofractures become arrested. Terra Nova, 13(6), 456-462.

Gudmundsson, A., Fjeldskaar, I., and Brenner, S. (2002). Propagation pathways and fluid transport of hydrofractures in jointed and layered rocks in geothermal fields. Journal of Volcanology and Geothermal Research, 116(3-4), 257-278.

Haber, E., & Oldenburg, D. (1997). Joint inversion: A structural approach. Inverse Problems, 13(1), 63-77.

Heise, W., & Pous, J. (2001). Effects of anisotropy on the two-dimensional inversion procedure. Geophysical Journal International, 147(3), 610-621.

Hudson, J. (1980). Overall properties of a cracked solid. Math. Proc. Camb. Phil. Soc., 88, 371-384.

Hudson J. (1981). Wave speeds and attenuation of elastic waves in material containing cracks. Geophysical Journal of Royal Astronomical Society., 64, 133-150.

Ingham, M. (2005). High resolution electrical imaging of fault zones. Physics of the Earth and Planetary Interiors, 150(1-3), 93-105.

Jonasson, K. (1994). Rhyolite volcanism in the Krafla central volcano, north-east Iceland. Bulletin Volcanol, 56, 516-528.

Klein, F. (2002). User's guide to Hypoinverse-2000, a Fortran program to solve for earthquake locations and magnitudes: United States Geological Survey.

Kozlovskaya, E. (2001). Theory and application of joint interpretation of multi-method geophysical data. Unpublished Academic Dissertation, University of Oulu, Linnanmaa, Finland.

Kozlovskaya, E. G., Karatayev, G. I., & Yliniemi, J. (2001). Lithosphere structure along the northern part of EUROBRIDGE in Lithuania; results from integrated interpretation of DSS and gravity data. Tectonophysics, 339(1-2), 177-191.

Lachenbruch, A. H., and Sass, J.H.,. (1978). An expanding lithosphere and heat flow in the Basin and Range province. Geol. Soc. Amer. Mem, 152, 209.

Maultzsch S., C., E., Liu, E., and Li, Y. X.,. (2003). Modeling frequency-dependent seismic anisotropy in fluid-saturated rock aligned fractures: implication of fracture size estimation from anisotropic measurements. Geophysical Prospecting, 51, 381-392.

Menke, W., West, M., Brandsdottir, B., & Sparks, D. (1998). Compressional and shear velocity structure of the lithosphere in northern Iceland. Bulletin of the Seismological Society of America, 88(6), 1561-1571.

Mossop, A., and Segall, P. (1995). Induced seismicity and The Geysers, Northern California, Eos proceedings of the Amer. Geophysics Union, 444.

O'Connell, R. J., and Budiansky, B. (1974). Seismic velocities in dried and cracked solids. Journal of Geophysical Research, 79, 5412-5426.

Pellerin, L., & Hohmann, G. W. (1990). Transient Electromagnetic Inversion - a Remedy for Magnetotelluric Static Shifts. Geophysics, 55(9), 1242-1250.

Pellerin, L., & Hohmann, G. W. (1995). A Parametric Study of the Vertical Electric Source. Geophysics, 60(1), 43-52.

Pellerin, L., Johnston, J. M., & Hohmann, G. W. (1996). A numerical evaluation of electromagnetic methods in geothermal exploration. Geophysics, 61(1), 121-130.

Ranganayaki, R. (1984). An interpretative analysis of magnetotelluric data. Geophsics, 49, 1730-1748.

Rial, J. A., Elkibbi, M., & Yang, M. (2005). Shear-wave splitting as a tool for the characterization of geothermal fractured reservoirs: lessons learned. Geothermic, 34(3), 365-385.

Rodi, W., & Mackie, R. L. (2001). Nonlinear conjugate gradients algorithm for 2-D magnetotelluric inversion. Geophysics, 66(1), 174-187.

Rubin, Y., Hoversten, M., Hou, Z., and Chen, J. (2006). Risk reduction in gas reservoir exploration using joint seismic-EM inversion. GasTips, 12(1), 5-9.

Saemundsson, K. (1974). Evolution of the axial rifting zone in Northern Iceland and the Tjornes fracture zone. . Geol. Soc. Amer. Bull, 85, 495-504.

Saemundsson, K. (1978). Fissure swarms and central volcanoes of the neovolcanic zones of Iceland. Geol. Jour. , 10(Spec Issue), 415-432.

Saemundsson, K. (1981). The Krafla geothermal field, north-east Iceland. In L. Rybach and In Geothermal Systems (pp. 272-294): Wiley, New York, N.Y.

Sigurdsson, O., Gudmundsson, A., Fridleifsson, O., Franzson, H., Gudlaugsson, S., and Stefansson, V. (2000, May 28-June 10). Database of igneous rock properties in Icelandic geothermal systems: Status and unexpected results. Paper presented at the World Geothermal Congress, Kyushu-Tohuku, Japan.

Simpson, F., and Bahr, K. (2005). Practical Magnetotellurics. Cambridge University press

Spies, B. R. (1989). Depth of Investigation in Electromagnetic Sounding Methods. Geophysics, 54(7), 872-888.

Spies, B. R., & Eggers, D. E. (1986). The Use and Misuse of Apparent Resistivity in Electromagnetic Methods. Geophysics, 51(7), 1462-1471.

Spies, B. R., & Parker, P. D. (1984). Limitations of Large-Loop Transient Electromagnetic Surveys in Conductive Terrains. Geophysics, 49(7), 902-912.

Stefansson, V., and Steingrimsson, B. (1980). Production of wells tapping two-phase reservoirs at Krafla and Namafjall. Paper presented at the 6th Workshop on Geothermal Reservoir Engineering, Stanford.

Stefansson, V., Axelsson, G., and Sigurdsson, O. (1982). Resistivity logging of fractured basalt. Paper presented at the Eighth Workshop of Geothermal Reservoir Engineering, Stanford University, California.

Stroujkova, A., & Malin, P. (2001). Multiple ruptures for Long Valley microearthquakes: a link to volcanic tremor? Journal of Volcanology and Geothermal Research, 106(1-2), 123-143.

Stroujkova, A., & Malin, P. E. (2002). Moment-tensor statistics of the 1997 Long Valley microearthquake swarm. Journal of Seismology, 6(1), 69-85.

Stroujkova, A. F., & Malin, P. E. (2000). A magma mass beneath Casa Diablo? Further evidence from reflected seismic waves. Bulletin of the Seismological Society of America, 90(2), 500-511.

Ussher, G., Harvey, C., Johnstone, R., and Anderson, E (2000, May 28- June 10). Understanding the resistivity observed in geothermal systems. Paper presented at the World Geothermal Congress, Kyushu-Tohoku, Japan.

Wannamaker, P. E. (1999). Affordable magnetotelluric interpretation in natural environments. Society of Exploration Geophysicist, 274.

Wannamaker, P. (2005). Anisotropy versus heterogeneity in continental solid earth electromagnetic studies: Fundamental response characteristics and implications for physicochemical state. Surveys in Geophysics, 26: 733-765

Ward, P., and Bjornsson S. (1971). Microearthquakes swarms, and the geothermal areas of Iceland. J. Geophys. Res., 76, 3953-3982.

Wyllie, R., Gregory, A., and Gardner, G. (1958). An experimental investigation of factors affecting elastic wave velocities in porous media. Geophysics, 23, 459-493.

EXAMPLE OF A GEOTHERMAL FIELD

BOREHOLE SEISMIC NETWORK & DRILL TARGETING REPORT

By

IESE - SONDI

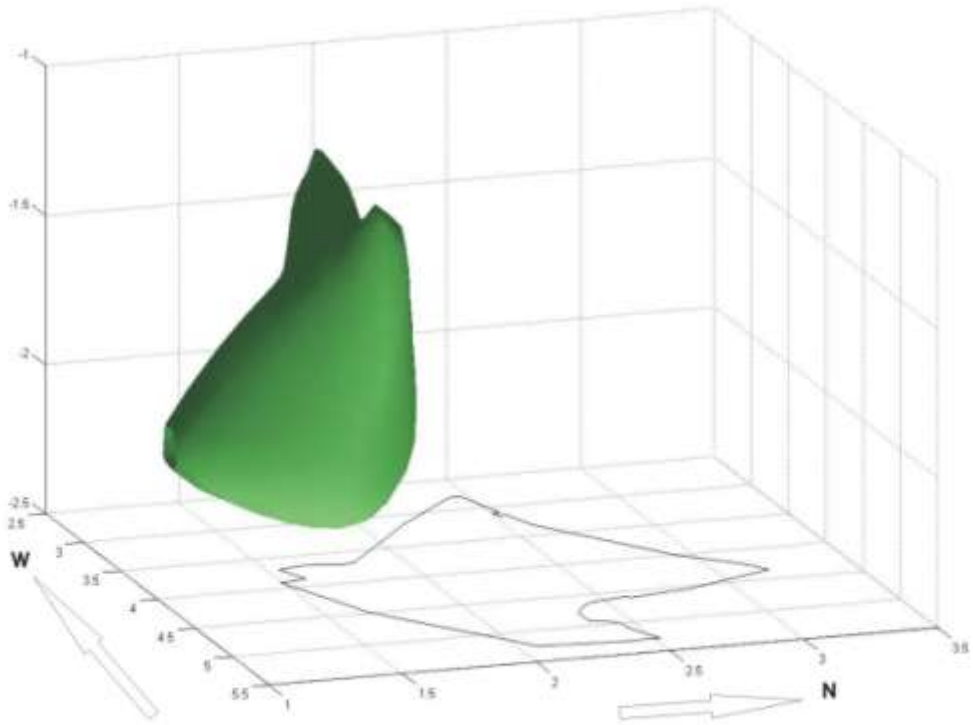

An isosurface plot of a high fracture density body proposed for exploratory drilling. The Example Geothermal Field lease boundary is plotted on the grid bottom for reference.

IESE - SONDI
University of Auckland Uniservices
Private Bag 92019 Auckland Mail Center
Auckland 1142, New Zealand

EXECUTIVE SUMMARY

The Example Geothermal Field borehole seismic network recorded a total of 1864 events in its first 7 months of operation. Most of the recorded events were very small, with more than 90% of them smaller than M~ 0.6. The average seismicity was about 8 events per day with noticeable fluctuation in the number of daily events. The highest seismicity rate was recorded when a swarm of 95 events was detected during a 73 minute time period. The daily seismicity rate exhibits strong periodicity with ~7 day cycles of increasing and decreasing seismicity, and a weaker one at 5 day cycles. These cycles are probably related to the EGF's schedule of operation.

The large number of small events below M~0.6 maybe associated in some way with the EGF's power generation operations. These events appear to add more than a third more seismicity than might be expected from the local Gutenberg-Richter statistics. If so, the fact that the borehole seismic network is able to detect and locate this high level of events and their 7 and 5 day cycles suggests that it is sensitive enough to monitor the inner workings of the EGF's production and injection system.

3-D maps of P and S velocities and the Vp/Vs ratios show a zone of very high P-velocity near the southeastern corner of the EGF lease. More studies are needed to determine the cause of that anomaly. The Vp/Vs ratio there is probably dominated by the P velocity increase as opposed to low Vs, and thus is not a good fluid content indicator.

On the other hand, this general zone appears to contain a relative abundance of aligned fractures. This conclusion is based on an S-wave splitting analysis of the borehole network seismograms. At this SE corner of the lease, the fracture orientation appears consistent with the direction of the EGF's major rift structure. A 3-D fracture density map calculated from the S-wave splitting time shows the zone of high fracture density to lie at depths of 1.2 km to 2.2 km. This zone trends further to the south, extending outside the lease boundary. No other equivalent volume of high fracture density was found in the lease area.

It is our recommendation that all efforts toward any enlargement or enhancement of the EGF should be concentrated on the SE corner of the current lease. We do not find any promising zones in other parts of the lease and cannot recommend drilling elsewhere.

SUMMARY OF NETWORK OPERATION

The Example Geothermal Field (EGF) borehole geophysical network has been completed and is now fully operational (Figure 1). The network started operation with 5 stations: P01, P02, P03, P06 and P08. Two more stations, P04 and P07, were added a couple of months later. The last station, P05, was installed at the end of first year.

Data are collected by visiting each station every 8-12 days and swapping data cards. The job was done by EGF employees. It is important to ensure the continuation of data collection for smooth network operation.

Recently, data analysis from the network has been somewhat problematic, when the network computer was installed at the EGF. Connections to the computer are blocked by the local firewall, and operating the computer from outside the EGF is impossible at the moment. IESE-SONDI was able to get data through an FTP site, but that solution is no longer possible. IESE-SONDI and the EGF operators are working on solving the firewall problem for future data analysis.

Figure 1. Map of the Example Geothermal Field region and the 8 station borehole seismic network. These stations are marked with red squares. These stations include: seismometers, accelerometers, tiltmeters, and passive electric and magnetic field sensors.

EARTHQUAKE STATISTICS

In first 7 months of operation, a total of 1864 events were located by the network (see Figure 2). All events located by the network are listed in the accompanying DVD file "EGF_MEQ_LIST.txt". Location quality greatly improved significantly with the addition of Stations P04 and P07.

Earthquake magnitudes were calibrated using the larger events detected by the EGF's surrounding regional seismic network. The lowest magnitude threshold of reliable detection and location for the borehole network is about magnitude M~ - 0.2. This is a great improvement over the regional network that has a minimum threshold of 2.0.

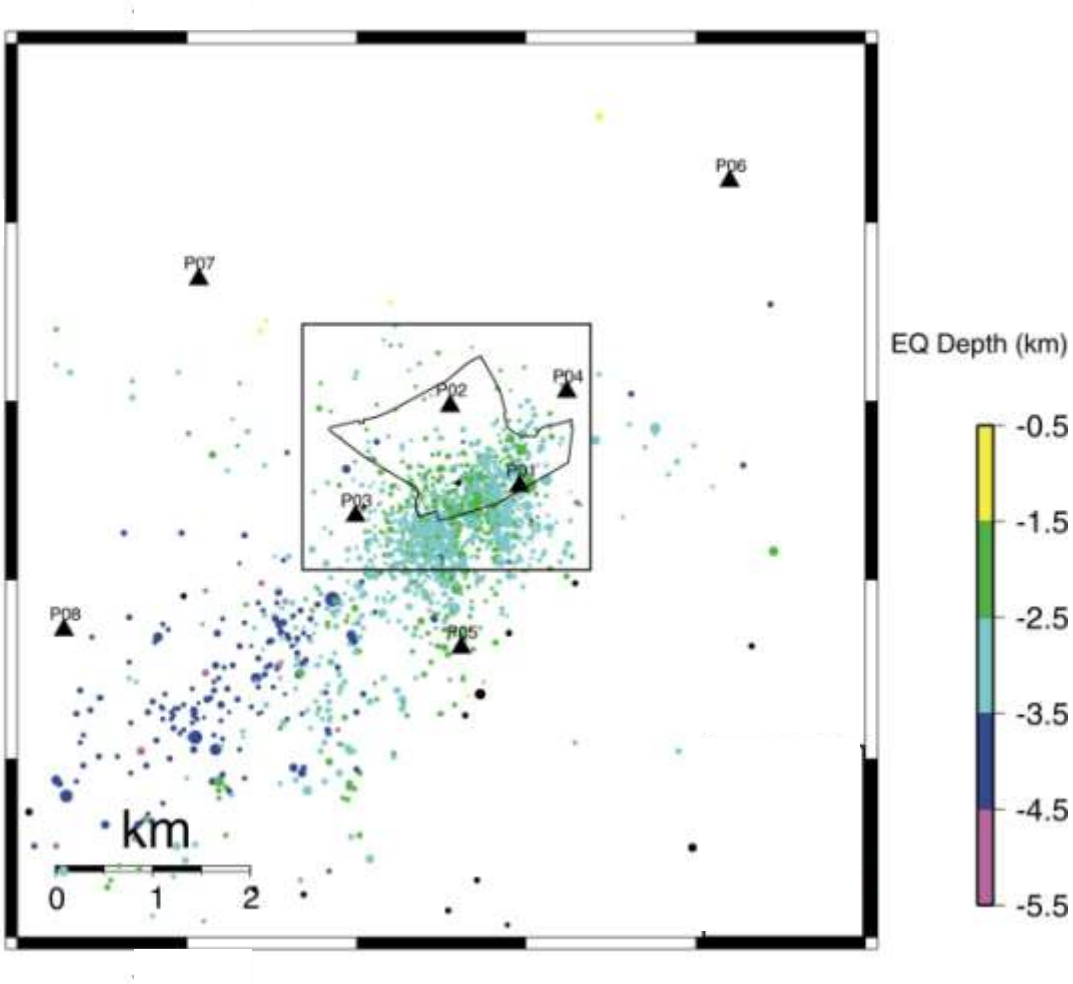

Figure 2: Map of all close events located by the EGF borehole seismic network. Circles mark earthquake location; the color of the circles marks depth and the circle size indicates magnitude (Largest circle = M~2.5). The black rectangle represents the area of detailed 3-D mapping. Also shown is the EGF lease boundary interior of this rectangle.

As is the case with many geothermal fields, the ratio between the number of small and large events is higher than in other seismically active areas. This effect can be seen in the so called Gutenberg-Richter relationship of cumulative number of events versus magnitude. The Gutenberg-Richter relation is given by:

$Log_{10}N = A - B*M$

where M is the magnitude, $Log_{10}N$ is the logarithm of cumulative number of events with magnitude equal or greater than M, and B is the ratio of these values. In most seismically active places, the "B value" is about 1. The result is that for each unit step in magnitude one can expect a 10 fold increase in the number of earthquakes. At the EGF the average B-value is 1.4 (Figure 3). This means that for every unit drop in magnitude (e.g. from 2.0 to 1.0) a roughly ~25 fold increase in seismicity is observe at the EGF site.

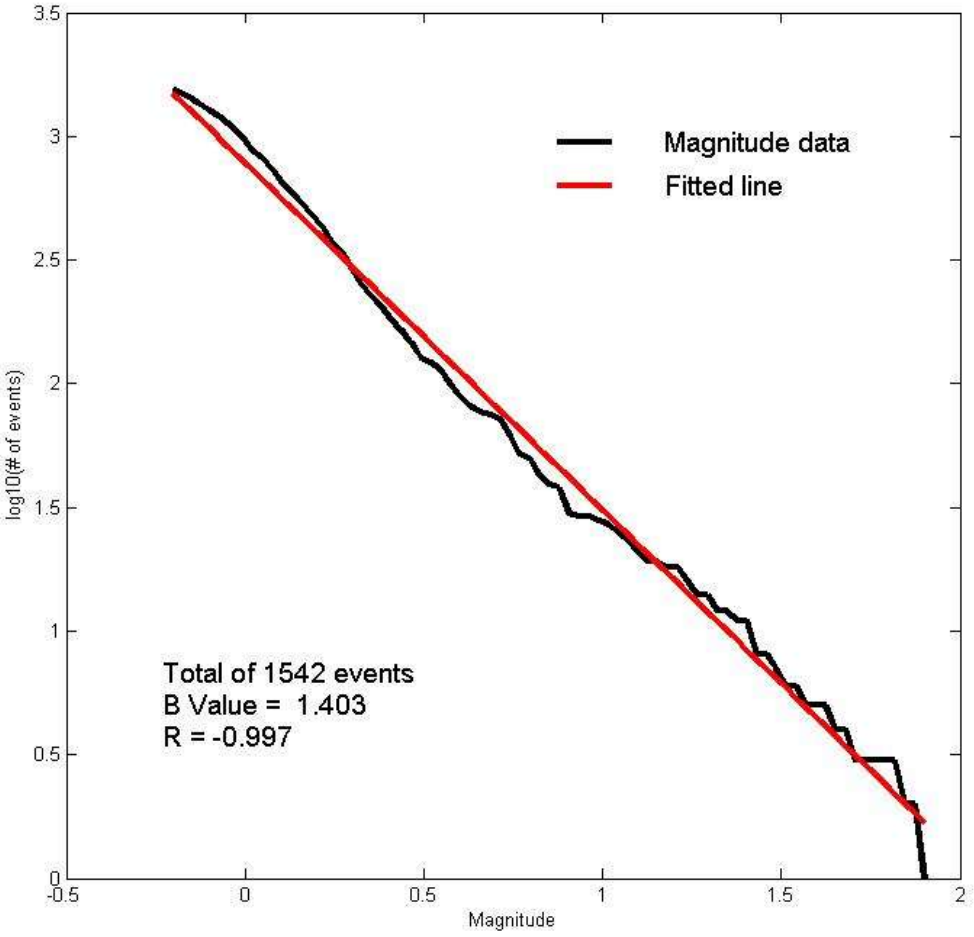

Figure 3. Gutenberg-Richter relation for all events inside a 5 km radius of the EGF network.

The graph of the "Magnitude data" in Figure 3 also shows a further increase in the B value below about magnitude 0.6 or so. Thus the B-value for events smaller than this is even larger than 1.4. This increase in the number of smaller events probably relates to the plant operations at the EGF site. Perhaps the proportion of reinjection events below M ~0.6 at the EGF site is higher than at other geothermal fields. For a B value of ~1.6 the cumulative number of events would increase by more than a third. As discussed below, there are other peculiarities that might also relate to this possibility.

The average seismicity detection rate during the 7 months covered here was about 8 events per day. Figure 4 shows that the seismicity rate was relatively stable most of the time except for a marked increase after Day 200. That increase peaked on Day 212, when a swarm with a minimum number of 95 events were recorded and located in 73 minutes. The total number of events during this period was considerably higher, but many events occurred almost simultaneously and could not be located (see Figure 5 next page).

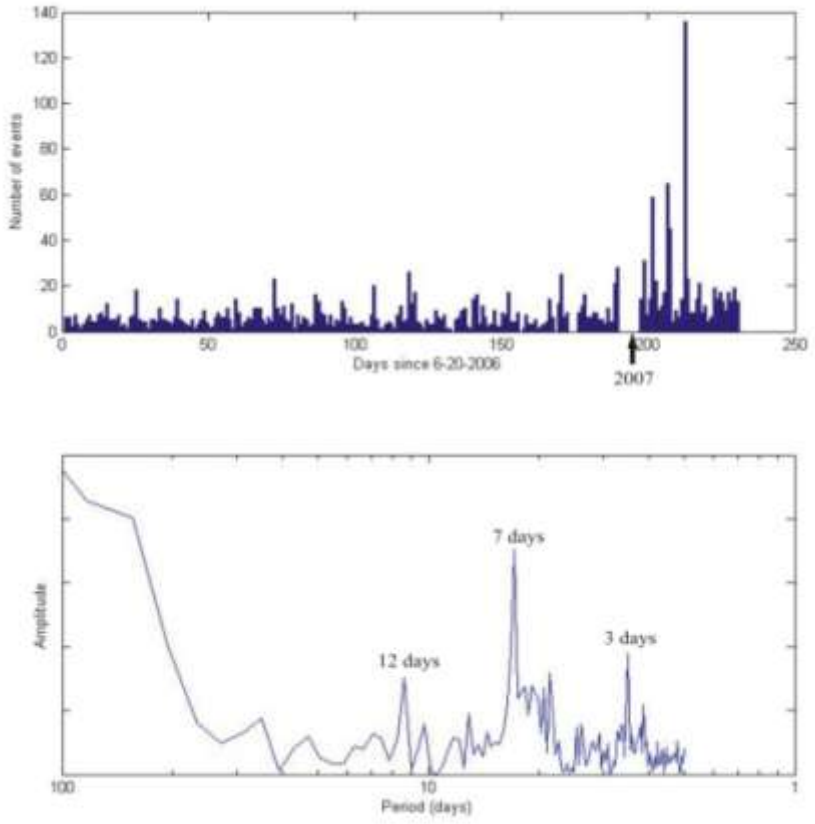

Figure 4. EGF daily seismicity (top); periodicity (bottom). Maximum=Day 212; Period =days/cycles, the values to the right of each labeled decade being P=decade/N cycles where N=the number of logarithmic units to right (e.g. 3 days/cycle = 10 days/3.3 cycles). There are 3 large, sharp peaks at 3, 7, and 12 days, and a smaller broad one at 5. A delayed data-mailing caused the gap around 2007, arriving too late to be included, but not impacting our conclusions.

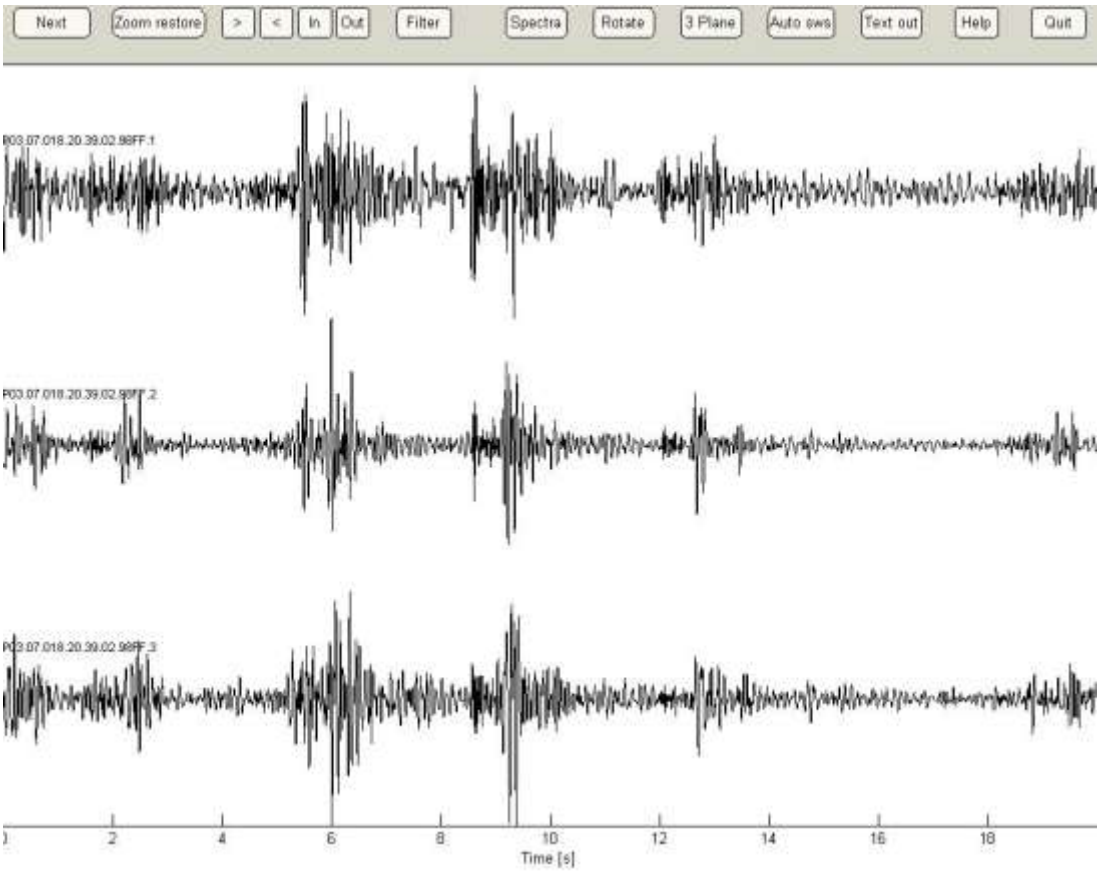

Figure 5. A 20 second section of Station P03 seismograms showing more than a half-dozen events during the earthquake swarm. Top trace: vertical component; Lower traces: horizontal components. At least 3 events were locatable, the rest begin obscured by the overlapping codas.

An important feature of the seismicity shown in Figure 4 is its apparent periodicity in event rate: the number of events per day rises and falls at regular intervals. The periodicity analysis of the daily rate data (Figure 4 bottom) shows 3 strong, peaked periodicities at ~3 days, ~7 days, and ~12 days, and 1 weaker, broader, periodicity centered on 5 days. It is proposed that the large 7 day peak is related in some way to the EGF's weekly operations. Give low resolution of the relatively short run of data included in the analysis, the smaller ~3 and ~12 day peaks may be its 1st sub harmonic and harmonic. The 5 day cycle may have the same origin and related harmonics, but the latter are much less clear. The true nature of these periodicities is yet to be determined.

If the number of small events and 7 and 5 day cycles of seismic activity are related to the EGF's operation, then the borehole network is clearly a sensitive guide to their effects. Further, the 8th station will improve the accuracy of their locations.

3-D SEISMIC VELOCITY MAPPING AT THE EGF

The results of P wave velocity tomography are shown in Figure 6 as a set of horizontal slices at depths of 1.5, 2.0, 2.5, and 3.0 km below the surface. All these plots and subsequent velocity tomography plots show the focused study area around the EGF lease (the 3 x 2.5 square shown in Figure 2) to a depth of 4 km. Slice depths are measured from the average elevation of the borehole stations.

The most striking feature of the P-wave tomography is the high velocity zone near the southern corner of the lease. This high is vertically persistent and is a robust feature required by the P-wave travel time data. This zone also shows the highest concentration of seismicity, which indicates brittle rock at depth. Another high velocity zone appears to exist at the eastern corner of the lease, but here resolution and accuracy are not as high.

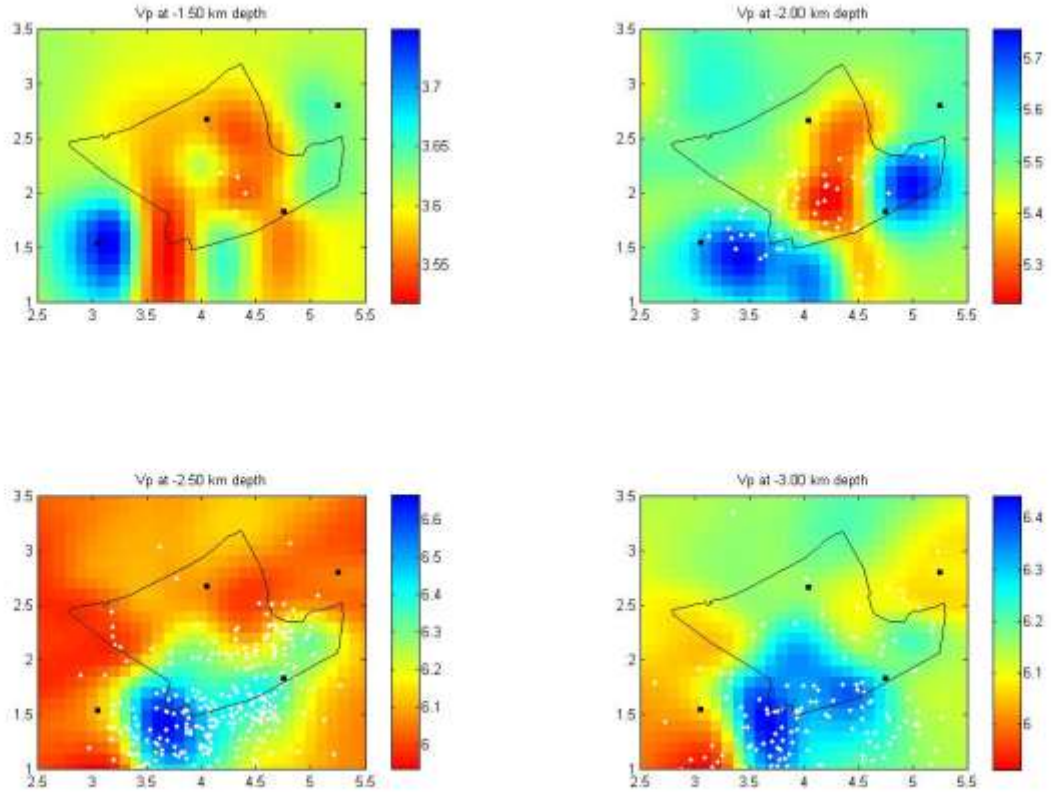

Figure 6. Horizontal slices of the 3-D P wave velocity at the EGF. Red color indicates slow velocity, blue color indicates fast velocity. White dots mark earthquakes inside the layer.

Figure 7 shows the 3-D S wave velocity of the target area as horizontal slices at depths of 1.5, 2.0, 2.5, and 3.0 km. Slow S velocity (red colors) can be a sign of higher fluid content in the rock but may also indicate different rock composition. The southern half of the lease area, at a depth greater than 2 km, exhibits low S velocity but it is not clear if that is due to a higher volume of fluid in that zone.

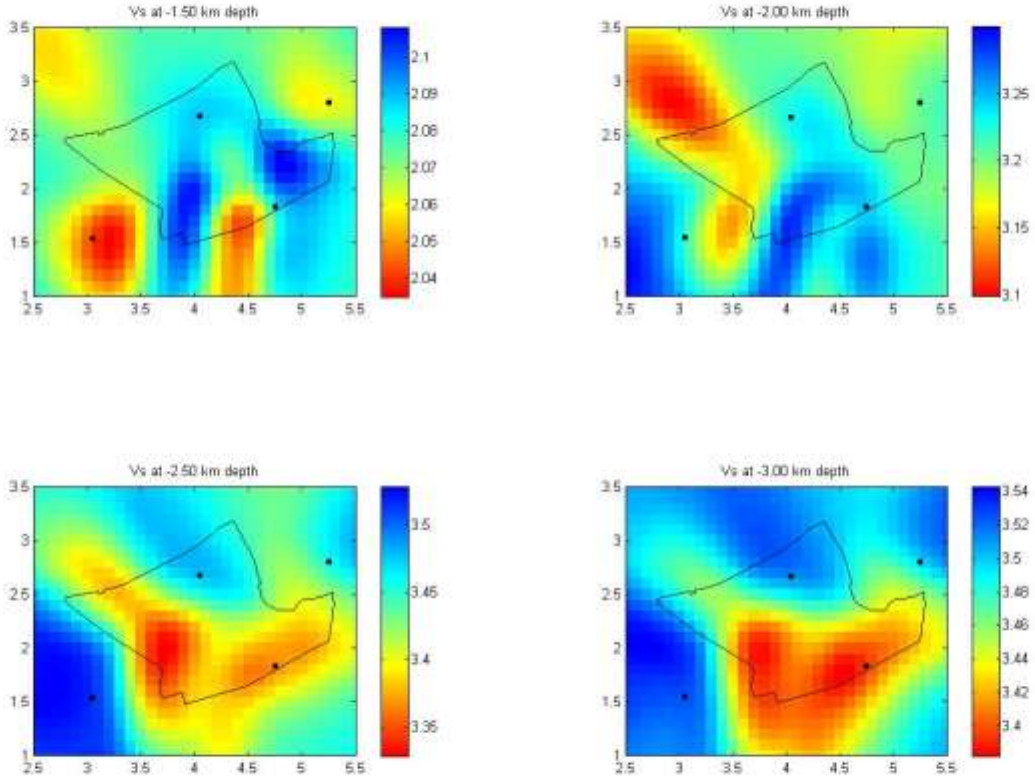

Figure 7. Horizontal slices of the 3-D S velocity at the Example Field geothermal area. Red color indicate slow velocity, blue color indicates fast velocity.

Figure 8 shows the Vp/Vs ratio tomography for the target volume. It is important to notice that this Vp/Vs ratio is not simply the division of the P velocity by the S velocity but a separate, independent inversion based on the observed ratio of the P- and S-travel times. High Vp/Vs ratio (blue colors) may serve as a good indication for drilling targets since fluid filled fractures tend to reduce S velocities more than P velocities, resulting in high Vp/Vs. However, the main contributor to the high Vp/Vs region on the SE boundary of the EGF is the very high Vp also located there (e.g. see Figure 5). Thus the high Vp/Vs ratio in this zone should not be used on its own as a drill targeting tool.

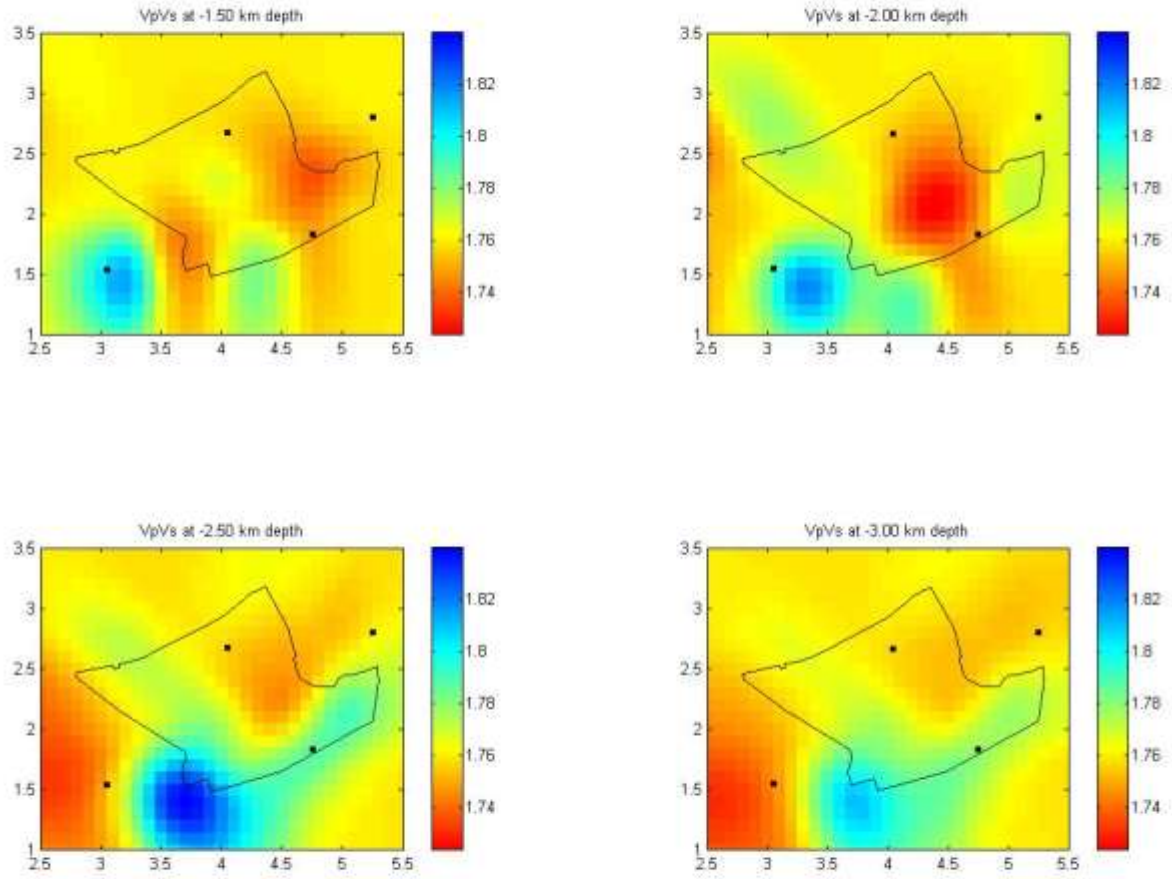

Figure 8. Horizontal slices of the 3-D Vp/Vs ratio showing changes from the average ratio of 1.76. Red color indicates low ratio, blue color indicates high ratio.

SHEAR WAVE SPLITTING AND FRACTURE DENSITY MAP

Shear wave splitting (SWS), where the S-wave arrives as two time-separated waves, was found to be a common feature of the EGF borehole seismic data. These signals are called the "Fast" and "Slow" S-waves for obvious reasons. In the upper few kilometers of the crust, the separation of these waves is thought to be due to fractures. For sub vertical fractures and borehole sensors, analysis of SWS signals in terms of fractures is limited to raypaths that are close to vertical. The EGF borehole seismic network turned out to be well designed to focus on SWS observations, the four stations close to the EGF lease being in the right places for most events in the data set.

Once SWS is shown to exist in a zone, it may possible to determine the relative density of fractures producing the split, along with some of their other physical characteristics. Fracture density inversion is possible only if the fractures in the target zone are aligned in the same direction. Figure 9 shows the alignment of all the Fast S-waves observed at the EGF site, this direction corresponding to the strike of the fractures.

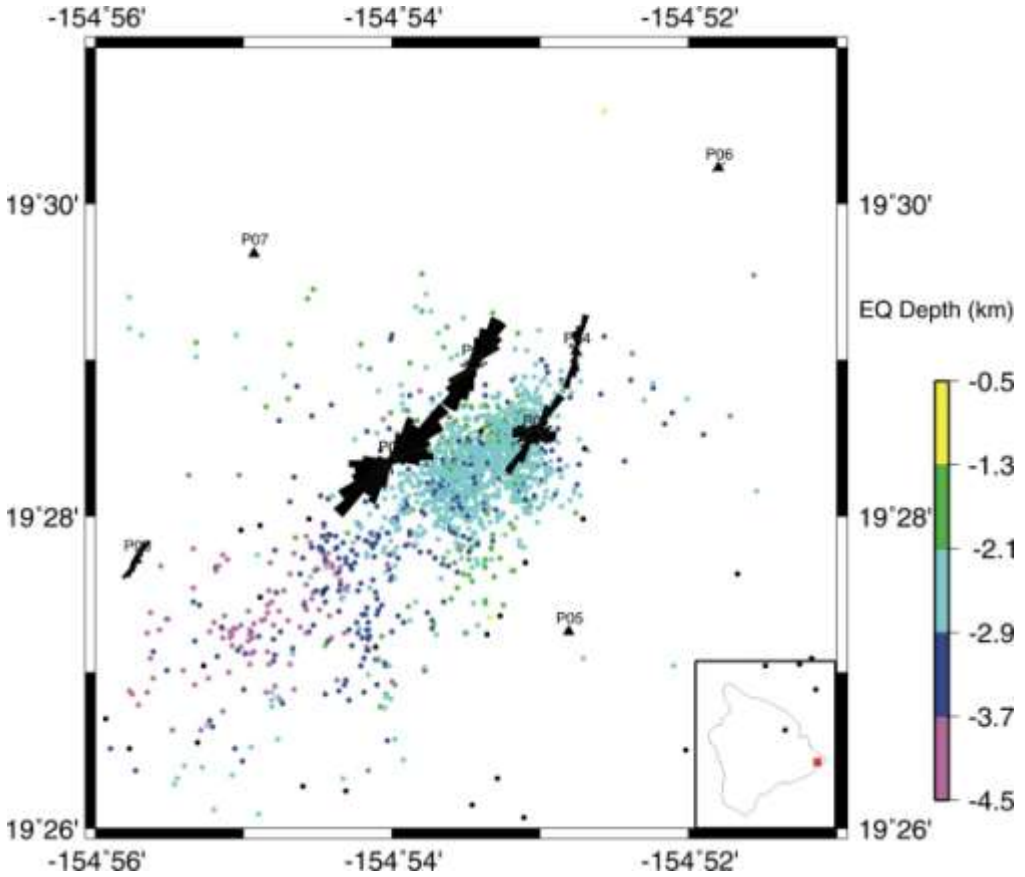

Figure 9. Fast shear wave polarization directions for the EGF stations. The 4 close showed the most SWS. The rose diagrams show the number of SWS for each direction.

Since all the EGF seismic stations are in boreholes and the actual directions of the horizontal components are not known, these orientations had to be determined before the Fast and Slow directions could be established. This was accomplished using P-waves from well located events to find consistent back azimuths. The resulting orientations were found within a $\pm$ 10^{o} window. This orientation error can explain the variations in the Fast direction rose diagrams for some of the stations. For the whole SWS data set, the majority of the Fast observations are aligned to 40^{o} T, in agreement with the direction of the known rift zone that crosses this area. Thus a density inversion was possible.

The relative 3-D fracture density tomography at the EGF is displayed in Figures 10 and 11. Figure 10 show horizontal slices of the 3-D volume at depths of 1.25, 1.5, 1.75, 2.0, 2.25, 2.5 km below the mean station elevation. High fracture density zones are marked with red colors. Only one zone of high fracture density can be seen in Figure 10. This zone starts inside the lease boundary near the south corner of the lease and extends to the south outside the lease boundary.

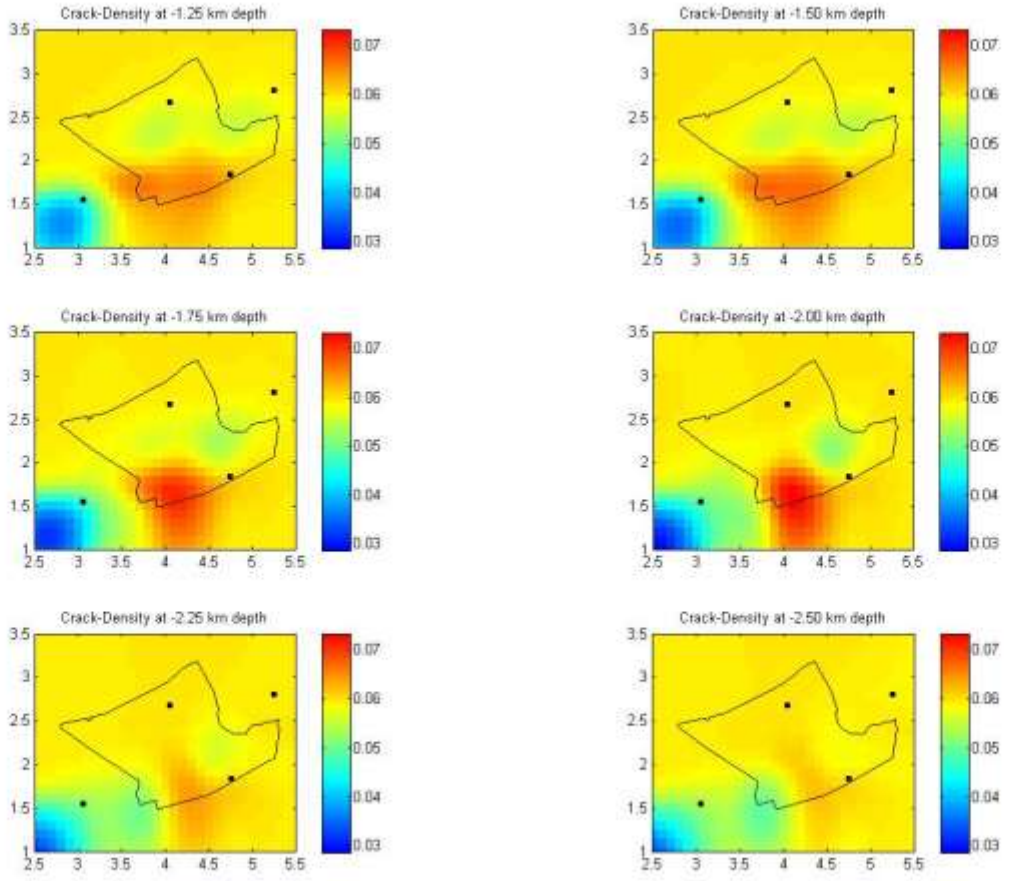

Figure 10. Fracture density map for the Example Field geothermal area. Red color indicates high fracture density; blue color indicates low fracture density.

Figure 11 (on the next page) shows an isosurface plot of the high fracture density region in block diagram. The bounding surface plotted has a relative fracture density of 0.065, inside of which the density exceeds this value - meaning all values of fracture density greater than 0.065 are inside the plotted surface and values below 0.065 are outside of it.

These plots of high fracture density are more qualitative that quantitative. In other words, high and low regions should be looked at in relation to each other and not as threshold numbers that define high or low fracture densities. The value of the surface plotted in Figure 11 is thus in relation to its surroundings, indicating it is likely to be a better bet as a geothermal drilling target. This region seems to be limited between depths of 1.2 km (3900 ft) and 2.25 km (7400 ft), although the shallow depth limit is not well resolved by the available distribution of stations and events. This region extends toward the south and lies outside the lease boundary. No other regions inside the lease boundary appear to have equally high fracture densities.

For other views of the various tomography results, including the fracture density volumes, the DVD accompanying this report contain files of all the inversion results digitized at 100 m node spacing. The results can thus be displayed with any interactive 3-D plotting programs, enabling the viewer to rotate and change view points.

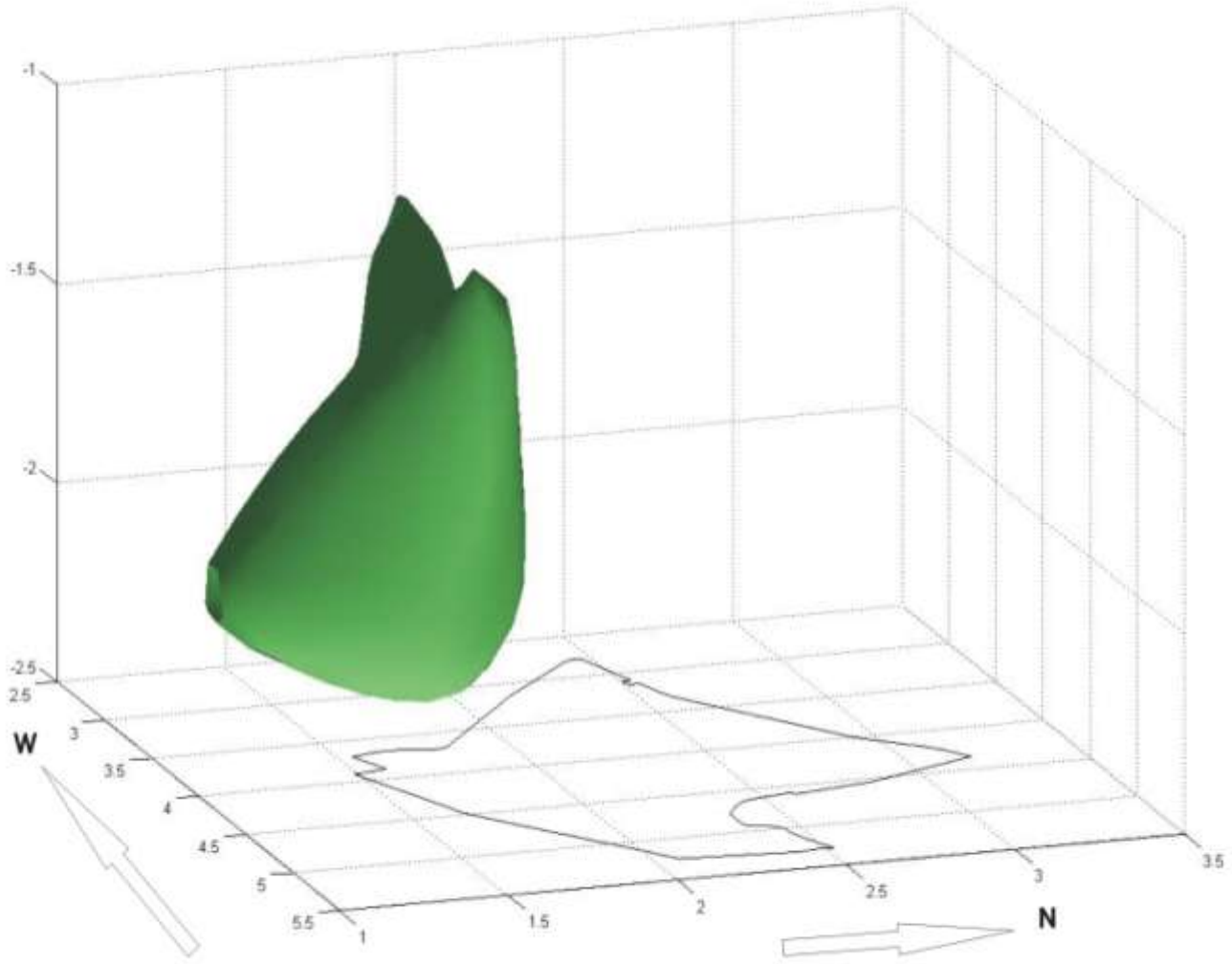

Figure 11. An isosurface plot of the greater than 0.065 fracture density zone from Figure 10, looking from the southeast direction. The EGF's lease boundary is plotted at the bottom to help see the orientation and location of the relatively high fracture density zone.

CONCLUSIONS AND RECOMMENDATIONS

Simple statistical analysis of the earthquake data collected by the EGF borehole seismic network shows that the seismicity rate at this site is about 8 events per day. Of these events less than ~10% are larger than Magnitude 0.6. Further, the Gutenberg Richter B-value of very small events seems to increase below M~0.6. These results explain why most of the EGF earthquake activity completely escapes the notice of the regional surface seismic network, which has a detection and location cutoff of M~2.

Periodicity analysis of the EGF's seismicity rate shows 3 dominant cycles of activity, the strongest taking place on a 7 day cycle. This increase and decrease in seismicity may have something to do with the operation of the EGF's power plant and reinjection systems, since weekly changes are common cycles for cultural events. It also maybe the cause of a weaker 5 day cycle that appears in the data as well.

Assuming that the numerous small events and changes in their rates are due to the EGF's operations, then it appears that the borehole seismic net is sensitive enough to monitor the EGF's inner workings and its reaction to human activities. A joint analysis of its power plant activities and the seismic reaction of the geothermal field to them may resolve this question and as result enhance the management of the field's operations.

Tomographic analysis of the P- and S-velocities and Vp/Vs ratios show that the southeast corner of the geothermal lease area contains several unique subsurface features. Both relatively and absolute P-velocities at this location are quite high. On the other hand, its S-velocities are only moderately slow relative to its surroundings. This causes the Vp/Vs ratio near this zone to be high. Based on the high absolute P-velocities, the rock there is very competent and thus the high Vp/Vs zone is not necessarily indicative of a good drilling target. More studies are needed to find what causes the high P-velocities.

On the other hand, the 3-D fracture density map also shows a relative high density near the SE corner of the lease in the depth range of 1.2 to 2.2 km. This region of high fracture density extends further toward the south and outside the lease boundary.

It is our recommendation that all efforts toward enlargement or enhancement of the EGF should concentrate on this zone. We do not find any other promising zones in the lease area and cannot recommend drilling in other locations.

ATTACHMENTS

Six supporting digital documents are attached to this report in the form of a DVD:

File#	Name	Contents	Size
1.	EGF_MEQ_List.txt	A hypo71 list of event locations	
2.	EGF _3-D_maps.doc	A description of the 3-D maps	
3.	Vp_vol.out	3-D map of P velocity	
4.	Vs_vol.out	3-D map of S velocity	
5.	VpVs_vol.out	3-D map of Vp/Vs ratio	
6.	CD_vol.out	3-D map of fracture density	

REFERENCES TO RELATED STUDIES

2007 Onacha, S., P. Malin, E. Shalev, W. Cummings, K. Arnasson, and B. Palsson. Formulation of a porosity operator for joint interpretation of resistivity and microearthquake data across a fluid-filled fracture zone. Proceedings of the 29th New Zealand Geothermal Workshop, 19-21 Nov 2007, University of Auckland. 6 pp.

2007 Kahn, D., P. Malin, and E. Shalev, The Basel HDR Stimulation: MEQ Scaling as a Function of Event Size. Proceedings of the 29th New Zealand Geothermal Workshop, 19-21 Nov 2007. University of Auckland. 7 pp.

2007 Onacha, S., P. Malin, E. Shalev, S. Simiyu, and W. Cumming. Microearthquake and resistivity imaging of the Longonot geothermal prospect, Kenya. Proceedings of the 29th New Zealand Geothermal Workshop, 19-21 Nov 2007. University of Auckland. 6 pp.

2005 Onacha, S., D. Kahn, P. Malin, and E. Shalev. Resistivity and Microearthquake Imagaing of the Krafla Geothermal Field, NE Iceland. Geothermal Resources Council Annual Meeting, Reno, NV, Sept. 2005. 6 pp.

2000 Simiyu, S.M., and P.E. Malin. A volcanoseismic approach to geothermal exploration and reservoir monitoring: Olkaria, Kenya and Casa Diablo, USA. World Geothermal Congress, pages 001-006, 5 color figures, June 2000. see: http://www.wgc.or.jp/08/cdrom.html

1999 Malin, P.E., and E. Shalev. Shear-wave splitting crack density maps for the Geysers and Mammoth geothermal fields. Invited paper in: Horne, R., Editor Twenty-Fourth Workshop on Geothermal Reservoir Engineering, Stanford University, Stanford, SGP-TR-162, 1999.

1997 Lou, M., E. Shalev, and P.E. Malin. Shear-wave splitting and fracture alignment at the Northwest Geysers, California. Geophysical Research Letters 24: 1895–1898.

1994 Malin, P.E. The seismology of extensional hydrothermal systems. Geothermal Resources Council Transactions 18: 17–22.